In Search of Small Planets Around Small Stars:
Conducting Photometric Transit Surveys of Nearby M-dwarfs

By

Dax Lee Feliz

Dissertation

Submitted to the Faculty of the

Graduate School of Vanderbilt University

in partial fulfillment of the requirements

for the degree of

DOCTOR OF PHILOSOPHY

in

Astrophysics

May 13th, 2022

Nashville, Tennessee

Approved:

Keivan G. Stassun, Ph.D.

Karen A. Collins, Ph.D.

Joshua Pepper, Ph.D.

David A. Weintraub, Ph.D.

Andreas Berlind, Ph.D.

DEDICATION

I would like to dedicate this dissertation to my family, many friends and mentors. A special feeling of gratitude goes to my loving mom, Robin, and my sisters, Angie and Cheyenne, who have always encouraged my dream of being an astronomer since I was a child, with unwavering support. They have always been with me through all of my failures and successes and without them, I don't know if I ever would have gotten this far. I'd like to promise my twin nieces, Charlotte and Eden, that I will call and visit more often to make up for lost time. I dedicate this dissertation to my Godfathers, Roldan (may he rest in peace) and Pito, and my Godmothers, Samantha and Nilsa, for being there and helping me learn right from wrong. I would also like to dedicate this dissertation to my friends Alberto, Carlos, Charles, Glenn (may he rest in peace), Misra, Richard, Ryan and Sandra for their constant support, shared laughter and for making the world feel a lot smaller.

Last and not least, I would also like to dedicate this dissertation to my home in Harlem, New York City. There are far too many people to thank but this community has always supported my dreams and ambitions throughout the years and it is on their shoulders that I hope to reach for the stars. It is very possible that I may be the first astronomer to come out of Harlem but I promise that I will not be the last.

ACKNOWLEDGEMENTS

and people I've gotten to meet have endlessly blown my mind as I never thought I'd ever occupy and share these spaces. I owe all of my thanks to him for being an incredible advisor and mentor. I also thank Dr. Karen Collins for being a magnificent research mentor and spending countless hours teaching and guiding me on how to be an astronomer. I would also like to thank Dr. Joshua Pepper for inviting me into the KELT family and providing so much insight and guidance. I would like to thank rest of the members of my dissertation committee, Drs. David Weintraub and Andreas Berlind for their invaluable time, advice, and expertise and for validating my experiences and progress during my PhD.

TABLE OF CONTENTS

LIST OF TABLES

LIST OF FIGURES

A4   Example of NEMESIS TLS Validation Report for the transiting planet TOI 270 c (TIC 259377017).

Top Left: *Odd/Even Mismatch test*, we take the odd and even numbered transits and compare how much each transit depth compare while visually verifying that transit duration and shape are consistent. We also display the best-fit TLS transit model in red. **Middle Left:** *FFI image cutout*, an 11×11 pixel cutout of the FFI. We display the target star as a blue X with the center of the centroid of as a yellow X and the selected aperture mask in red with the background shown in purple. Nearby stars are labeled with their GAIA magnitude with cyan colored circles and red text. To visually check whether the centroids are on target, we also place small purple dots marking the centroid positions at each cadence. **Lower Left:** *Centroid Motion*, to help keep track of centroid positions we also plot the motion in the image column (black points) and image row (red points) pixel positions in time and then phase fold the timestamps relative to the TLS detected transit time and period. **Upper Right:** *Light Curve*, we display the full light curve in black points with the best-fit TLS model in red. The transits times are marked by cyan arrows and the momentum dumps are marked with vertical blue lines. We also display the CDPP noise metrics for the light curve before processing for the SAP light curve and afterwards for the detrended light curve. **Middle Right:** *TLS Power Specrum*, we display the TLS power spectra in terms of Signal Detection Efficiency (SDE) as a function of orbital period in days. We mark the momentum dump rate with a vertical grey dashed line, the TLS period corresponding to the strongest SDE peak is marked with a solid red line and 0.5x and 2x harmonics of the TLS period are marked with dashed red lines. **Middle:** *Phase Folded Light Curves,* we fold our light curve centered on the transit time, for the full orbital phase and at 0.5x, 1x and 2x the TLS period. **Lower Middle Right:** *DSS Cutout*, to help visualize our target star we also query the Digitized Sky Survey (DSS) catalog which has a smaller pixel scale than TESS for quick reference. **Lower Right Text:** We display various stellar parameters queried from the TIC and best-fit planet parameters output by TLS. **Top Center Text:** *EDI Vetter Unplugged*, using a modified version of the EDI Vetter tool[19] which uses outputs from TLS, we conduct several automated planet candidate vetting tests with false positive results marked in red colored text which suggest the candidate requires a closer inspection . . . .

Chapter 1

Introduction

The very first extra-solar planets (called exoplanets hereafter) were discovered at an initially slow rate as the field was pioneered in the 1990s, with the first confirmed exoplanet discovered by Wolszczan & Frail 1992, the first exoplanet orbiting a main sequence star discovered by Mayor & Queloz 1995, and the first exoplanet to be discovered with the transit method discovered by Konacki et al. 2003. As of March 2022[1], there are over 4,935 confirmed exoplanets with over 2,700 exoplanets coming from the Kepler mission (Borucki et al., 2010), over 470 from the Kepler K2 mission and almost 200 confirmed exoplanets from the Transiting Exoplanet Survey Satellite mission (TESS, Ricker et al. 2014). In the early days of exoplanetary science, the primary method of exoplanet detection was Doppler spectroscopy (also known as the radial velocity method) which indirectly measures the gravitational pull of unseen planets on a star through periodic Doppler shifts in the observed stellar spectra. Since the Kepler mission launched in 2009, the dominant method of exoplanet detection is now the transit method, which aims to indirectly detect the presence of a planet by searching for periodic eclipses present in the photometric time-series observations of a star. Of the 4,935 confirmed exoplanet discoveries, 3,811 of them were detected with the transit method versus the 915 that were detected with the radial velocity method. At the core of this dissertation, the transit method is the most relevant of all exoplanet detection techniques and I summarize the method in the following section.

---

[1] https://exoplanetarchive.ipac.caltech.edu/

1.1 The Transit Method

If an object passes between a star and the Earth, it will block a portion of the stars light, and the observed brightness will temporarily decrease. If the duration of this event is consistent and occurs periodically, it is an indication that an object, like a planet, could be eclipsing the star in our line of sight (transiting) once per its orbital period (P). By measuring the time in between transit events, the orbital period can be obtained. Additionally, the fraction of light of the star blocked by the planet during transit can be approximated as the fraction of the stellar disk that is eclipsed by the planetary disk and is directly related to the size ratio between the star and the planet:

$$\Delta F \equiv \frac{F_{no\ transit} - F_{transit}}{F_{no\ transit}} = \left(\frac{\pi\ R_P^2}{\pi\ R_S^2} \right) = \left(\frac{R_P}{R_S} \right)^2 \tag{1.1}$$

where R_P and R_S are the radii of the planet and the star, respectively. With the orbital period measured, the photometric time series of the star can be folded over the period to produce a stronger signal. With each transit event measured, folded over the orbital period, it is possible to obtain a few other observable parameters that describe the orbit of this transiting planet, using Figure 1.1 as a reference.
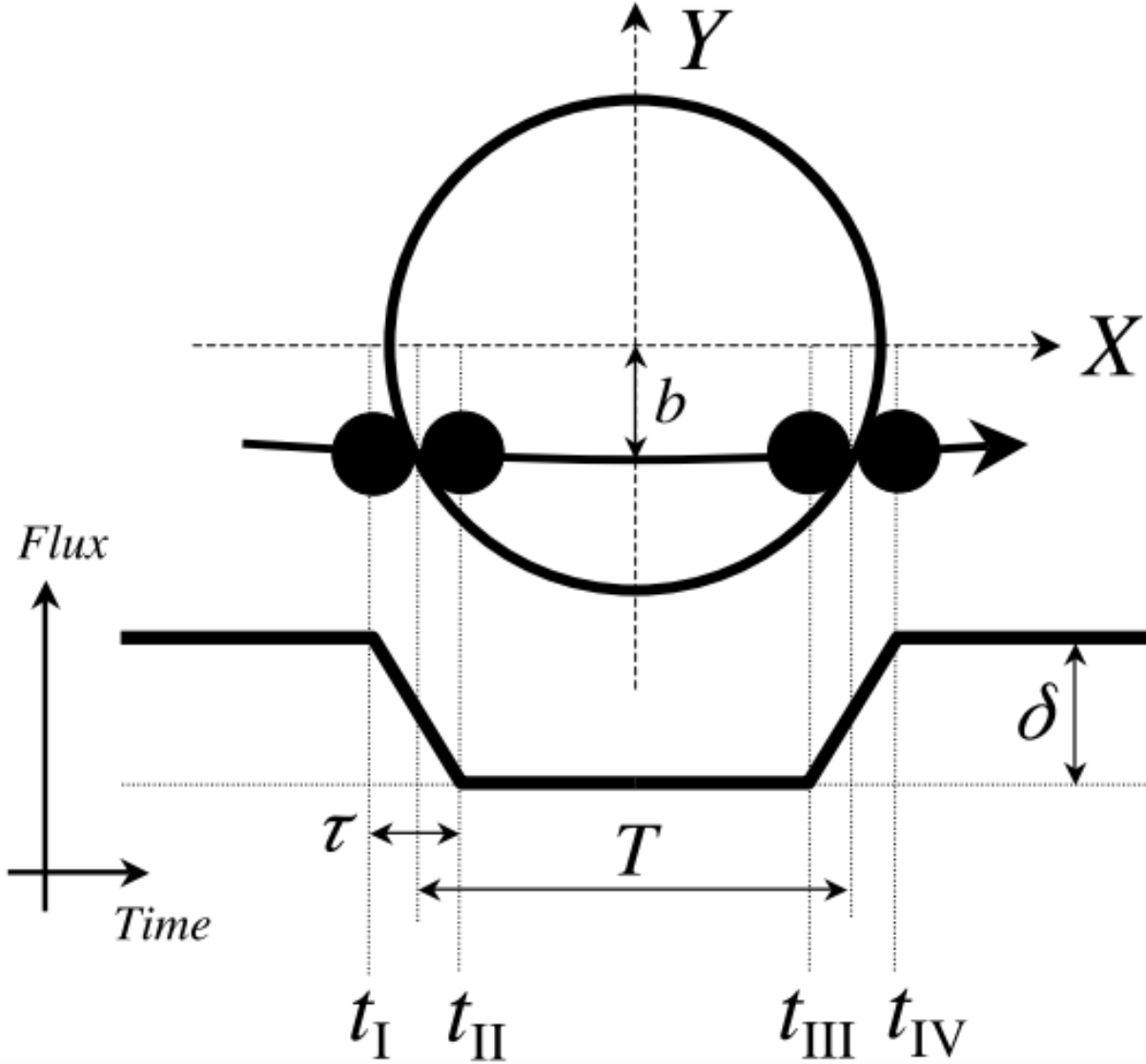
Figure 1.1: Figure 2 from Winn 2011: Illustration of the geometry of a planetary transit in a light curve. A coordinate system is chosen so that it is centered on the star, with the sky in the XY plane and the +Z axis pointing at the observer. The four contact points (t_I, t_{II}, t_{II}, t_{IV}) represent various moments during a transit event where the planet eclipses the host star. T represents the transit duration and τ represents the ingress/egress duration. b is the impact parameter and δ is the transit depth.)

To measure the total transit duration for a circular orbit, the difference in time between contact points t_{IV} and t_I can be defined as shown in Equation 14 from Winn 2011:

$$T = t_{IV} - t_I = \frac{P}{\pi} \sin^{-1} \left[\frac{R_S \sqrt{(1 + \frac{R_P}{R_S})^2 - b^2}}{a \, \sin i} \right] \tag{1.2}$$

3

where a is the semi-major axis, i is the orbital inclination (relative to an observer), and b is the impact parameter (the projected distance between the planet and star centers during mid-transit in units of stellar radius). The ratio between the semi-major axis (a) and the stellar radius (R_S), and the impact parameter (b), can be directly defined from the contact points from Figure 1.1 and Equation 1.1 (as shown in Equations 7 and 8 from Seager & Mallén-Ornelas 2003):

$$b \equiv \frac{a}{R_S} \cos i = \left[\frac{(1 - \sqrt{\Delta F})^2 - \frac{\sin^2 \tau_{III-II}}{\sin^2 \tau_{IV-I}}((1 + \sqrt{\Delta F})^2)}{1 - \frac{\sin^2 \tau_{III-II}}{\sin^2 \tau_{IV-I}}} \right]^{1/2} \qquad (1.3)$$

$$\frac{a}{R_S} = \left[\frac{(1 + \sqrt{\Delta F})^2 - b^2(1 - \sin^2 \tau_{IV-I})}{\sin^2 \tau_{IV-I}} \right]^{1/2} \qquad (1.4)$$

where τ_{III-II} and τ_{IV-I} are defined as:

$$\tau_{III-II} = \frac{(t_{III} - t_{II})\pi}{P} \quad ; \quad \tau_{IV-I} = \frac{(t_{IV} - t_I)\pi}{P} \qquad (1.5)$$

And the stellar density (ρ_S) can be defined from Kepler's Third Law and Equation 1.4 as Equation 9 from Seager & Mallén-Ornelas 2003):

$$\frac{\rho_S}{\rho_\odot} \equiv \frac{M_S/M_\odot}{(R_S/R_\odot)^3} = \left[\frac{4\pi^2}{P^2 G} \right] \left[\frac{(1 + \sqrt{\Delta F})^2 - b^2(1 - \sin^2 \tau_{IV-I})}{\sin^2 \tau_{IV-I}} \right]^{3/2} \qquad (1.6)$$

To summarize, with the transit method, the frequency, shape and duration of the transit events can provide estimates of the orbital period (P), impact parameter (b), orbital inclination (i), the stellar density (ρ_S) and most importantly, the planet radius (R_P) relative to the host star radius (R_S). While the transit method is the most effective method of exoplanet detection to date, it is not without its downsides.

While the radial velocity method can detect exoplanets orbiting their host stars of all orbital inclinations (with the exception of "face on" orbits with i$\sim$0°), the transit method is restricted to planetary orbits where i$\sim$90°) ("edge on") since the planet must pass directly between the star and

the observer. For a circular orbit (with zero eccentricity), the probability that an exoplanet's orbital plane is aligned with an observer can be defined as Equation 9 from Winn 2011:

$$P_{transit} \approx \frac{R_S + R_P}{a} \tag{1.7}$$

For example, for a Sun-like star ($R_S = R_\odot$), the probability of observing a transiting Earth-sized planet ($R_P = R_\oplus$) at 0.1 AU from it's host star is $\sim$4.69% whereas that same planet at the same distance from an M-dwarf-like star (say $R_S = 0.25 R_\odot$) is $\sim$1.21%. In order to confirm the existence of a transiting exoplanet and its orbital period, multiple observations of the transit events must be obtained in order to refine the ephemeris and establish enough phase coverage to rule out other possible orbital periods. For these reasons, transit surveys must observe large patches of sky, continuously, for long stretches of time, in order to improve the chance of observing transiting exoplanets. Lastly, blind transit surveys are subject to a high detection rate of various phenomena that mimic transit-like features in photometry, known as False Positives. A discussion of various False Positive scenarios and how to vet for them is described in the following sections.

1.2 Vetting for False Positives Scenarios and Confirmation of Transiting Planets

One of the main limitations of blind exoplanet transit surveys is that the transit method is vulnerable to detections of false positives. These must be taken into consideration before one validates a planet candidate as a confirmed exoplanet.

Eclipsing Binaries

Not every periodic dimming in brightness can be attributed to transiting planets as the cause, sometimes it is another star that eclipses the target star. Star systems like these are commonly

referred to as "Eclipsing Binaries". Typically, when companion stars transit directly across the face of a target star, they will have large transit depths indicative of a large transiting body. However, when companion stars have high impact parameters and graze across the edge of the star's face, these transits can appear V-shaped rather than the typical U-shape that planetary transits exhibit. Another way to identify Eclipsing Binaries is to look for a secondary eclipse which occurs when the companion star passes behind the target star in the observer's line of sight, having its own light blocked. If the two stars have different brightnesses, the transit depths of the primary and secondary transits will be different; this makes the non-planetary nature of the companion easier to identify. An illustration of a typical Eclipsing Binary signal in photometry is displayed in Figure 1.2[2].
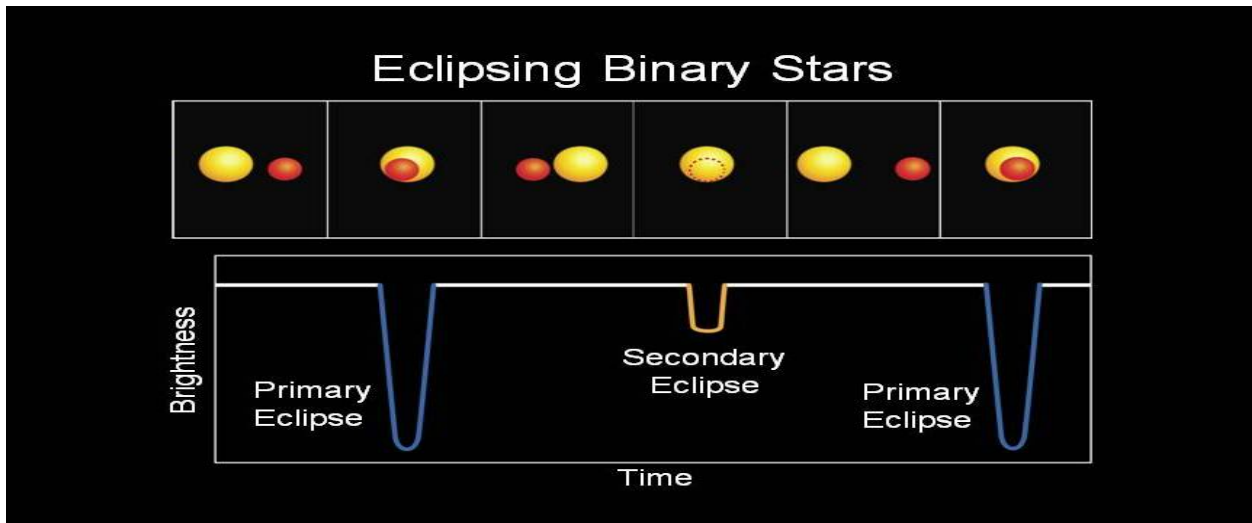
Figure 1.2: When the smaller star partially blocks the larger star, a primary eclipse occurs, and a secondary eclipse occurs when the smaller star is occulted, or completely blocked, by the larger star. Image Credit: NASA[2]

Photometric Contamination of Nearby Stars

A transit-like event can also be caused from nearby or background stars that are located in the photometric apertures used for extracting photometry from astronomical images. When multiple stars are located in the same photometric aperture (either in the foreground or background), the light from both stars are blended together in the photometry and any periodic transit-like features

[2] https://en.wikipedia.org/wiki/File:Light_curve_of_binary_star_Kepler-16.jpg

present in the resulting light curve can be difficult to assess which star the signal is coming from. For example, when another Eclipsing Binary or Star-Planet system is included in the photometric aperture of a target star in the foreground or background, it can be complicated to detangle the photometry without conducting further observations or using different photometric apertures. This kind of photometric contamination can occur because photometers measure all light in a specific aperture, and are not able to resolve individual stars.

A couple of tests and practices that are useful for identifying contamination from nearby sources are a centroid analysis, ephemeris matching or deblending the photometry. By tracking the location of the target star (centroid) throughout a light curve, especially during transit events, any offsets of the centroid present could indicate a False Positive as another nearby photometric source is likely pulling the photometric aperture away from the target star. Another method is to compare the ephemeris (orbital period and mid-transit time) to other known signals, especially of those that are nearby to the target star. If two signals match, this may indicate that at least one of them is a False Positive. For telescopes that use CCD photometry and have large pixel scales, it is not uncommon for multiple stars to be located on the same pixel. To account for this blended light, other catalogs with improved spatial resolution (e.g. GAIA, Gaia Collaboration et al. 2016) can be queried to estimate the total flux in the photometric aperture and the expected flux from the target star. These values can be used to subtract off extra light from the light curve that is not from the target star.

Photometric Noise and Instrumental Systematics

Another potential source of False Positives could be attributed to stellar variability (star spots, pulsations, etc) or instrumental systematics. A number of tests against these types of false positives can include checking the consistency of each transit event in terms of parameters like depth or duration (on the basis that planetary transits should appear the same throughout a light curve), the shape of a transit (planetary transits have a characteristic U-shape), or the uniqueness of the transit events, meaning that there should be no other transit-like events of similar depth or duration.

Confirmation through Follow Up Observations and Validation

The above methods for identifying False Positives in transit photometry are not always success-ful. There could be scenarios where a stellar companion may be too faint to exhibit a secondary eclipse or a giant planet with a high impact parameter may exhibit a deep V-shaped transit which could confused for a grazing Eclipsing Binary. Another scenario is that an Eclipsing Binary or Star-Planet system may be so spatially close to a target star that a centroid analysis does not result in an significant centroid offset. Obtaining follow-up observations of a planet candidate's host star is thus important for confirming planets, identifying False Positive scenarios, and better refining the properties of exoplanetary system.

Spectroscopy and High Resolution Imaging

Spectroscopy and high resolution imaging are important tools for the follow up of exoplan-ets detected with the transit method (Morton & Johnson, 2011). Spectroscopy is able to detect close in binaries through radial velocity variations, and blended scenarios by cross correlating the spectra with a library of synthetic spectral templates to estimate the stellar atmospheric proper-ties, including the effective temperature, rotational velocity, and the surface gravity. Spectroscopic observations also provide more accurate stellar properties than those based only on photometry (Mathur et al., 2017), which in turn provides more accurate exoplanet properties. Meanwhile, high resolution imaging is able to detect companions in wide orbits and those not physically associated with the target. High resolution imaging follow up is typically performed with adaptive optics, which allows image qualities comparable to those taken from space while being more accessible in ground-based facilities. Observations from the ground are often limited by atmospheric tur-bulence, but adaptive optics is able to compensate for this by employing deformable mirrors that correct for the effect. These images produce contrast curves, which place limits on the relative brightness of nearby stars as a function of separation from the target star. The combination of the transit method with vetting for false positive scenarios, doing follow up spectroscopic reconnais-

sance and obtaining high resolution images can lead to the confirmation and overall validation of exoplanet detections.

1.3 Why M-dwarfs are Favorable Target Stars for Transit Searching

As shown in Figure 1.3, a planet transiting a solar-type star will create only a slight dimming, while the same planet transiting a M-type star will have a more noticeable effect[3]. For example, the planet Kepler-186 f has a planet radius of 1.11 $R_\oplus$ and host star radius of 0.472 $R_\odot$ (Quintana et al., 2014) ; using Equation 1.1 gives a transit depth of 465 parts-per-million (ppm) whereas the same planet transiting a Sun-like star (1 $R_\odot$) has a transit depth of 103.6 ppm. M-type stars are also much cooler in temperature than Solar-type stars, so their habitable zones (where liquid water on a planet's surface can exist) are much smaller (Shields et al., 2016) and exoplanets transiting in our line of sight will eclipse their host stars more frequently, as seen from telescopes like TESS.

---

[3] https://www.nasa.gov/sites/default/files/files/Kepler186_FINAL-Apr2014.pdf
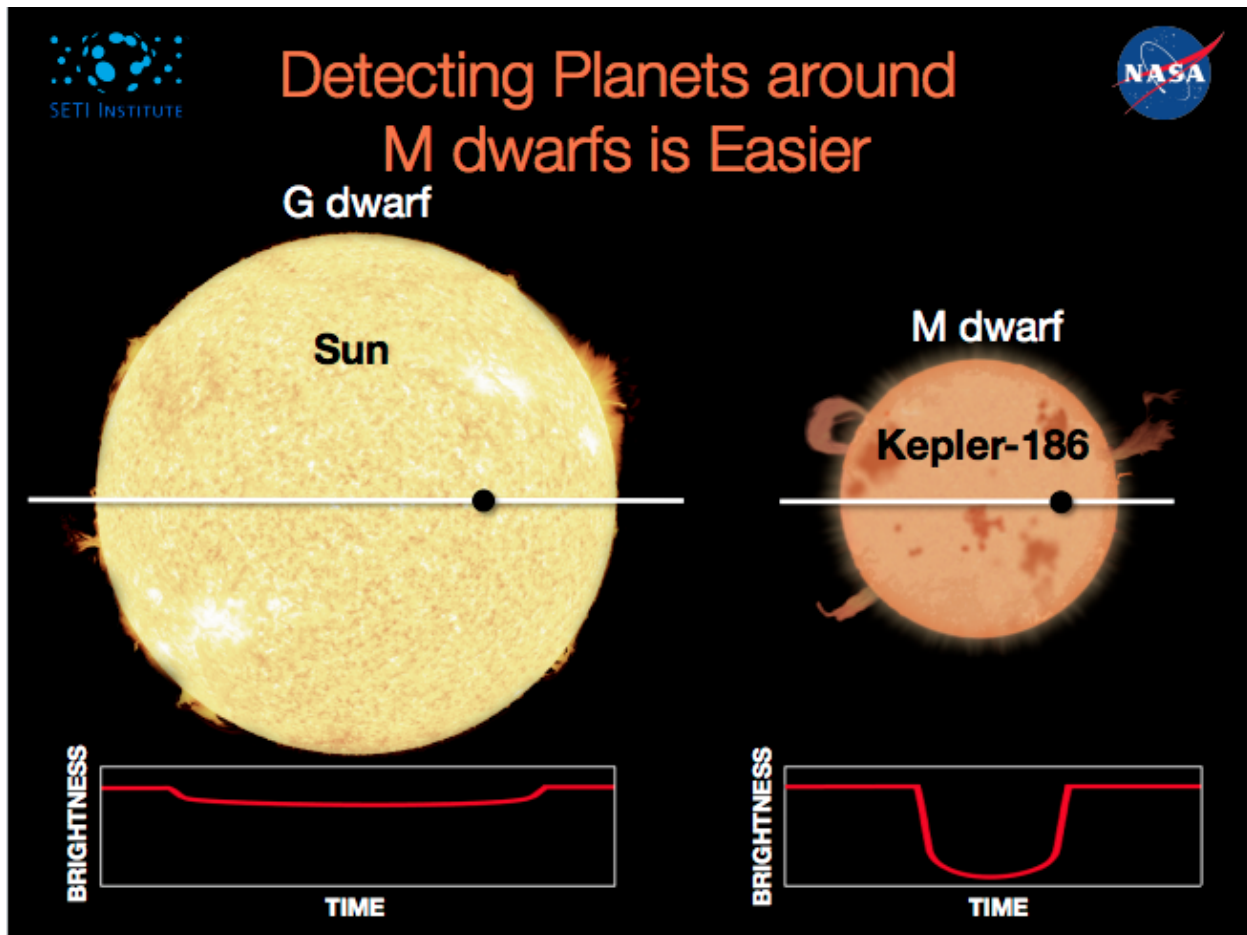
Figure 1.3: A comparison of planetary transit events between Sun-like G stars and M-type stars with identical planets. Image Credit: NASA[3]

M-dwarfs have the lowest mass, size, luminosity and temperature of main sequence stars which comprise 70% of the total number of stars in the Milky Way galaxy (Bochanski et al., 2010). Planetary systems that exist around M-dwarfs could represent the most abundant planetary systems in the galaxy. The hunt for exoplanets, specifically around M-dwarf host stars, is over two decades old, with the first M-dwarf hosted planetary companion discovered by Marcy et al. 1998. The search for exoplanets around M-dwarfs has expanded steadily over recent years because it allows the first detections of low-mass planets in their habitable zones. Because of their low masses and small radii, compared to Sun-like stars, relatively large radial velocity amplitudes and transit depths can occur. Additionally, the transit probability of planets in the habitable zone of M-dwarfs

is correspondingly higher as well.

Stellar magnetic activity can cause confusion in the interpretation of M-dwarf radial velocities. Activity in the form of both starspots and convective inhomogeneities can mimic exoplanetary signatures at the rotational period of the star or its harmonics. When star spots rotate onto the limb of the star, they can change the spectral line profiles (Saar & Donahue, 1997). Additionally, local magnetic fields associated with starspots can cause convective flows that would produce a net blue shift in the spectra (Gray 2009 ; Meunier et al. 2010). While stellar activity presents challenges for radial velocity exoplanet detection for all stars across the main sequence, only for M-dwarfs does the characteristic rotation period coincide with the habitable zone. M-dwarfs of a given mass (above the convective limit) exhibit a spin-down effect in their rotation periods (McQuillan et al., 2013, 2014). However, below the convective limit there appear two divergent populations of faster and slower rotators (Newton et al., 2016b). This gap is likely attributable to a period of short but rapid spin-down of mid-to-late M-dwarfs. While they maintain rapid rotation for several gigayears, they reach periods of 100 days or more by a typical age of 5 Gyr (Newton et al., 2016b). For early to late type M-dwarf systems, the habitable zone corresponds to planetary orbital periods in the range of $\sim$10–100 days (Newton et al., 2016a).

M-dwarf planet detection with the transit method, in contrast, is less affected by stellar variability. Stellar flares in light curves can potentially complicate the search for transits, and have even been observed during transit events themselves (Plavchan et al., 2020). However, studies of M-dwarf photometric variability on the timescales of transits conclude that, depending on the photometric filter used, stellar activity should not meaningfully affect the detection of exoplanets (Tofflemire et al., 2012; Goulding et al., 2012). Although M-dwarfs have a unique set of challenges in analyzing their photometry due to their stellar activity and overall intrinsic faintness, M-dwarfs remain favorable target stars when utilizing the transit method as these stars offer a plethora of

observational opportunities for exoplanet transit detections.

Due to the target star selection strategy of the Kepler & K2 missions, the majority of transiting exoplanets have been discovered around Sun-like host stars, as illustrated by the abundance of exoplanet hosts with Sun-like radii in Figure 1.4. To differentiate M-dwarfs from other star types in Figure 1.4, a simple criteria is used: $2300\,K < \mathrm{T_{eff}} < 4000\,K$, $\mathrm{R_{Star}} < 0.5\,R_\odot$, $\mathrm{M_{Star}} < 0.5\,M_\odot$, and $\mathrm{logg} > 3$. The Kepler space telescope was designed to have spectral bandpass ranging from 400–850 nm, as it was optimized for observing stars like the Sun whose spectra peak in optical wavelengths. The TESS space telescope was designed to have a spectral bandpass ranging from 600-1,000 nm[4] and is optimized for observing cool, red stars like M-dwarfs, whose spectra peak in infrared wavelengths. Both bandpasses are illustrated in Figure 1.5. Since the start of the original NASA Kepler mission in 2010, there have been light curves produced for approximately 200,000 stars (Mathur et al., 2017). Since Kepler was designed to detect Earth-sized planets in the habitable zones of F, G and K stars, only a small fraction ($\sim$2.5%) of stars observed by Kepler are of M-dwarfs (Dressing & Charbonneau, 2015). Using the target star selection criteria for filtering M-dwarfs in the TESS Input Catalog (Stassun et al., 2018), as outlined in Feliz et al. 2021, approximately 191,000 M-dwarf stars will be observed by TESS during its prime mission. As of March, 2022 and as shown in Figure 1.4, there are $\sim$100 exoplanets with M-dwarf host stars within 1,000 parsecs of the Sun, but this number is likely to be much larger given the fact that the vast majority of the stars in our galaxy are understudied M-dwarfs.

---

[4] https://heasarc.gsfc.nasa.gov/docs/tess/the-tess-space-telescope.html#bandpass
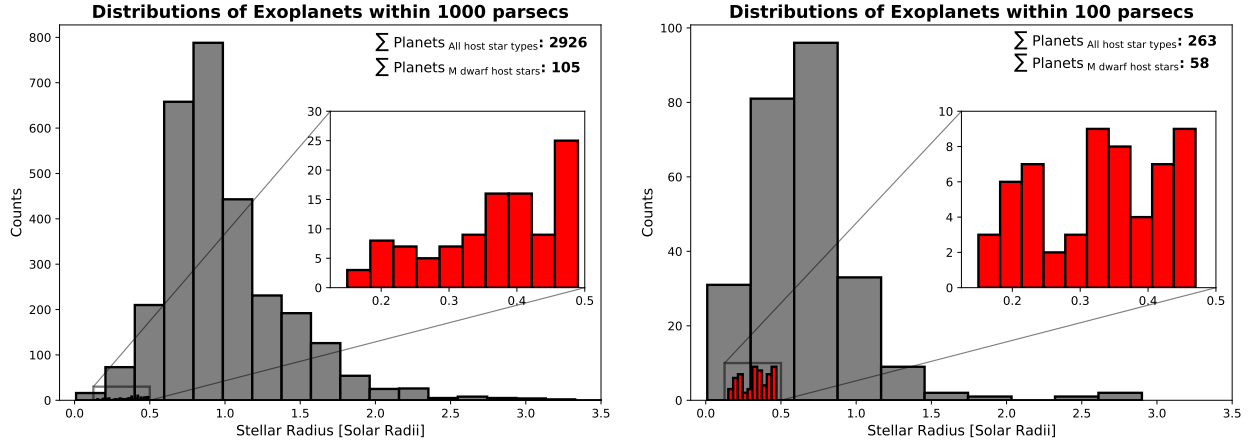
Figure 1.4: Histogram of stellar radii of exoplanet host stars within 1,000 and 100 parsecs. The distribution of stellar hosts of all spectral types are shown in grey and the distribution of M-dwarf stars are shown in red.
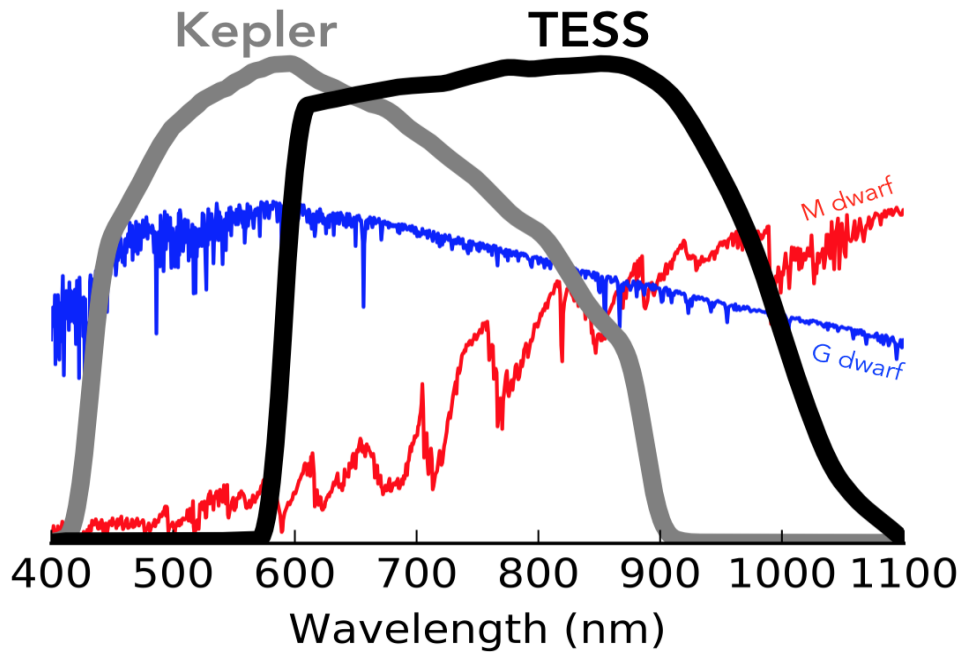
Figure 1.5: A comparison between the spectral bandpasses of the Kepler (grey line) and TESS (black line) space telescopes[4]. For reference, the simulated spectra of G & M dwarfs are also shown in blue and red lines, respectively. TESS will monitor a much larger sample of M stars compared to Kepler, thus the bandpass extends further to red wavelengths. Image Credit: Zach Berta-Thompson with data from Sullivan et al. 2015.

An outline of the remainder of this dissertation is as follows. Chapter 2 describes an extensive transit survey of the closest M-dwarf star, Proxima Centauri. Proxima Centauri hosts an exoplanet with a minimum mass of $\sim$1.3 M$_\oplus$ which was discovered by Anglada-Escudé et al. 2016 with the

13

radial velocity method. In the first project of this work, I present the analysis of 329 ground-based observations of Proxima Centauri spanning from 2006–2017. In Chapter 3, I continued the second project of this work where I analyzed our ground-based observations to explore if any transits in the period range of 1–30 days could be detected. In Chapter 4, I present an analysis of 33,054 M-dwarf stars, located within 100 parsecs, via the TESS full-frame images (FFIs) of observed sectors 1–5. I present a new pipeline called NEMESIS, developed to extract detrended photometry, and to perform a search for transit-like events in single-sector data in TESS FFIs. In this work, we detect 183 threshold crossing events and present 24 new planet candidates. In Chapter 5, I present currently ongoing and future work and summarize the results of this dissertation.

Chapter 2

A Multi-year Search for Transits of Proxima Centauri I: Light Curves Corresponding to Published Ephemerides

This chapter originally published as Blank et al. 2018 in *The Astrophysical Journal*.

Abstract

Proxima Centauri has become the subject of intense study since the radial-velocity discovery by Anglada-Escudé et al. 2016 of a planet orbiting this nearby M-dwarf every ~ 11.2 days. If Proxima Centauri b transits its host star, independent confirmation of its existence is possible, and its mass and radius can be measured in units of the stellar host mass and radius. To date, there have been three independent claims of possible transit-like event detections in light curve observations obtained by the MOST satellite (in 2014–15), the BSST telescope in Antarctica (in 2016), and the Las Campanas Observatory (in 2016). The claimed possible detections are tentative, due in part to the variability intrinsic to the host star, and in the case of the ground-based observations, also due to the limited duration of the light curve observations. Here, we present preliminary results from an extensive photometric monitoring campaign of Proxima Centauri, using telescopes around the globe and spanning from 2006 to 2017, comprising a total of 329 observations. Considering our data that coincide directly and/or phased with the previously published tentative transit detections, we are unable to independently verify those claims. We do, however, verify the previously reported

ubiquitous and complex variability of the host star. We discuss possible interpretations of the data in light of the previous claims, and we discuss future analyses of these data that could more definitively verify or refute the presence of transits associated with the radial-velocity discovered planet.

2.1 Introduction

Neptune-like and lower mass planets are common around M dwarfs; a result predicted in simulations (Laughlin et al., 2004; Ida & Lin, 2004; Montgomery & Laughlin, 2009), validated within a factor of $\sin i$ in radial-velocity (RV) observations (e.g. Bonfils et al. 2005, 2013), and now confirmed by Kepler transit work (Dressing & Charbonneau, 2013, 2015; Morton & Swift, 2014). This is of great interest since M dwarfs far outnumber other stellar types and terrestrial analogs with orbital periods of only a few days to a few weeks could still have an Earth-like climate, despite being tidally locked (Joshi et al., 1997) or subject to high UV flux (France et al., 2013), though such factors make it almost certain that the exoplanet history will be very different than that of Earth (Lopez et al., 2012; Ramirez & Kaltenegger, 2014; Luger et al., 2015). Such planets would be prime candidates in searches for spectroscopic evidence of life by space-born missions (see Tarter et al. 2007 and Shields et al. 2016 for useful reviews).

The discovery of Proxima Centauri b (Proxima b, hereafter) claimed by Anglada-Escudé et al. 2016 (A2016, hereafter) in an 11.2 day habitable zone (Kopparapu et al., 2013) orbit of its host star is important because the planet would likely be a rocky (Brugger et al., 2016; Kane et al., 2017; Bixel & Apai, 2017) and possibly habitable world (Ribas et al., 2016; Barnes et al., 2016; Meadows et al., 2016; Turbet et al., 2016; Boutle et al., 2017) orbiting our nearest-known stellar neighbor. The main source for the uncertainty in the nature and habitability of Proxima b is that only its lower mass limit of 1.27 $M_\oplus$ (A2016) is reported since it was discovered using the RV technique. If Proxima b transits its host star, independent confirmation of its existence is possible,

and its mass and radius can be measured in units of the stellar host mass and radius. Thus, it would be possible to infer bulk composition (Lopez & Fortney, 2014; Weiss & Marcy, 2014; Rogers, 2015; Chen & Kipping, 2017), which in turn impacts the question of habitability. Damasso & Del Sordo 2017 (D2017, hereafter) reanalyzed the RV data and provided a refined ephemeris (see Section 2.4).

There have been searches for transiting planets orbiting Proxima Centauri (Proxima, hereafter) from both space-based (Kipping et al., 2017) and ground-based (Liu et al., 2017; Li et al., 2017) observatories, but no convincing transit candidates were found. However, Kipping et al. 2017 (K2017, hereafter) and Liu et al. 2017 (L2017, hereafter) describe tentative transit-like event detections compatible with the RV orbit, and K2017 and Li et al. 2017 (Li2017, hereafter) describe potential transit-like detections that are incompatible with the RV orbit.

We have been conducting a search for transiting planets orbiting Proxima since 2006 as part of our Global Earth M-dwarf Search Survey (GEMSS)[5]. As was pointed out in Shankland et al. 2006 and Nutzman & Charbonneau 2008, sub-meter diameter telescopes with commercial grade CCD cameras provide sufficient photometric precision to detect transiting terrestrial-type exoplanets around mid- and late-M dwarfs. For example, Proxima b is predicted to have a radius between 0.9 and 1.4 $R_\oplus$ (Brugger et al., 2016), which would produce a detectable transit with a depth in the range of $0.5 - 1.3\%$. The observations from the first year of GEMSS operation are described in Blank et al. 2007[6].

The observations reported in Section 2.8 are the basis of two studies. In this work, we examine the question of whether Proxima b transits, specifically in the context of the three published RV ephemerides (A2016, K2017, D2017) and in the context of tentative transit-like detection claims by K2017, L2017 and Li2017. Section 2.2 summarizes the recent claims in the literature that we

---

specifically examine in this work. Section 2.8 presents our new observations and data reduction methodology. The results, discussion, and summary of conclusions are provided in Sections 2.10, 2.11, and 2.12, respectively.

In Feliz. et al. 2019, (Paper II, hereafter), we will present a more general transit search based on our Proxima data, including a search of ephemerides beyond those recently claimed, and we provide an analysis of the sensitivity of our data relative to various configurations of periodic transit events.

2.2 Recent Claims in the Literature to be Examined in this Work

The claim of an RV-detected planet in the habitable zone of Proxima by A2016 led to rapid and increased attention to this system, especially in the hopes of identifying possible transits associated with Proxima b. In this section and in Table 2.1, we summarize the original and re-analyzed RV claims and associated predicted ephemerides and the claims of tentative transit-like event detections. Then, using our own extensive light curve observations presented in Section 2.8, we analyze the reported detections in Section 2.10. We emphasize that the photometry-based claims described below are low significance tentative detections, especially considering the apparent intrinsic variability of Proxima, and are not generally claimed by the reporting authors as confirmation of a planet transiting Proxima.

Table 2.1: Literature Ephemerides Investigated

Reference	Data Source	Period (d)	T_0 - 2450000 (BJD$_{TDB}$)	Depth (%)	Duration (min)
A2016	RV data & analysis	$11.186^{+0.001}_{-0.002}$	1634.73	est. 0.5	-
K2017	RV ephemeris re-analysis	11.1856 ± 0.0013	6678.78 ± 0.56	est. $0.48^{+0.14}_{-0.11}$	$[76.4]^1$
	MOST data, Model $\mathcal{M}_1$, Signal S	$11.18467^{+0.002}_{-0.00039}$	$6983.1663^{+0.00648}_{-0.0329}$	[1.06]	[64.8]
	MOST data, Model $\mathcal{M}_2$, Signal C	$11.18725^{+0.00012}_{-0.00016}$	$6980.0573^{+0.00156}_{-0.00344}$	[0.84]	[64.1]
D2017	RV re-analysis	$11.1855^{+0.0007}_{-0.0006}$	$7383.71^{+0.24}_{-0.21}$	-	-
L2017	MOST Signal C + BSST light curve	11.18858	6801.0439	0.48 ± 0.09	82.6 ± 5.3
Li2017	Las Campanas 30 cm Robot light curve	$2 - 4$	$7626.563554^{0.001582}_{0.002355}$	0.46	~ 60

Note – Quantities in square brackets were calculated from model and stellar parameters provided in K2017. All T_0 values have been converted to BJD$_{TDB}$ (Eastman et al., 2010) and all transit depths have been converted to percent.
[1]To determine the transit duration listed for the K2017 RV-based ephemeris, we assumed an impact parameter, $b = 0$, and eccentricity, $e = 0$, and stellar properties $M_\star = 0.123\,\mathrm{M_\odot}$, $R_\star = 0.145\,\mathrm{R_\odot}$ (Demory et al., 2009) and nominal planetary radius $R_P = 1.06\,\mathrm{R_\oplus}$ from K2017 Section 3.2.

2.3   A2016

A2016 report the discovery of Proxima b based on a total of 216 RV observations collected over 16 years. A subset of 54 RV observations were concentrated in a $\sim$75 day period in 2016. The RV data showed a periodic signal with reference epoch $T_0 = 2451634.73146\,\mathrm{JD_{UTC}}$, a Doppler semi-amplitude K $\sim 1.38 \pm 0.21\,\mathrm{m\,s^{-1}}$, eccentricity e < 0.35, and period P $= 11.186^{+0.001}_{-0.002}$ days, which is stable over $\sim$16 years. The corresponding minimum planet mass is $\sim$1.27 M$_\oplus$, and the probability of a transit orientated orbit is 1.5%. Based on the minimum mass and an Earth-like density, the predicted transit depth is $\sim 0.5\%$. Evidence is also found for an additional periodicity in the RV data in the range of $60 - 500$ days.

2.4   D2017

D2017 undertook a re-analysis of the RV data reported by A2016 using a Gaussian process (GP) framework to mitigate the stellar correlated noise in the RV time-series. The analysis resulted in a revised orbital period P $= 11.1855^{+0.0007}_{-0.0006}$ days, reference epoch $T_0 = 2457383.71^{+0.24}_{-0.21}$ JD$_{UTC}$, eccentricity e $= 0.17^{+0.21}_{-0.12}$, and Doppler semi-amplitude K $\sim 1.48^{+0.13}_{-0.12}\,\mathrm{m\,s^{-1}}$. Their anal-

ysis dismisses the possibility of an additional planet signal in the A2016 RV data.

2.5   K2017

K2017 present broadband optical photometric observations of Proxima obtained with the MOST space telescope made over 12.5 days in 2014 ($\sim$2600 time-series observations) and 31 days in 2015 ($\sim$13000 observations). K2017 also re-analyzed the A2016 RV data and extracted a new RV ephemeris with $T_0 = 2456678.78 \pm 0.56$ HJD and orbital period $P = 11.1856 \pm 0.0013$ days. K2017 use a GP+transit model with an uninformative prior on transit phase (model $\mathscr{M}_1$) that yields four transit epochs within the MOST time-series, although one of these occurs during a data gap. This detection is referred to as signal S after phase-folding. The ephemeris derived from the events has $T_0 = 2456983.1656^{+0.0064}_{-0.0330}$ HJD, which is more than 4σ from the RV ephemeris prediction, and $P = 11.18467^{+0.00200}_{-0.00039}$ days. K2017 state that the observed event mid-points are "difficult to reconcile with the radial velocity solution."

Using a GP+transit model with an informative prior on transit phase (model $\mathscr{M}_2$) yields two events (at $\sim$2456801.06 and $\sim$2457159.05 HJD). This detection is referred to as signal C after phase-folding. The ephemeris derived from signal C has $T_0 = 2456980.0554^{+0.0027}_{-0.0023}$ HJD, which is 1.5σ consistent with the RV ephemeris, and $P = 11.18725^{+0.00012}_{-0.00016}$ days. A similar model which also includes an informative prior on the radius of the planet (model $\mathscr{M}_3$) finds the same signal. K2017 conclude that HATSouth data moderately disfavor the existence of signal C at the $1-2\sigma$ level.

Finally, $\mathscr{M}_2$ was run a total of 100 times while iteratively translating the prior on T_0 by 0.01P, which effectively searches the full phase of the period for transit signals. This search yields three new events that are referred to as signal T after phase folding. Over 95% of the posterior trials

correspond to a grazing geometry, which is also evident from the V-shaped morphology of signal, which favors a large planet that is highly incompatible with the `Forecaster` prediction. K2017 assert that signal T would not be considered a detection even if its phase had been compatible with the RV ephemeris, so we do not consider it further in this work.

To allow for comparison with other claimed transit-like detections, we calculate transit depth and duration for signals S and C from the model $\mathcal{M}_1$ and $\mathcal{M}_2$ parameters, respectively, and include the results in Table 2.1.

2.6   L2017

L2017 report photometric observations from the Bright Star Survey Telescope (BSST) located at the Chinese Antarctic Zhongshan Station. Ten nights of observations were obtained from 29 August to 21 September, 2016. They detect with 2.5σ confidence a transit-like event with $T_C = 2457640.1990 \pm 0.0017$ HJD, which is $\sim 1\sigma$ from the K2017 and $\sim 2\sigma$ from the D2017 RV predicted ephemerides. This event occurs 138 min later than predicted by the K2017 model $\mathcal{M}_2$ ephemeris.

Fitting a linear ephemeris to the two tentative K2017 signal C events and the L2017 event yields a new ephemeris with a period of $P = 11.18858$ days and $T_0 = 2456801.0439$ HJD (adopting the first T_{lin} value in their Table 2). The resulting transit timing variations (TTVs) relative to the linear ephemeris are in the range of $17 - 39$ minutes. L2017 calculate that an Earth-mass planet orbiting near a 2:1 or 3:2 mean motion resonance with Proxima b is able to produce TTVs $\gtrsim 30$ minutes while keeping Proxima's RV$< 3\,\text{m s}^{-1}$.

2.7 Li2017

Li2017 report one potential transit with a depth of $\sim 0.5\%$ in photometric observations made over 23 nights with a robotic 30-cm telescope at Las Campanas Observatory. The modeled mid-transit time is $T_C = 2457626.5635537^{+0.0015813}_{-0.0023548}$ BJD_{TDB} and the duration is about one hour. Li2017 show that if the event is indeed caused by a planet transiting Proxima, the transit model prefers a $2-4$ day orbit. Furthermore, the planet mass would need to be $< 0.4\,M_\oplus$ to avoid detection by the A2016 RVs.

2.8 New Observations and Reductions

2.8.1 Observations

We have conducted an extensive photometric monitoring campaign of Proxima using multiple ground-based observatories from 2006 to 2017. The campaign conducted observations routinely each year, except for a gap in observations from 2009 to 2012. In total, we obtained 329 nights of time-series photometric observations that resulted in light curves of at least 1.5 hours in duration (most are 3–8 hours in duration) after data processing and cleaning (see Section 2.9). In this section, we describe the observations, which are summarized in Table 2.2. To the best of our knowledge, this is the longest duration transit study of Proxima to date.

In the present work, we restrict our analyses to a subset of 96 observations that coincide with the predicted times of transit from previously published claims (see Section 2.2 and Table 2.1). The 96 light curves are presented in Appendix A and will be provided along with the full set of light curves in machine readable format in Paper II.

Table 2.2: Summary of Photometric Observations Analyzed in this Work and in Paper II

Telescope Name	Aperture	FOV	Plate-Scale	Start Date	End Date	Exp. Time	Filter	# Obs
	(m)	(arcmin^2)	(arcsec pixel^{-1}	(UT)	(UT)	(sec)		(nights)
RAE	0.35	10.4×10.4	1.2	2006 May 24	2008 Feb 25	20	R	23
RCOP	0.4	24.2×16.3	0.76	2014 Feb 13	2014 Aug 23	16-20	R	30
Prompt 1	0.4	9.64×9.64	0.9	2013 Aug 17	2015 Apr 22	16-20	R	40
Prompt 2	0.4	21×14	0.41	2013 Aug 21	2017 Mar 07	15–20, 65	R,G	50
Prompt 4	0.4	10×10	0.59	2014 Mar 07	2015 May 11	15-20	R	50
Prompt 5	0.4	10.25×10.25	0.59	2014 Mar 16	2016 Mar 29	18-20	R	10
Prompt 8	0.6	22.6×22.6	0.69	2014 Jun 20	2015 Mar 15	16-18	R	3
Prompt SS01	0.42	15.6×15.6	0.9	2014 Feb 23	2015 May 05	15-20	R	46
Prompt SS02	0.42	15.6×15.6	0.9	2014 Feb 23	2014 Jul 30	17-20	R	18
Prompt SS03	0.42	15.6×15.6	0.9	2014 May 08	2014 Aug 14	15-20	R	40
Prompt SS04	0.42	15.6×15.6	0.9	2013 Sep 02	2013 Sep 13	20	R	2
Hazelwood	0.32	18×12	0.73	2017 Mar 18	2017 Jun 16	5-12	Ic	6
Ellinbank	0.32	20.2×13.5	1.12	2017 Jun 16	2017 Jul 30	14-18	R	5
Mt. Kent CDK700	0.7	27.3×27.3	0.40	2017 Jun 20	2017 Jul 25	20-25	I	3
ICO	0.235	16.6×12.3	0.62	2017 Mar 18	2017 May 14	15-30	I	3

2.8.2 Observing Strategy

Because our survey started in 2006, almost all of our observations were conducted before the A2016 RV-discovered planet was announced. Thus, we were generally conducting a blind search for transits of Proxima through 2016. After the RV ephemeris was announced, we targeted the D2017 predicted times of transit, allowing for about a day of uncertainty in the transit window.

Proxima is known to be a flare star (Shapley, 1951; Walker, 1981), and M-dwarf flares are known to be much brighter in blue passbands compared to red passbands (Kowalski et al., 2016). Although Proxima's flares are prominent across the UV and optical bands, they are indeed stronger in the blue compared to the underlying stellar photosphere (Walker, 1981), so we targeted the *R* passband and redder to minimize the impact on our photometric observations. Even so, contamination from systematics, flares, and low energy flares that are now predicted to occur about every ~ 20 minutes at the 0.5% level (Davenport et al., 2016), is significant in our photometric data. Thus we needed a large number of observations to help improve the sensitivity of our data to periodic transit signals predicted to have a depth similar to the amplitude of variations common in our data.

2.8.3   Perth Observations

Our 2006 to 2008 observations were obtained using the Real Astronomy Experience (RAE) Robotic Telescope at the Perth Observatory in Bickley, Western Australia, which was primarily used for astronomy education in the "Hands on Universe" program (Fadavi et al., 2006)[7]. The telescope was a Schmidt-Cassegrain design with an aperture of 0.35 m and was equipped with an Apogee Ap7 CCD camera and $BVRI$ filters. Despite having a plate scale of $1.2''$ pixel^{-1}, the seeing was generally at least $3''$, so under-sampling was not typically a problem. The RAE telescope was not guided, so periodic re-pointing of the telescope by the robot was required to keep the field centered on the detector. Additional telescope specifications are provided in Table 2.2.

The RAE observations were conducted in an R filter with exposure times of 20 seconds. The CCD readout time was 11 seconds, yielding an effective cadence of 31 seconds per exposure. Proxima was the brightest star in the RAE field and the ADU counts varied between 22,000 and 35,000, which ensured that the frames were not saturated but still well exposed. Bias, dark, and flat-field frames were applied automatically to each science exposure by the telescope system. The telescope was operated remotely through the internet.

2.8.4   Skynet Observations

The great bulk of our observations were obtained using the Skynet world-wide network of remotely operated 0.4 m and 0.6 m telescopes (Reichart et al., 2005). Our observations were obtained using telescopes located at Cerro Tololo, Chile (Prompt 1, 2, 4, 5, and 8), Siding Springs, New South Wales, Australia (Prompt SS01, SS02, SS03, and SS04) and Perth, Western Australia (referred to as RCOP, hereafter). All of our observations were obtained with the 0.4 m telescopes, except for three observation runs with the 0.6 m Prompt 8 telescope. In general, the Skynet telescopes were not guided, so periodic re-pointing of the telescope by the robot was required to keep

---

[7] https://handsonuniverse.org/

the field centered on the detector. Additional Skynet telescope specifications are included in Table 2.2.

Frames were exposed in an *R* filter with integration times ranging from 15 to 20 s, except for one 2017 Prompt 2 observation with an integration time of 65 s, which used a generic green filter (listed as G in Table 2.2). We adopted the standard Skynet calibrated data, which includes dark, bias, and flat-field corrections.

2.8.5   KELT-FUN Observations

We collected observations from the Kilodegree Extremely Little Telescope (KELT; Pepper et al. 2007, 2012) Follow-Up Network (KELT-FUN; Collins et al. 2018) based on the A2016 RV-based ephemeris. We used the `Tapir` software package (Jensen, 2013) to schedule the KELT-FUN observations. KELT-FUN members contributed a total of 18 light curves from March, 2017 to July, 2017. The KELT-FUN observations are identified in Table 2.2 as Hazelwood, Ellinbank, Mt. Kent CDK700, and Ivan Curtis Observatory (ICO). The single Prompt 2 G-band observation in March of 2017 was also contributed by a KELT-FUN member using Skynet time allocated to the KELT project. KELT-FUN telescope specifications are included in Table 2.2. Image calibration included dark, bias, and flat-field corrections.

2.9   Data Reduction

To achieve the photometric precision needed to detect a $\sim 0.5\%$ transit-like event in our ground-based observations, we require differential photometry to compensate for the adverse effects of the

atmosphere. However, it is difficult to directly compare differential photometry across multiple nights and multiple telescopes due to telescope pointing inaccuracies combined with imperfect flat-field compensation, long term changes in comparison star brightness, differences in the comparison stars available on the detector, chromatic differences in atmospheric transparency, differences in atmospheric scintillation, changes in telescope focus, etc. In our case, telescope guiding was not implemented for the RAE and Skynet observations, so the significant changes in the placement of the field on the detector throughout a time-series limited the number of comparison stars available on the detector for the entire sequence. Fewer comparison stars generally results in lower photometric precision and higher levels of systematics. The comparison star ensemble problem would typically be compounded across multi-night differential photometry, if trying to use the same ensemble to directly compare the differential light curves, so we allowed for different comparison star ensembles for each night of observations.

To overcome the different calibration of the multi-night differential photometry, we chose to process and then normalize each light curve separately, such that the final mean value is 1.0. We discuss the data processing below. While normalizing the observations allows a direct comparison of multi-night light curves, we acknowledge that a real event could be obscured if the duration is longer than $\sim 50\%$ of the duration of the light curve. To minimize this issue, we generally required light curves to be at least ~ 2.5 hours long before data processing. In some cases, data processing reduced the light curve duration, so we set a hard lower limit of 1.5 hours of coverage and dropped light curves with a shorter final duration.

AstroImageJ (AIJ; Collins et al. 2017) was used to perform differential photometry on all data sets. The images for each night were inspected manually and frames contaminated with aircraft, satellite, clouds, etc, that might cause photometric inaccuracies, were discarded. In general, we find that selecting comparison stars that have $\pm 50\%$ of the brightness of the target star produces the least systematics in the target star light curve. In addition, we generally find that balancing the

number of ensemble integrated counts from comparison stars fainter and brighter than the target star reduces light curve systematics even more. However, Proxima is the brightest star in the field of our detectors in our filter bands, so only fainter comparison stars were available for the ensemble. For this work, we first selected all comparison stars that are at least 50% as bright as Proxima. However, in many cases (in particular for the RAE and Skynet telescopes with relatively small fields of view), only one or two comparison stars with the desired brightness were available on the detector throughout the time series, so we generally selected the ~ 5 brightest stars available for the ensemble, avoiding stars that showed significant variability. For most image sequences, we used an aperture with an 8 pixel radius, but the radius varied depending on differences in detector pixel scales, seeing, and telescope focus.

To minimize the effects of chromatic differential airmass trend and long term stellar variability, we assumed a flat light curve model and performed a linear detrend using, at a minimum, airmass and time. In some light curves with a strong correlation between the x- and/or y-centroid of the target star location on the detector and variability in the light curve, we performed a linear detrend using the x- and/or y-centroid locations of the target star. In some cases we detrended using sky background, full-width half-maximum of the stellar point spread function, and/or the total number of comparison star net integrated counts. If a telescope meridian flip or tracking jump resulted in an correlated change in the photometric baseline, we fitted and realigned the baseline at that point. This method of detrending will help to minimize false event detections due to potentially large step functions at the ends of individual light curves when we perform our periodic transit search for Paper II. The normalizing and detrending process also minimizes the effects of Proxima's 82.6 ± 0.1 day rotation period (Collins, J. M. et al., 2017) and seven year stellar cycle (Wargelin et al., 2017). While we acknowledge that detrending using this method may reduce or enhance the significance of transit-like events, we have visually compared each undetrended light curve with its detrended version, and can confirm that the adverse affects are minimal. In Paper II or a followup paper, we also intend to investigate de-weighting data near the edges of individual light curves to potentially

reduce the need for detrending and/or to improve the periodic transit search results.

The light curves have between 79 and 1468 data points each, with an average of 483 data points. Assuming perfectly Gaussian distributed data sets containing 79, 483, and 1468 data points, Chauvenet's criterion (Chauvenet, 1960) specifies that values beyond 2.7, 3.3, and 3.7σ from the mean, respectively, should be considered outliers. Therefore, to remove large flares and other photometric outlier data points, we elected to perform a uniform iterative 3σ cut on each individual light curve using AIJ. After each $> \pm 3\sigma$ outlier point was removed, AIJ detrended and normalized the data again, and the process was repeated until no 3σ outlier data points remained. We visually inspected each light curve before and after the cuts to verify that the cleaning operation did not remove any obvious transit-like events in our data. After very strong flares, we also removed additional data points in the light curve that were not removed by the 3σ cut, but that were obviously affected by the rising or decaying flare signal. We also removed short segments of data that were separated in time from the main cluster of data, and that likely did not share the same baseline differential flux value due to a telescope meridian flip or a large instantaneous shift of the field on the detector.

After the data were cleaned, 329 light curves (167,445 photometric data points) having a duration of 1.5 hours or longer remained in our sample. Even after detrending and 3σ cleaning of the light curves, some had very large oscillatory or other variations that were not consistent with a transit signal, or would have prevented detection of an underlying $\sim 0.5 - 1.0\%$ transit-like event. We sought to exclude these light curves using a statistical cut.

Figure 2.1 shows a histogram of the 329 standard deviations of the individual cleaned and detrended light curves. The standard deviations range from $\sim 0.17 - 1.5\%$ and have a median value of 0.516%. The distribution has a standard deviation of 0.23%. The light curves with standard deviation above the distribution's median value plus the distribution's standard deviation (0.746%) were flagged to be removed from the analysis. We examined each of the flagged light curves and

found that several had large standard deviation due to either a transit-like event (although generally deeper than predicted for Proxima b) or a relatively flat light curve with white-noise-like scatter above the threshold. We retained those two types of light curves in our sample, despite the large standard deviation. Two examples of light curves retained in our sample, despite being above our standard deviation threshold are shown in Figure 2.2. The final light curve count in our study sample is 262, which includes a total of 127,733 photometric data points.
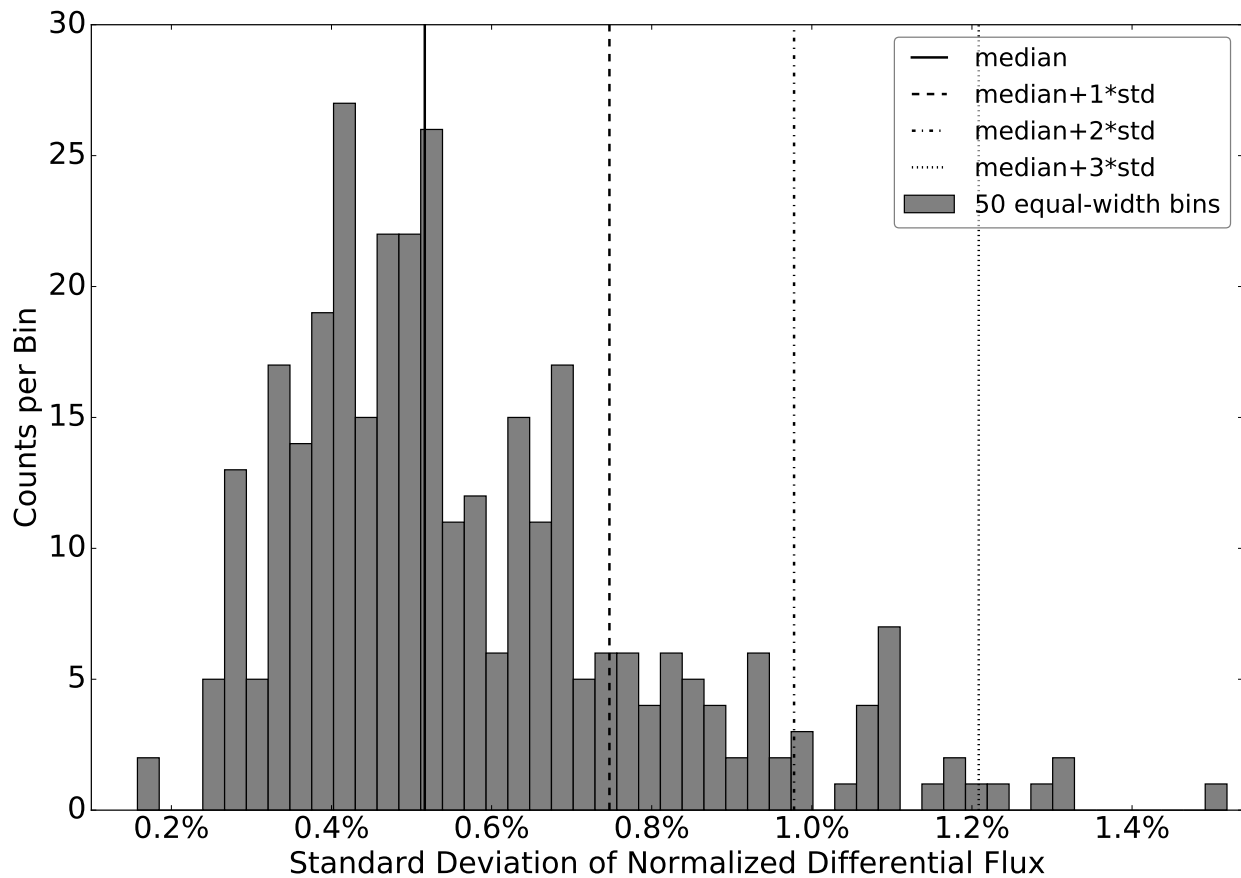
Figure 2.1: Histogram of the standard deviations of our 329 individual light curves. The solid line marks the median of the distribution at 0.516%. The distribution has a standard deviation of 0.23%. The long-, medium-, and short-dashed lines mark the values of median plus 1, 2, and 3 times the standard deviation, respectively.
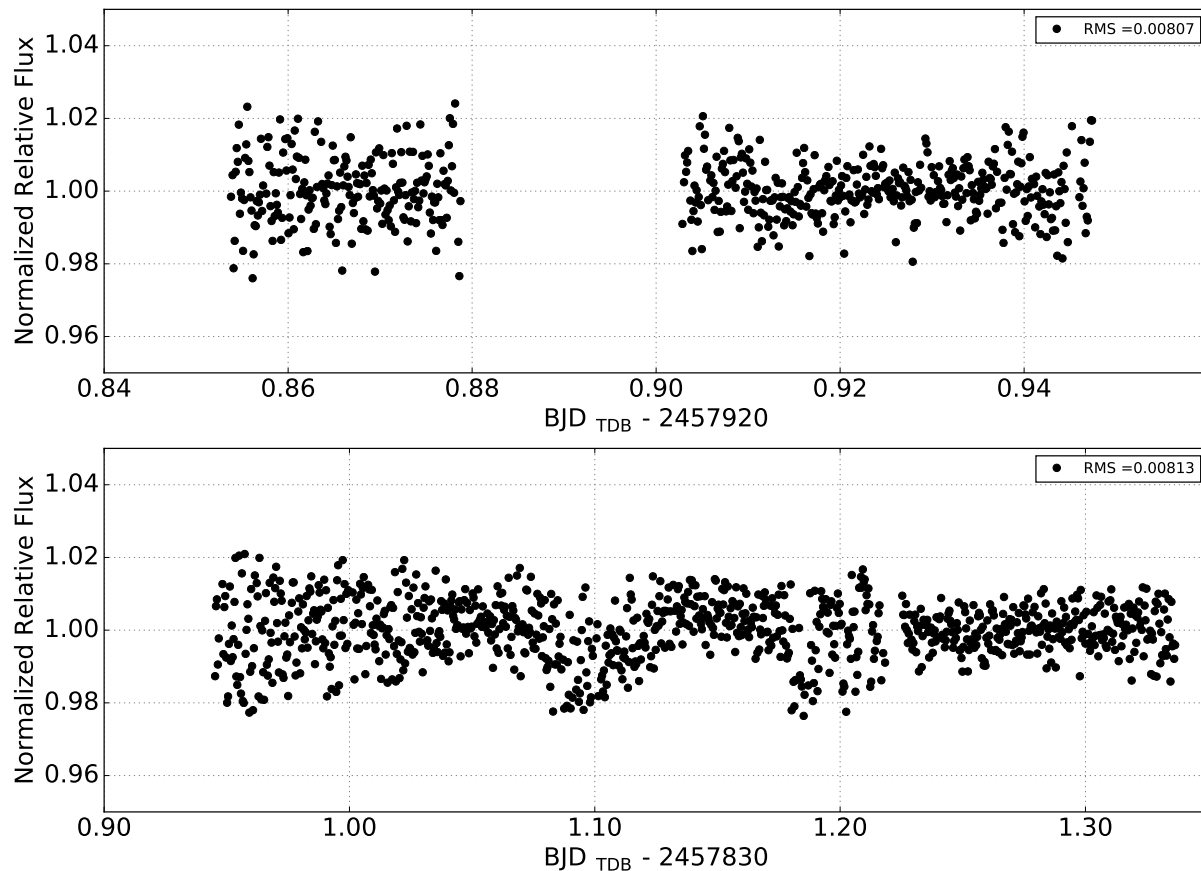
Figure 2.2: Example light curves retained in our data set, despite having standard deviation above our threshold. (Top Panel) The KELT-FUN Hazelwood Observatory light curve from UT 2017 June 16 is relatively flat but has scatter above our threshold. (Bottom Panel) The KELT-FUN ICO light curve from UT 2017 March 18 has a transit-like feature that contributes to the high scatter.

2.10   Results

From the 262 light curves in the final sample, Appendix A describes and displays the subset of 96 light curves that coincide with the published ephemerides described in Section 2.2 and Table 2.1. The full set of 262 light curves and their analysis will be presented in Paper II.

2.10.1 Light Curves in Relation to RV-based Ephemerides

In total, there are 85 light curves from the final sample that contribute data within 2σ of the K2017 RV-based ephemeris. The light curves are phased to the K2017 RV-based ephemeris and displayed in the Appendix A, along with the K2017 MOST light curves and the L2017 BSST light curves. The vertical scale of the light curves in Appendix A is compressed to accommodate the large number of light curves. To elucidate the level of post-detrended residual variations in the light curves, Figure 2.3 shows a subset of 19 light curves that fall within 2σ of the K2017 RV-based ephemeris.

Each light curve has been shifted on the vertical axis for clarity, and date of observation and telescope identification, as defined in Section 2.8 and Table 2.2, are displayed on the right-hand vertical axis. The light curve data are binned in 5 minute intervals. The center of Figure 2.3, labeled as phase zero, corresponds to the nominal predicted transit center at each epoch of displayed data according to the K2017 RV-based ephemeris. The grey vertical bars at $\sim \pm 1.2$ days span the width of the 2σ uncertainty, and varies depending on the amount of time since the reference epoch, T_0, due to the cumulative uncertainty in the period.

Also shown are the transit centers at each displayed epoch, extracted from the other literature ephemerides listed in Table 2.1, after phasing to the K2017 RV-based ephemeris. The transit centers predicted by the A2016 RV-based ephemeris are displayed as blue vertical lines. The nominal A2016 transit centers are inconsistent with the K2017 RV-based ephemeris at a level of $\sim 1.5\sigma$, primarily due to an offset in the reference epoch. The transit centers predicted by the D2017 ephemeris are displayed as magenta vertical solid lines. The D2017 ephemeris is highly consistent with the K2017 RV-based ephemeris, relative to the uncertainty. The K2017 Signal C and L2017 ephemerides are shown as black and light blue vertical bars, respectively. Both sets of predicted transit centers precede the K2017 RV-based ephemeris by about 1σ.

The light curves exhibit a variety of behaviors. In some cases there is no clear evidence for a transit, within the noise of the data (e.g., light curves "20140329 Prompt1" and "20140730 SS02"). In other cases, there is some variability of amplitude comparable to that found by other authors, but which does not have a shape that is generally consistent with a transit, or more specifically, with the previously claimed transits (e.g., light curves "20070508 RAE" and "20170307 ICO"). Finally, there are some cases in which there is variability observed that could potentially be regarded as consistent with the previously claimed transit-derived models, although the transit center phase is not consistent with the models (e.g., light curve "20140514 Prompt2").
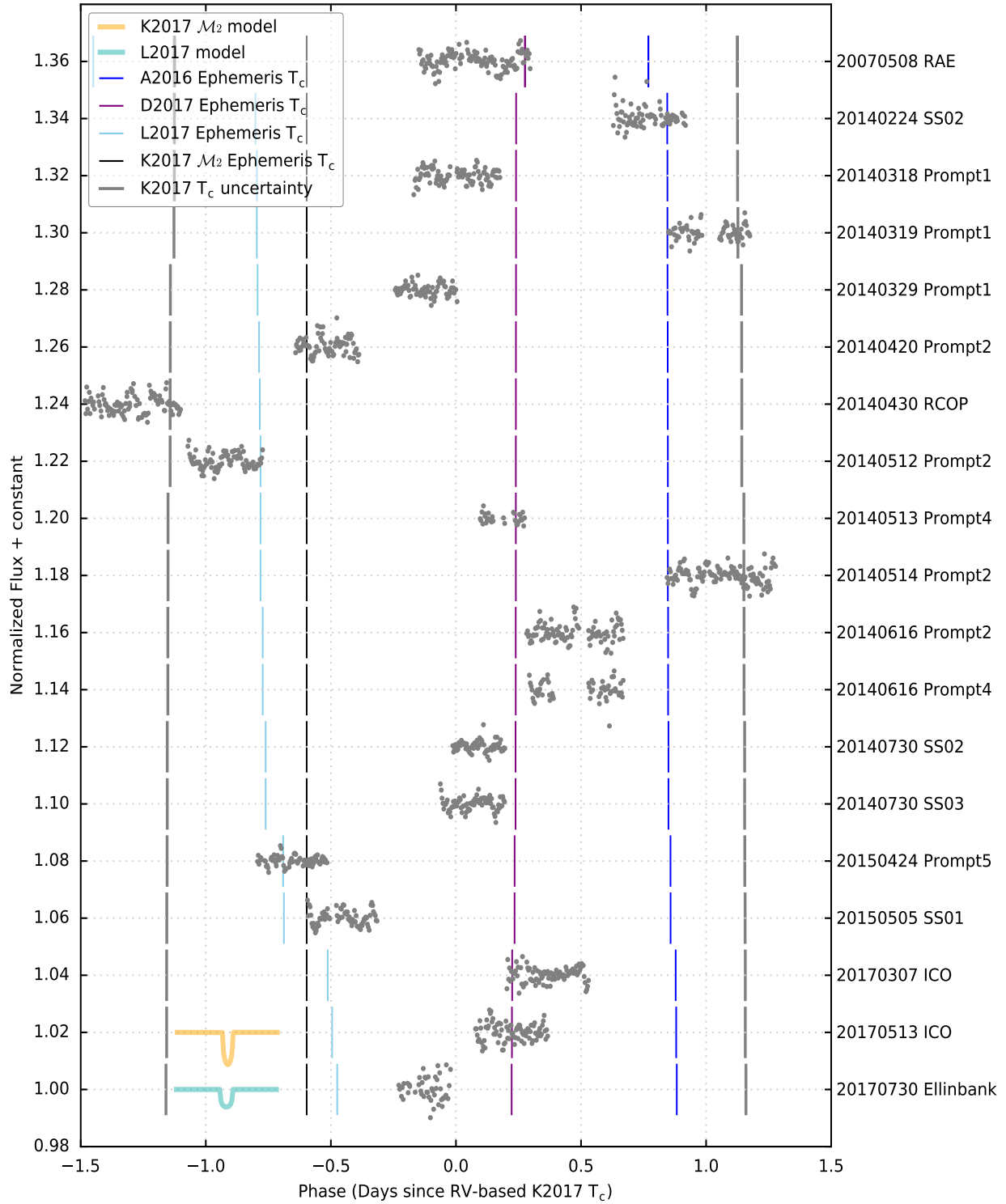
Figure 2.3: A subset of 19 light curves from this work phased to the K2017 RV-based ephemeris. The nominal transit center times predicted by the K2017 RV-based ephemeris are located in the center of the figure at phase zero. The grey vertical solid lines mark the $\pm 2\sigma$ uncertainty in the ephemeris. The blue, magenta, light blue and black vertical solid lines mark the transit center times predicted by the ephemerides of A2016, D2017, L2017, and the K2017 model $\mathcal{M}_2$ (Signal C), respectively. The K2017 $\mathcal{M}_2$ and L2017 models are shown to scale in the lower left corner as solid orange and light green solid lines, respectively. All 85 light curves contributing data within $\pm 2\sigma$ of the K2017 RV-based ephemeris are presented in Appendix A.

Since the 2σ uncertainty in the RV-based transit ephemerides corresponds to a time window of approximately ± 1.2 days, the ground-based light curve observations presented here cannot individually span the entire time window within which transits might be expected to occur. However, after combining and phase-folding all 85 light curves from this work, the full $\pm 2\sigma$ phase range has complete coverage. Figure 2.4 shows the full phase range with the data from this work displayed as grey dots. The data are combined and binned at five minute intervals and displayed as magenta dots. The K2017 MOST data are also displayed as black squares, and the L2017 BSST data are shown as light blue triangles. The K2017 Signal C transit models are displayed as solid orange lines. The L2017 BSST transit model is displayed as a solid brown line. There are no obvious transit signals, at the depth of the plotted models evident within the noise of binned data. Note, however, that the significance of any transit signals following the other ephemerides described in Section 2.2 would be significantly reduced due to the skewing of the transit alignments as a result of the slightly different periods compared to the K2017 RV-based ephemeris used to phase the data and transit models.
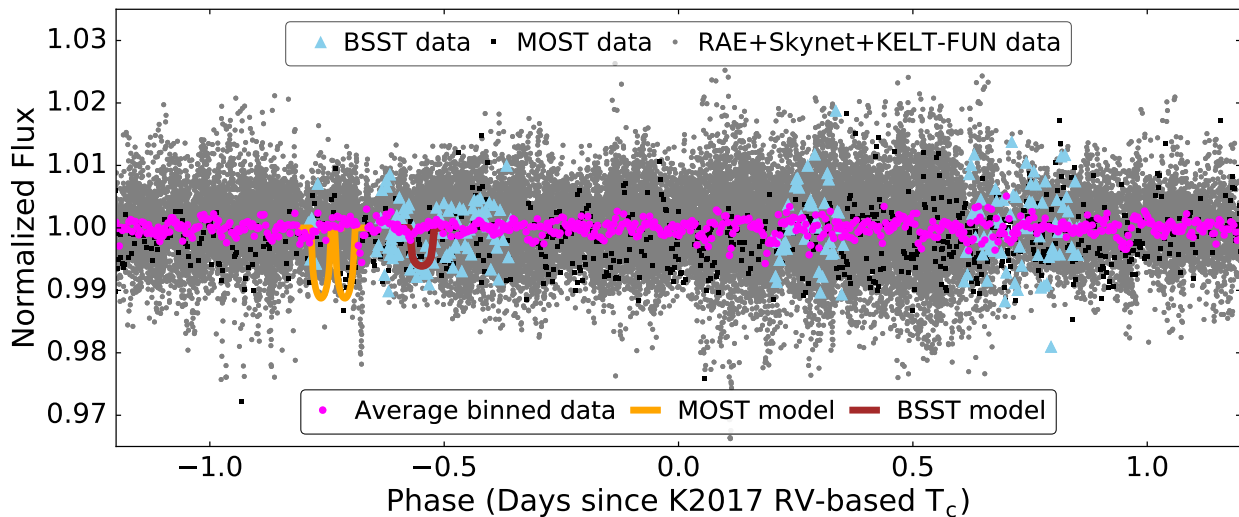
Figure 2.4: All light curve observations, including those from the literature and those newly obtained by us, folded on the K2017 RV-based ephemeris. The data from this work are displayed as grey dots, and after combining and binning at five minute intervals, as magenta dots. The K2017 MOST data are also displayed as black squares, and the L2017 BSST data are shown as light blue triangles. The K2017 Signal C transit models are displayed as orange solid lines. The L2017 BSST transit model is displayed as a brown solid line. There are no obvious periodic transit signals, at the depth of the plotted models, evident within the noise of the binned data.

2.10.2   Light Curves in Relation to K2017 Signals C and S Ephemerides

K2017 reported a transit-like event detection, referred to as Signal C, that is within the 2σ range of their RV-based ephemeris. To check for evidence of periodic transits in our data corresponding to signal C events, our data are phase folded using the corresponding Model $\mathscr{M}_2$ ephemeris and displayed as grey dots in Figure 2.5. The data are combined and binned at five minute intervals (after phased folding) and displayed as magenta dots. The binned data have a standard deviation of $\sim 0.20\%$, well below the 0.84% depth of the $\mathscr{M}_2$ model (displayed as a black solid line), but there is no obvious transit-like event in our phased data. The MOST data are also displayed as black squares, and the BSST data are displayed as light blue triangles. The lack of an obvious transit-like signal in our data, relative to the depth predicted by Model $\mathscr{M}_2$ is strong evidence that Signal C was not caused by a transiting exoplanet in a periodic orbit.
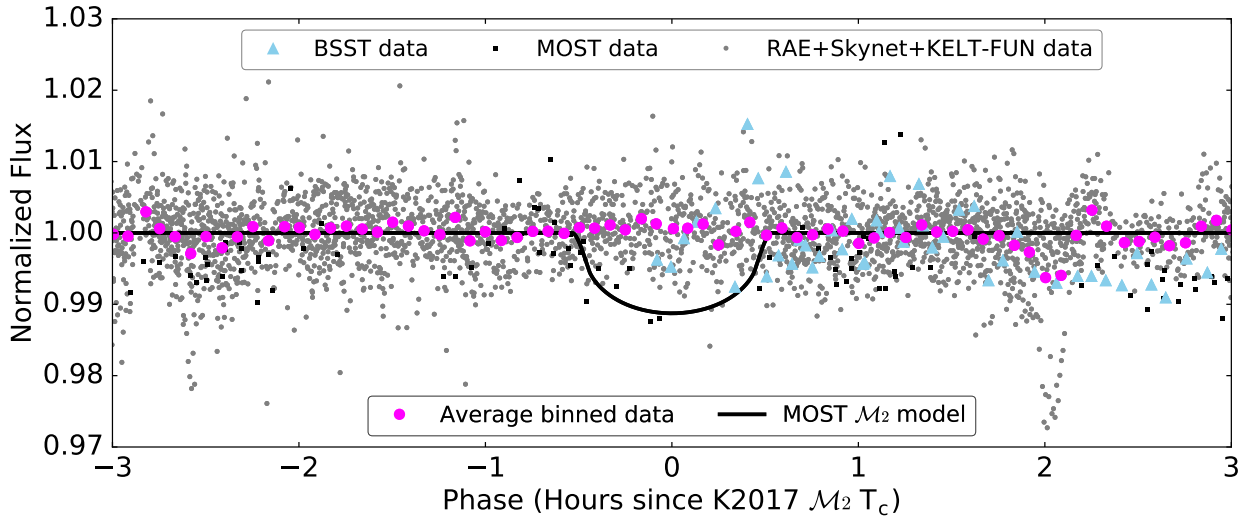
Figure 2.5: All light curve observations, including those from the literature and those newly obtained by us, folded on the K2017 Model $\mathscr{M}_2$ ephemeris. The phase range displayed is ± 3 hours from the Model $\mathscr{M}_2$ transit center time. Light curves from this work are displayed as grey dots, and after combining and binning at five minute intervals, as magenta dots. The MOST data are shown as black squares and the BSST data are displayed as light blue triangles. The K2017 $\mathscr{M}_2$ transit model is displayed as a black solid line.

K2017 also reported a transit-like event detection, referred to as Signal S, that is outside the 2σ range of their RV ephemeris, which they considered spurious. To check for evidence of periodic transits in our data corresponding to signal S events, the data are phase folded using the

corresponding Model $\mathcal{M}_1$ ephemeris and displayed as grey dots in Figure 2.6. The data are combined and binned at five minute intervals (after phased folding) and displayed as magenta dots. The binned data have a standard deviation of $\sim 0.21\%$, well below the 1.06% depth of the $\mathcal{M}_1$ model (displayed as a black solid line), but there is no obvious transit-like event in our data. The normalized MOST data are also displayed as black squares, and have been shifted vertically so that they approximately align with the $\mathcal{M}_1$ light curve model near to and during the time of the event. No BSST data contribute within ± 3 hours of the Model $\mathcal{M}_1$ ephemeris. The lack of an obvious transit-like signal in our data supports the K2017 conclusion that Signal S is spurious.
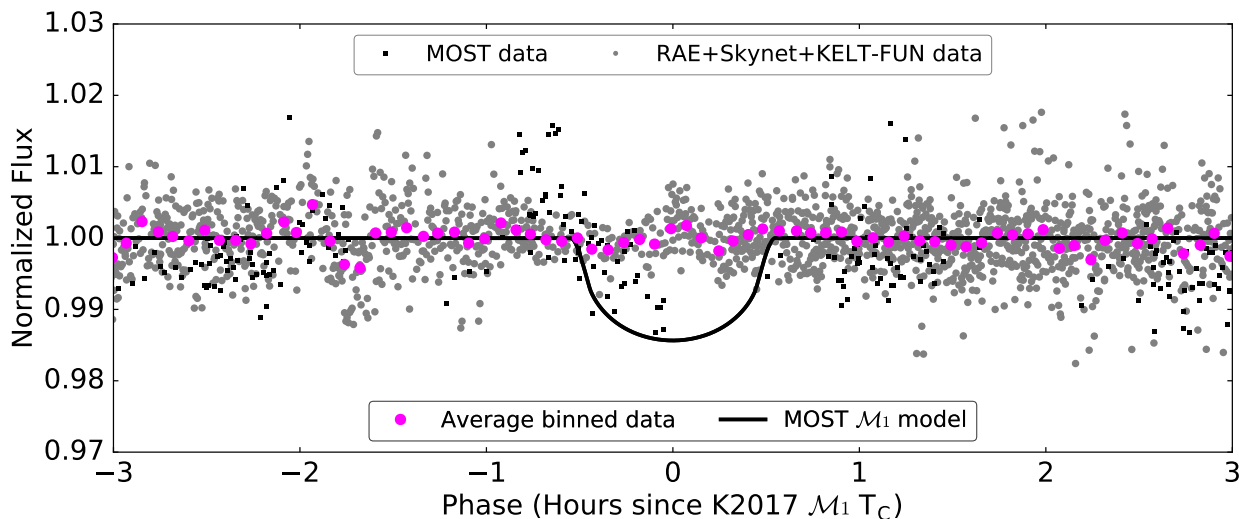
Figure 2.6: All light curve observations, including those from the literature and those newly obtained by us, folded on the K2017 Model $\mathcal{M}_1$ ephemeris. The phase range displayed is ± 3 hours from the Model $\mathcal{M}_1$ transit center time. Light curves from this work are displayed as grey dots, and after combining and binning at five minute intervals, as magenta dots. The MOST data are shown as black squares and the $\mathcal{M}_1$ transit model is displayed as a black solid line. No BSST data contribute to the displayed phase range.

2.10.3 Light Curves in Relation to L2017 TTV Ephemeris

L2017 combined a single transit-like event detection in their BSST data with the two K2017 Signal C events and found the best fit linear ephemeris, which has a slightly longer period than the Signal C ephemeris. We present the observations from this work and the MOST and BSST observations phased to the L2017 ephemeris in Figure 2.7. The data are displayed as described

in Section 2.10.2 and Figure 2.5, except that the L2017 transit model is displayed as a black solid line. Our binned data have a scatter of $\sim 0.20\%$, which is below the 0.5% depth of the claimed transit. We see no evidence of a periodic 0.5% deep transit signal in our binned data. In fact, there is an apparent slight brightening in our light curve during the predicted transit event, which we discuss further below.
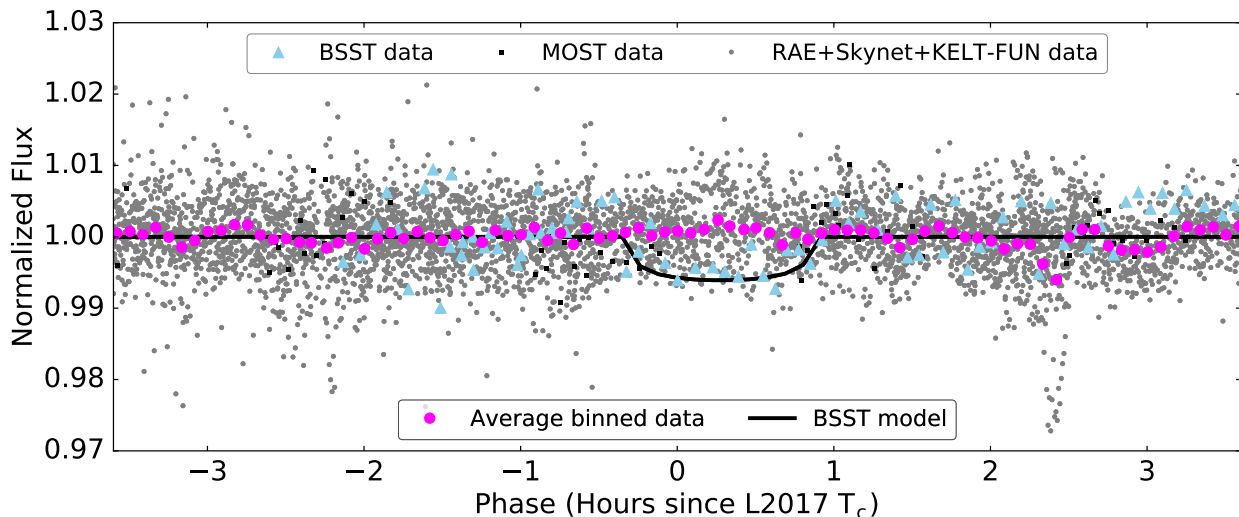
Figure 2.7: All light curve observations, including those from the literature and those newly obtained by us, folded on the L2017 ephemeris. The phase range displayed is ± 3 hours from the L2017 transit center time. The data are displayed as described for Figure 2.5, except that the L2017 transit model is displayed as a black solid line.

The three transit-like events connected by the L2017 ephemeris are not consistent with a strictly periodic signal, but can be described by a common ephemeris if TTVs on the order of $\sim 20 - 40$ minutes are allowed. A series of transit events with TTVs on the order of half of the transit duration will "smear out" the events in a phased plot making them harder to detect. Therefore, to search for transit-like signals in our data that are consistent with the L2017 ephemeris plus TTVs, the phase-folded constituent light curves in Figure 2.7 are shifted relative to each other on the vertical axis in Figure 2.8. Each light curve has been binned at 5 minute intervals. The data from this work are displayed as dark and light grey dots for alternate light curves for clarity (since some light curves occasionally overlap in time). The MOST data are displayed in black and the BSST data are displayed in light blue. The transit models, phased to the L2017 linear ephemeris and shifted

according to the TTV offsets listed in L2017 Table 2, are displayed as black and light blue solid lines for the K2017 $\mathcal{M}_2$ and L2017 models, respectively.

We first note that the "20060605 RAE" light curve shows a flux deficit with a time of event minimum that occurs $\sim$ 1 hour before the L2017 ephemeris predicted transit center time, and with flux deficit duration of $\sim$ 1.5 hours. However, the light curve shows a flux increase above the average value during the time of transit, which explains the slight increase in brightness during transit in Figure 2.7. Considering the higher points in the light curve to be the out-of-transit baseline, the flux deficit event is even deeper and longer in duration. Given the inconsistency of the flux deficit event with the L2017 transit model, and the additional variations in those light curves, we do not interpret it as being caused by a transiting exoplanet, and further, do not support the connection of the tentative L2017 event with the tentative MOST Signal C events though the TTV-based ephemeris.

The other light curves are relatively flat or contain variations that are not consistent with a transit event. Although the constituent light curves do not provide full phase coverage at each epoch, it seems unlikely that our data would have missed all transit events on the 15 epochs with partial light curve phase coverage. Our light curve on "20140523 SS03" was observed simultaneously with the "20140523 MOST" light curve. Unfortunately, the robotic telescope halted observations during part of the first of the two MOST Signal C events. In addition, the correct relative baseline of the data between -1 and 0 hours is unknown because of a large jump of the field on the detector at about -1 hours, and a median flip at about -0.5 hours. Therefore, despite our simultaneous observations, we cannot place strong constraints on the Signal C event. The two deeper events at -2.2 and +2.3 hours in the "20140523 SS03" light curve are analyzed in more detail in Section 2.11. Since we are unable to predict the TTVs for our observed epochs, and since the SS03 robot shutdown during most of the Signal C event on UT 2014 May 23, our data are unable to completely rule out the

L2017 reported TTV-based ephemeris.
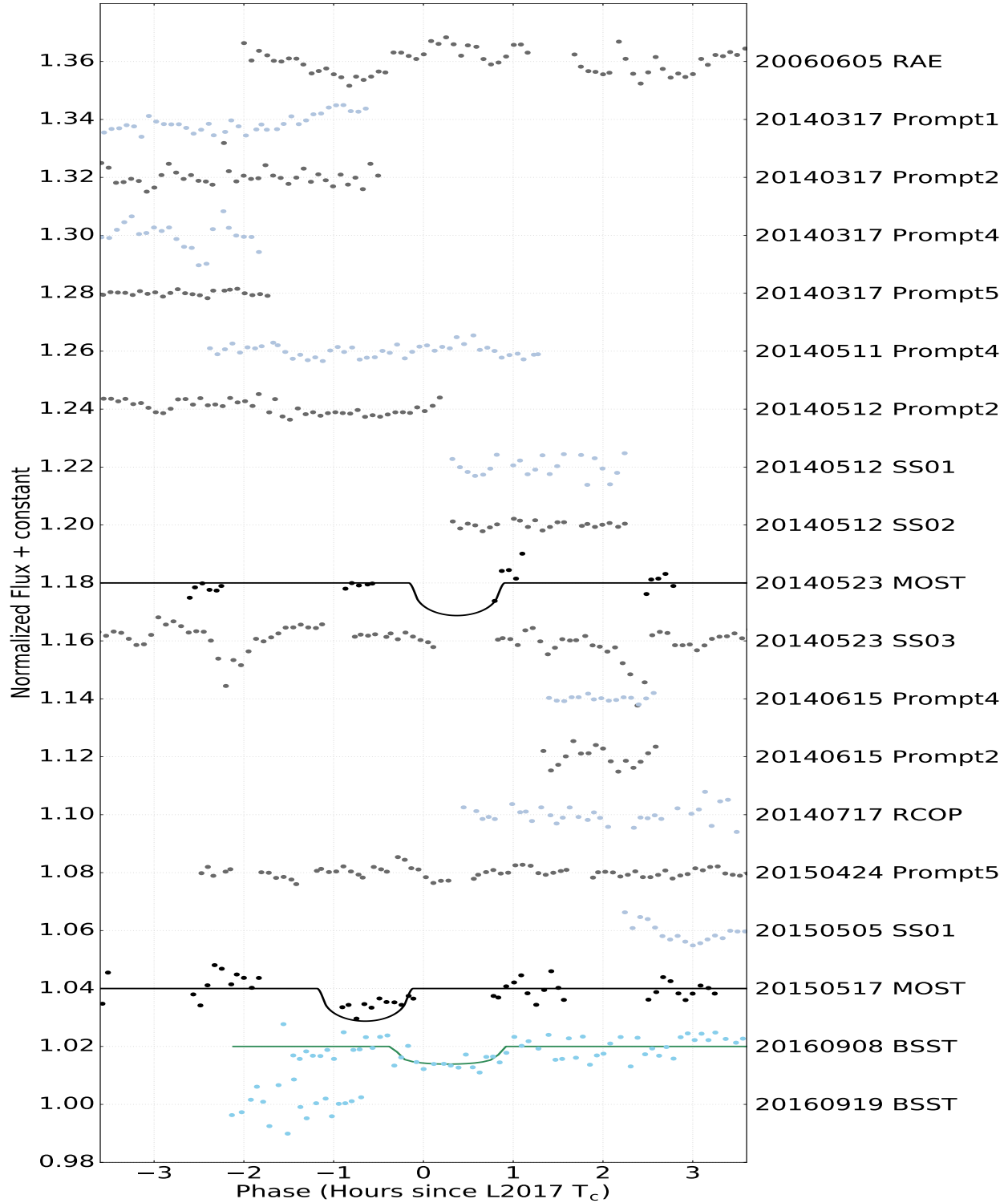
Figure 2.8: All light curve observations, including those from the literature and those newly obtained by us, folded on the L2017 ephemeris. The phase-folded constituent light curves in Figure 2.7 are shifted relative to each other on the vertical axis. Each light curve is binned at 5 minute intervals. The data from this work are displayed as dark and light grey dots for alternate light curves for clarity. The MOST data are displayed in black and the BSST data are displayed in light blue. The L2017 transit model is displayed as the light blue solid line for the BSST event while K2017 $\mathscr{M}_2$ transit models are displayed as the black solid lines for the MOST events.

2.10.4 Light Curves in Relation to Li2017 Ephemeris

Finally, we sought to phase-fold our light curve data according to the ephemeris proposed by Li2017. Unfortunately, due to the single transit-like event found by those authors, a precise period is not available for a phased transit search. The final observation from our campaign was obtained prior to the Li2017 reported event, so we have no simultaneous light curve to compare with theirs. However, Li2017 generously included full AIJ photometry measurements tables for all of their time-series observations on a public archive. With a measurements table loaded into AIJ, we were able to examine how the choice of different comparison star ensembles affected the Proxima light curve.

We generally find that choosing comparison stars having brightness as close as possible to the target star reduces systematics in the data due to variable atmospheric conditions. In the Li2017 data, Proxima had an average of $\sim 1.5 \times 10^6$ net integrated counts in the aperture. Based on our re-analysis, it appears that Li2017 used comparison stars having $\sim 0.2 \times 10^6$ net integrated counts in the aperture, except for one that is about 50% as bright as Proxima. There are three additional comparison stars that are more than 75% as bright as Proxima, so we explored a re-reduction of the Li2017 photometry using a comparison ensemble which included only the four stars that are at least 50% as bright as Proxima.

The original Li2017 light curve exhibiting the claimed transit is displayed in Figure 2.9 as red dots and has been shifted on the vertical axis for clarity. The corresponding original transit model is displayed as the top black solid line. The undetrended result of using the bright star ensemble is displayed as blue dots. Notice a slight airmass trend downward on the right hand side and a significantly shorter event in the data. The simultaneously fitted and airmass-detrended light curve is displayed as magenta dots. The corresponding best fit model is represented by the middle black solid line. Finally, the same bright star result simultaneously fitted to a flat line and airmass-detrended is displayed as green dots. There is indeed a short residual event when fitting to

a flat line. This could indicate that the short transit-like signal is a *bona fide* astrophysical event. On the other hand, since even the brightest comparison stars are still $\sim 25\%$ fainter than Proxima, the short signal could be a residual systematic, albeit much shorter than the signal resulting from the faint star ensemble. With the currently available data, we are unable to conclude which of the results best represents the true behavior of the Li2017 Proxima light curve on UT 2016 August 25.

Li2017 also provided on the public archive AIJ photometric tables for 22 additional Proxima time-series observations. We re-investigated those 22 light curves and found seven light curves that show apparent events having various durations and depths, any of which could be a Proxima astrophysical event or a systematic (we did not investigate alternate comparison star ensembles for these observations). It is unlikely that seven out of 22 blind search observations would catch transit events, which suggests that the variations were caused by an alternate astrophysical mechanism, or were caused by systemics, or a combination of both. These non-periodic variations exhibit a range of behaviors similar to the behaviors observed in our data (see Figure 2.3 and Appendix A).
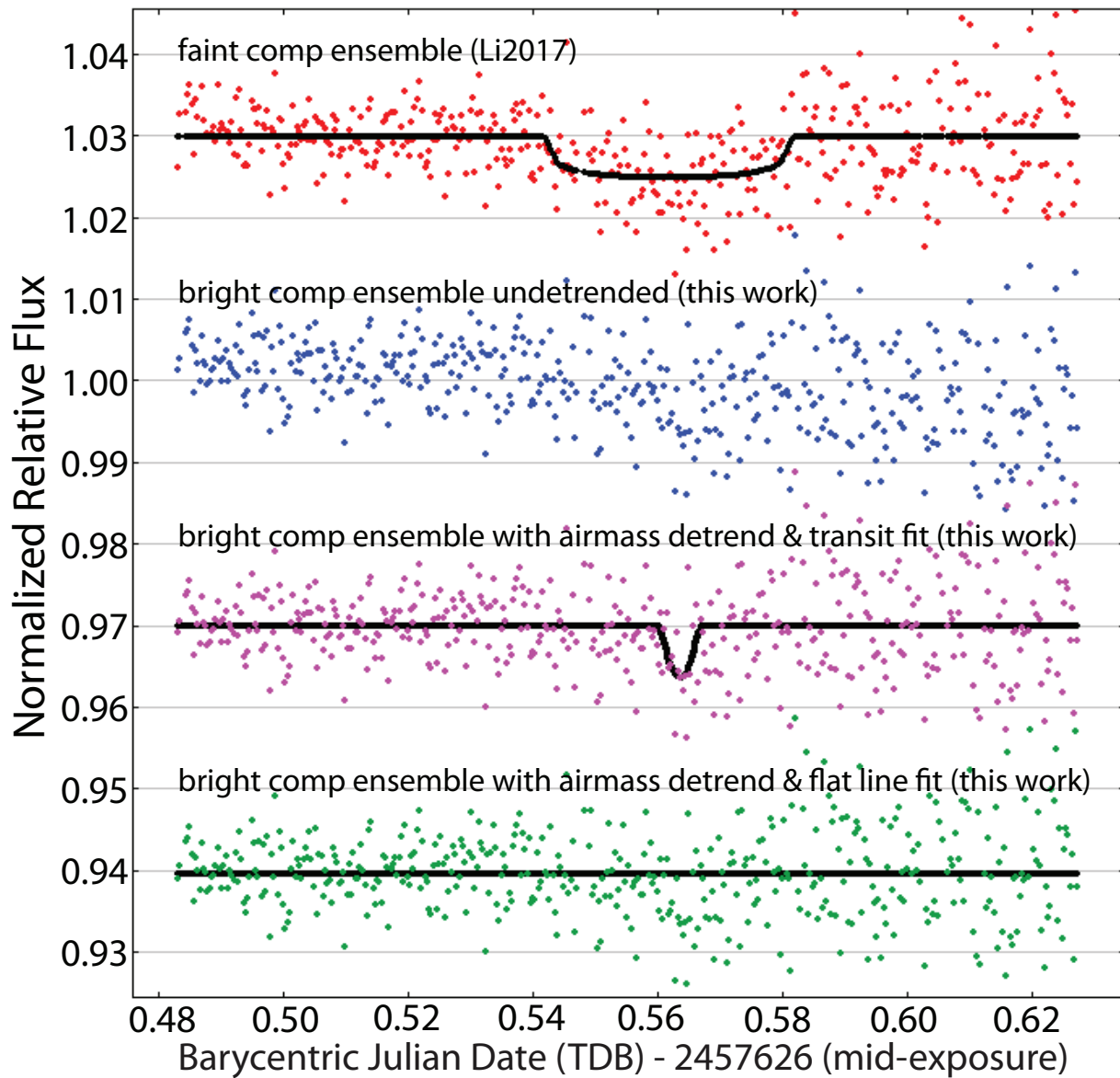
Figure 2.9: Comparison of the Li2017 results with our alternate reduction. The original Li2017 light curve exhibiting the claimed transit is displayed at the top as red dots. The undetrended result using the bright star ensemble (see text) is shown as blue dots in the second light curve from the top. The simultaneously fitted and airmass-detrended bright ensemble light curve is shown as magenta dots in the third light curve from the top. The bright ensemble light curve simultaneously fitted to a flat line and airmass-detrended is shown as green dots at the bottom. Models are displayed as black solid lines. Light curves are successively shifted by 0.03 to minimize data overlap for clarity. The signal in the bright ensemble light curve is significantly shorter than the faint star ensemble used by Li2017.

2.11   Discussion

We find no compelling evidence for Proxima b transits corresponding to any of the previously published ephemerides. We do, however, find many examples of light curves having variations consistent with the predicted $0.5 - 1.3\%$ Proxima b transit depths. Davenport et al. 2016 predicted that low energy flares of this magnitude occur approximately every 20 minutes on Proxima. These semi-regular events, having an amplitude similar to the predicted Proxima b transit depth (assuming Proxima b transits do exist), and occurring on the time scale of the predicted Proxima b transit duration, could contribute to the variations seen in our data. These positive-flux events would bias the individual light curve normalization levels upward by varying amounts, depending on the amount of low energy flare activity within the time-period covered by a particular light curve. Positive flux events occurring during a *bona fide* transit would tend to obscure the transit by changing the apparent duration, shifting the apparent transit center time, and/or dividing the transit into two or more shorter events, significantly complicating the detection of a potential real Proxima b transit. Furthermore, it is possible that starspots forming or changing significantly on $\sim$ hour timescales could produce photometric dips similar to the transit-like events and other variations detected in this work and by other authors.

As mentioned in Section 2.2, K2017 found only tentative evidence for Proxima b transit events, and they too discuss the difficulties of detecting Proxima b transits, if in fact they do occur, given the predicted low energy flare contributions to the Proxima light curve data. Because of the pervasiveness of variations in our data, we conclude that the low energy flares and starspot transients, combined with light curve systematics, are the source of many or all of the variations in our data. However, the variations could be hiding *bona fide* transit events. We reiterate that since we do not know the appropriate underlying astrophysical model that describes Proxima's light curve behavior, our light curve data presented here have been individually detrended assuming a flat light curve model. We have visually compared each undetrended light curve with its detrended version to verify that our detrending method did not significantly reduce or enhance transit-like events in

44

our data.

To further investigate systematics and other variations in ground-based Proxima light curves, we also re-analyzed the data set that included the Li2017 2.5σ transit-like signal detection and find that the signal becomes less obvious when comparison stars closer in brightness to Proxima are used. In addition, we reviewed 22 additional light curves provided by Li2017 and found seven that show variations, any of which could be Proxima astrophysical events or systematics. It appears that the Li2017 observations exhibit a range of behaviors similar to the behaviors observed by us. As visual evidence of the routine variability that may mimic transit-like events, we present a collection of our Proxima light curve data within $\pm 2\sigma$ of the K2017 RV-based ephemeris in Figure 2.10. We point out events with arrows that could be interpreted as transit-like features. In some cases, the events occur very near the time corresponding to one of the previously claimed transit ephemerides. However, such events also occur with similar frequency at other times.
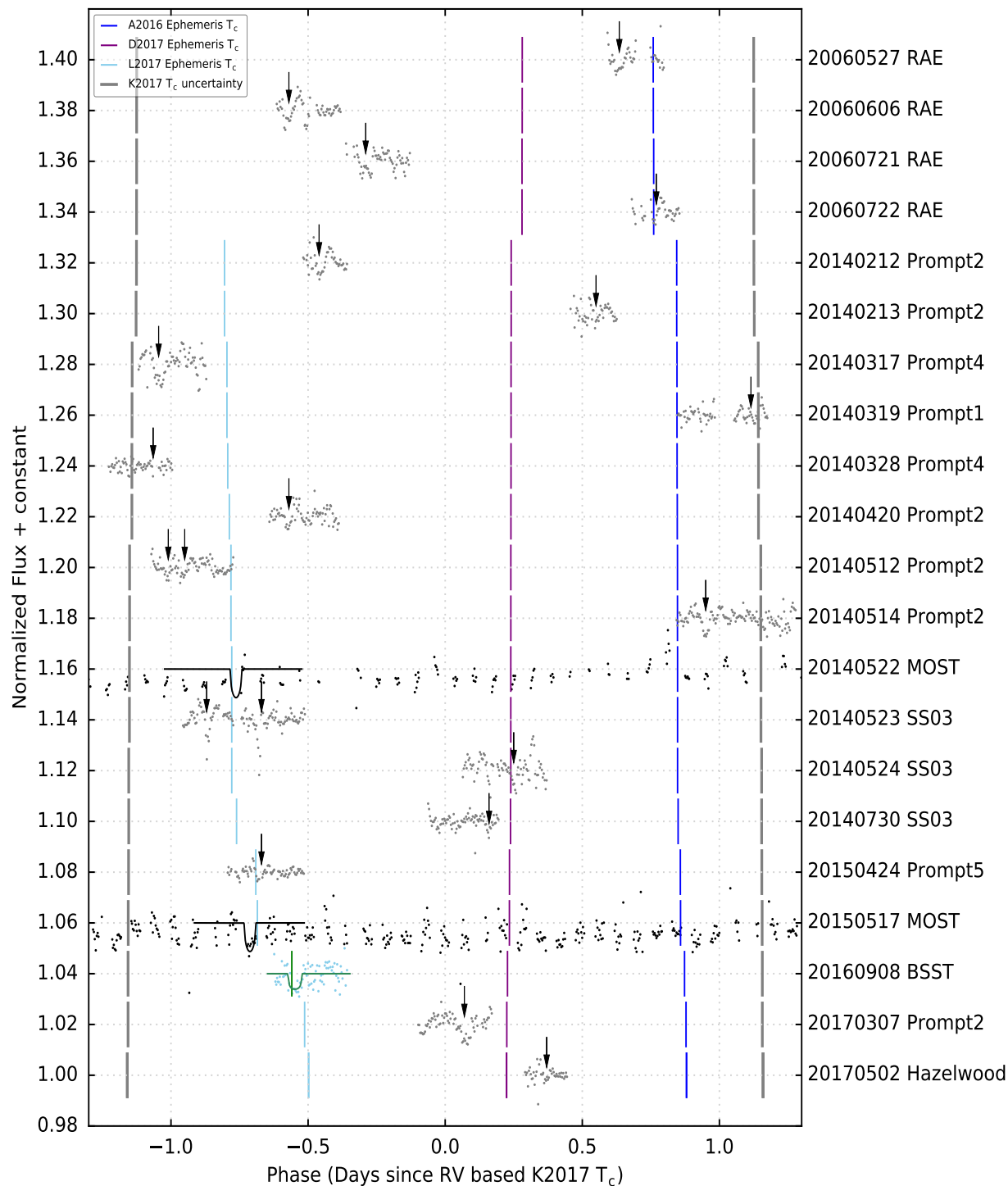
Figure 2.10: A subset of 18 light curves from this work that display variations with an amplitude similar to the depth predicted for a transiting Proxima b planet. All light curves are binned in 5 minute intervals and phased to the K2017 RV-based ephemeris. Light curves from this work are displayed as grey dots. The MOST and BSST data are plotted as black and light blue dots, respectively, along with the K2017 $\mathcal{M}_2$ (Signal C) and L2017 transit models in black and green solid lines, respectively. The black arrows are placed to highlight events that exhibit variations similar to the claimed transit detection depths reported in Table 2.1. The transit center times corresponding to the ephemerides of A2016, D2017, and L2017 are plotted as vertical blue, magenta, and light blue bars, respectively. The gray vertical bars mark the $\pm 2\sigma$ uncertainty boundaries for K2017 RV-based ephemeris.

46

In Figure 2.11, we present a more detailed investigation of four of the transit-like signals identified in Figure 2.10. The unbinned, detrended data are shown as black dots, and the best fit Mandel & Agol 2002a transit models are shown as a solid red lines. The "20140514 Prompt 2" light curve is presented in the top panel of Figure 2.11. The best fit model has a duration of 56 minutes and a depth of $0.55 \pm 0.1\%$, which is somewhat consistent with many of the tentative detections from the literature. However, the transit center time is not consistent with the other photometric-based ephemerides from the literature, and there are no other obvious events in our data that would indicate that the fitted event is periodic at the RV-based period. Those inconsistencies combined with the somewhat asymmetric morphology and the post-egress saw-tooth-shaped variations suggest that the $\sim 5\sigma$ detection is unlikely to have been caused by a transiting exoplanet.

We also found three transit-like features that are deeper than predicted for Proxima b. Two of the events occur in the "20140523 Prompt SS03" light curve shown in the middle panel of Figure 2.11. The event centered at 2456800.956 BJD$_{\rm TDB}$ has a best fit transit model depth of 1.31% and a duration of ~ 25 minutes. However, the model fit does not find the correct pre- and post-transit baseline, and doesn't fully account for the very short, initially deeper, ingress feature. Accounting for both of those features, we estimate that the true maximum change in the light curve is $\sim 3\%$. The second event in the middle panel, centered at 2456801.145 BJD$_{\rm TDB}$, has a best fit transit model with a depth of 2.5% and a duration of 11 minutes. Both events in this light curve have significantly asymmetric ingresses and egresses. Our "20140524 Prompt SS03" light curve has the deepest transit-like event found in our data and is displayed in the bottom panel of Figure 2.11. The event is centered at 2456801.933 BJD$_{\rm TDB}$ and the best fit transit model has a depth of 3.3% and a duration of 12 minutes.

We have investigated all of our systematics indicators and find no parameters that are correlated with these transit-like signals. However, due to the robotic nature of the Prompt telescopes, and the limited set of systematics indicators available to us, we cannot exclude systematics as the source

of these light curve features. In fact, Figure 2.8 illustrates that the MOST observations provide partial coverage of the event centered at 2456800.956 BJD$_{\text{TDB}}$ and do not show evidence of an event at that time (~ -2.3 hours in Figure 2.8). If these events are in fact astrophysical in nature, it is unlikely that they were caused by a transit of Proxima b due to asymmetric feature morphology, events that are too deep and short, and/or the fact that three similar features occurred within one day around 2456801 BJD$_{\text{TDB}}$, but are not found elsewhere in our data.
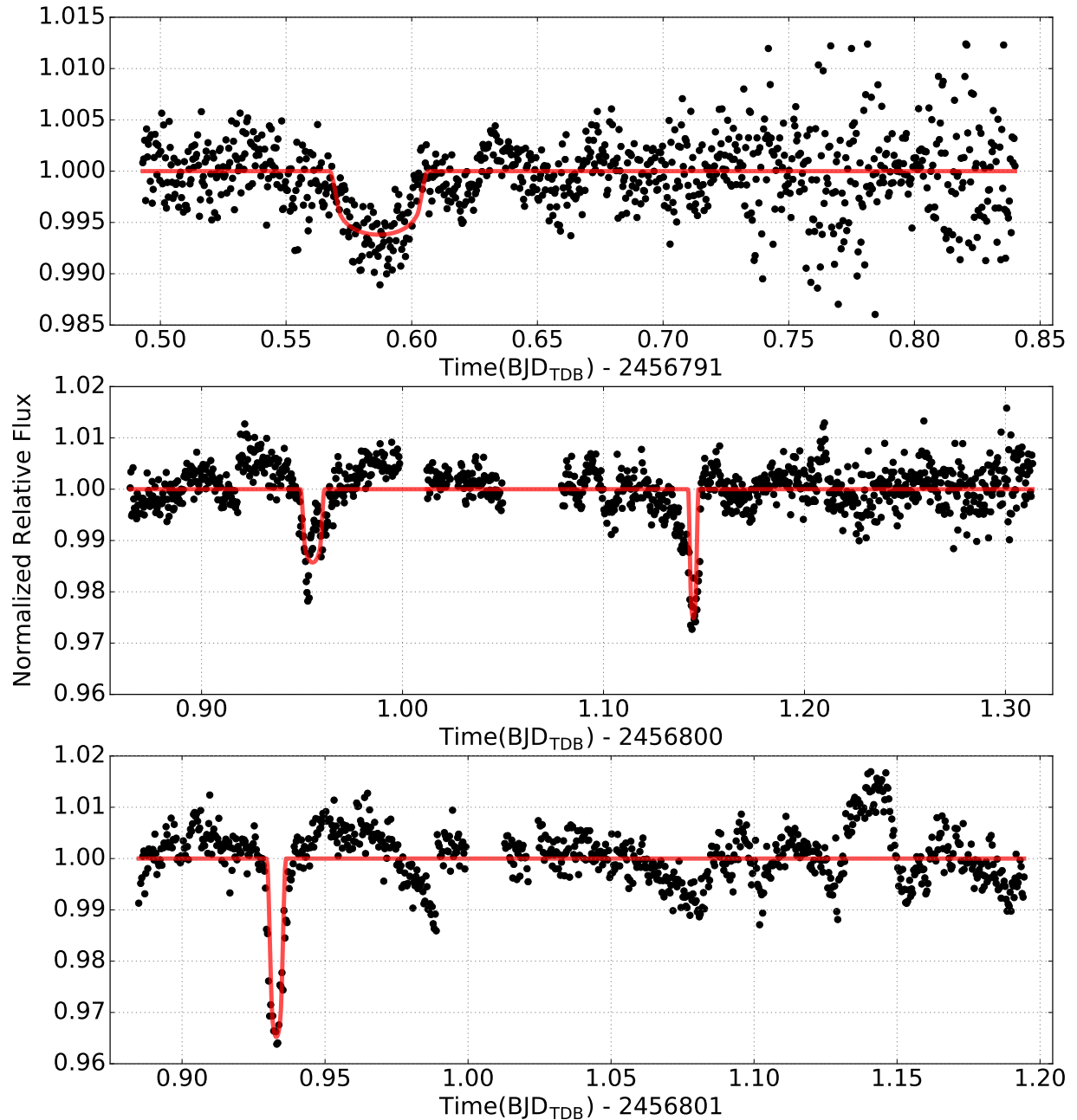
Figure 2.11: Examples of transit-like events in our Proxima data. The unbinned, detrended data are displayed as black dots, and the best fit transit models are displayed as red solid lines. (Top) Prompt 2 *R* band light curve from UT 2014 May 14. The model has a duration of 56 minutes and a depth of $0.55 \pm 0.1\%$. The somewhat asymmetric morphology and the post-egress sawtooth-shaped variations suggest that this light curve feature may not have been caused by a transiting exoplanet. (Middle) Prompt SS03 *R* band light curve from UT 2014 May 23. (Bottom) Prompt SS03 *R* band light curve from UT 2014 May 24. It is unlikely that the short, deep, mostly asymmetric events in the middle and bottom panels were caused by transits of Proxima b. See text for more details.

2.12 Conclusion

From a total of 262 Proxima light curves that will be published in Paper II of this series, we presented 96 Proxima time-series photometric observations that correspond to previously published Proxima b ephemerides from the literature. The light curves span from 2006 to 2017 and were conducted using a combination of RAE, Skynet and KELT-FUN telescopes. Because almost all of our observations were conducted before the A2016 RV-discovered planet was announced, we were generally conducting a blind search for transits of Proxima. Although Proxima's flares are prominent across the UV and optical bands, they are indeed stronger in the blue compared to the underlying stellar photosphere (Walker, 1981), so we targeted the R passband and redder to minimize the impact on our photometric observations. Even so, contamination from systematics, starspot transients, flares, and/or low energy flares that are predicted to occur about every ~ 20 minutes at the 0.5% level (Davenport et al., 2016), is significant in our photometric data. We simultaneously cleaned, detrended, and normalized each night of differential photometry individually using a 3σ iterative cut and a flat light curve model in lieu of a correct, but unknown model. We have visually compared each pre-cleaned, undetrended light curve with its cleaned and detrended version to verify that the data processing methods we used did not significantly reduce or enhance transit-like events in our data.

We investigated our data in relation to the RV-based ephemerides presented in A2016, K2017, and D2017, and the photometric-based ephemerides presented in K2017, L2017, and Li2017. In general, we find pervasive variability in our cleaned and detrended light curve data at the level of $0.5 - 3.0\%$. We also explored a re-analysis of the Li2017 data using a different ensemble of comparison stars that were similar in brightness to Proxima and found a significant reduction in the duration of the claimed event (the event was essentially eliminated). We also find variability in seven of 22 additional Li2017 light curves, similar to what we find in our data. Overall, considering all of the available data that coincide specifically with the previously published claimed transit detections, we are unable to independently verify those claims. We do, however, verify the

previously reported ubiquitous and complex variability of the host star.

In Paper II, we will present a search for periodic Proxima b transits over the range of periods having good phase coverage from our full set of 262 light curves. We will also present an analysis of the transit detection sensitivity of our data across a range of transit model parameters.

As previously mentioned, flares are stronger in blue bands than red bands, but are still significant in red bands. The Transiting Exoplanet Survey Satellite (TESS, Ricker et al. 2015) will likely observe Proxima for at least 27 days. TESS observes in a single band that includes the optical wavelengths above $\sim 600\,\mathrm{nm}$ ($\sim R$ band and redder), which will help minimize the contamination from Proxima's flares. However, it may still be difficult to separate contamination from the combination of possible starspot transients and the predicted every $\sim$20-min low energy flares from a potential *bona fide* transit signal in the TESS data, especially if the Proxima b orbit is not strictly periodic due to significant perturbations from other companion(s) in the system. One potential approach to separate the predicted low energy flares from potential real transit signals would be to conduct simultaneous observations in a blue and red band, since the low energy flares should be more significant in the blue band, while the transit signal should be consistent in both. Alternatively, observations simultaneous with the TESS observations, but in a different filter band could help differentiate transit signals in the TESS data.

Chapter 3

A Multi-year Search for Transits of Proxima Centauri II: No Evidence for Transit Events with Periods between 1 and 30 days

This chapter originally published as Feliz et al. 2019 in *The Astrophysical Journal*.

Abstract

Using a global network of small telescopes, we have obtained light curves of Proxima Centauri at 329 observation epochs from 2006 – 2017. The planet Proxima b discovered by Anglada-Escudé et al. 2016 with an orbital period of 11.186 d has an *a priori* transit probability of $\sim 1.5\%$; if it transits, the predicted transit depth is about 5 millimagnitudes. In Blank et al. 2018 (Chapter 2), we analyzed 96 of our light curves that overlapped with predicted transit ephemerides from previously published tentative transit detections, and found no evidence in our data that would corroborate claims of transits with a period of 11.186 d. Here we broaden our analysis, using 262 high-quality light curves from our data set to search for any periodic transit-like events over a range of periods from 1 – 30 d. We also inject a series of simulated planet transits and find that our data are sufficiently sensitive to have detected transits of 5 millimagnitude depth, with recoverability ranging from $\sim 100\%$ for an orbital period of 1 d to $\sim 20\%$ for an orbital period of 20 d for the parameter spaces tested. Specifically at the 11.186 d period and 5 millimagnitude transit depth, we rule out transits in our data with high confidence. We are able to rule out virtually all transits

of other planets at periods shorter than 5 d and depths greater than 3 millimagnitudes; however, we cannot confidently rule out transits at the period of Proxima b due to incomplete orbital phase coverage and a lack of sensitivity to transits shallower than 4 millimagnitudes.

3.1   Introduction

The discovery of Proxima Centauri b (Proxima b, hereafter) via the radial velocity (RV) technique by Anglada-Escudé et al. 2016 was a landmark event in exoplanet studies. We now know that orbiting in the habitable zone (Kopparapu et al., 2013) of the star nearest to our Sun is a planet that is likely to be rocky (Brugger et al., 2016; Kane et al., 2017; Bixel & Apai, 2017) and possibly habitable (Ribas et al., 2016; Barnes et al., 2016; Meadows et al., 2016; Turbet et al., 2016; Boutle et al., 2017). We report here further results from our transit search of Proxima Centauri from 2006 to 2017 (Blank et al., 2018, Paper I hereafter) which was motivated by the possibility that such planets may exist, and that they could be found using sub-meter size telescopes with commercial grade CCD cameras.

In the 11 years of this photometric campaign, we collected light curves at 329 epochs. Of these 329 light curves, 262 passed various quality tests (detailed in Paper I), 96 of which overlapped with the previously published ephemerides[8] of Anglada-Escudé et al. 2016, Kipping et al. 2017, Liu et al. 2017 and Li et al. 2017. A search for transits corresponding to Proxima b at these ephemerides is reported in Paper I. No convincing transit event attributable to Proxima b was detected in this subset of light curves.

In this work, we proceed to search all 262 quality light curves systematically for a planet of any orbital period in the period range 1.01 to 30.5 days. In Section 3.2 we summarize the data collection, drawing reference to Paper I. We also describe our strategy for determining a period range

---

[8] Throughout this paper we use the word ephemeris to refer to predicted, known, or estimated reference transit center time T_c plus an orbital period P for a known or possible transiting exoplanet. These values can be derived precisely from transit observations, or with less precision from RV observations.

to conduct our planet search. In Section 3.3 we describe our methods of analysis for searching for periodic transit events and tests for statistical significance and sensitivity to detect transit events. Section 3.4 contains our results and the tests of sensitivity needed to place limits on any possible detection. We discuss our findings in Section 3.5.

3.2   Observations and Data Completeness

3.2.1   Summary of Observations and Data Reduction done in Blank et al. 2018

The observations that make up our data set of 329 light curves came from the world-wide robotic telescope network Skynet (Reichart et al., 2005), the Real Astronomy Experience (RAE) robotic telescope (Fadavi et al., 2006) located in in Bickley, Western Australia, and from several participating observatories from the Kilodegree Extremely Little Telescope (KELT; Pepper et al. 2007, 2012) Follow-Up Network (KELT-FUN; Collins et al. 2018). More details about the participating instruments are in Table 2 in Paper I. Our data reduction techniques are described in Section 3.2 of Paper I.

To briefly summarize, in order to minimize the effects of long term stellar variability and differential chromatic airmass we performed a linear detrend for each parameter so that the final mean flux value was 1.0. Additionally, for correlated changes in the photometric baseline due to telescope meridian flips, we fitted and realigned the baseline at that point. In some light curves we performed an additional set of linear detrends using the x- and/or y-centroid locations of the target star, sky background, full-width half-maximum of the stellar point spread function, and/or the total number of comparison star net integrated counts. For more information on detrending with AstroImage J, see Section 4.4 of Collins et al. 2017. To remove obvious flares that are predicted to occur ~ 63 times per day (Davenport et al., 2016) and photometric outliers, we performed an iter-

ative 3-σ clipping. We present our 3-σ clipped undetrended and detrended light curves in Tables A1 and A2 in Appendix B.

3.2.2 Geometric Transit Probability of Proxima b-Like Planets For A Given Period

To estimate the geometric transit probability of Proxima, we assumed a planet mass of 1.27 $M_{\oplus}$ and a planet radius of $\sqrt{\delta}R_*$, where $\delta \sim 5$ millimagnitudes (or mmag, hereafter) as reported by Anglada-Escudé et al. 2016 and then calculated the probability of a planet transiting as the fraction of the area of the celestial sphere that is swept out by the shadow of the planet during one orbital period (Borucki & Summers, 1984; Winn, 2011):

$$\text{Transit Probability} = \left(\frac{R_* + R_p}{a}\right)\left(\frac{1 + e\sin w}{1 - e^2}\right) \tag{3.1}$$

Where R_* is the stellar radius, R_p is the planet radius, a is the semi-major axis, e is the eccentricity and w is the argument of periastron. Applying Kepler's Third Law, assuming e=0, w=$\pi/2$ and that $R_p \ll R_*$ gives:

$$\frac{R_*}{a} = R_*\left(\frac{G(M_p + M_*)P^2}{4\pi^2}\right)^{-1/3} \tag{3.2}$$

Adopting a stellar mass $M_* = 0.1221\, M_{\odot}$ and stellar radius $R_* = 0.1542\, R_{\odot}$ (Kervella et al., 2017), the geometric probability of transit detection for orbital periods from 0.01 to 365 days is shown in the top panel of Figure 3.1. It should be noted that this geometric estimation is based on the planet density model assumed by Anglada-Escudé et al. 2016 ($M_p = 1.27\, M_{\oplus}, \rho/\rho_{\oplus} = 1$) and that all transits are assumed to be across the face of the host star. Scaled curves of this type will have varied results from different assumptions of the density of the planet and from grazing transits.

3.2.3 Phase Coverage of Photometric Observations

To estimate the phase coverage of our data, we phase folded our data for each day in the period range of $0.01 - 365$ days and then binned our data into 5 minute bins and calculated the inverse variance weighted means for each bin.

$$\hat{y} = \frac{\sum_i y_i/\sigma_i^2}{\sum_i 1/\sigma_i^2} \tag{3.3}$$

We then define phase coverage as the number of finite values in our phase folded data bins divided by the total number of values in our phase folded data bins. The result of this procedure is shown in the bottom panel of Figure 3.1 where it is clear that the phase coverage falls below $\sim 75\%$ for periods longer than 30 days. Both panels of Figure 1 show the increasing difficulty of detection of a transit event for longer periods. For period longer than 30 days, both the low sensitivity of detection and the poor phase coverage imply a low probability of detecting a transit, and we have decided to limit our search to the period region 1.01 to 30.5 days. A lower orbital period limit of 1.01 days was chosen to avoid potential aliases due to diurnal and sidereal day sampling.
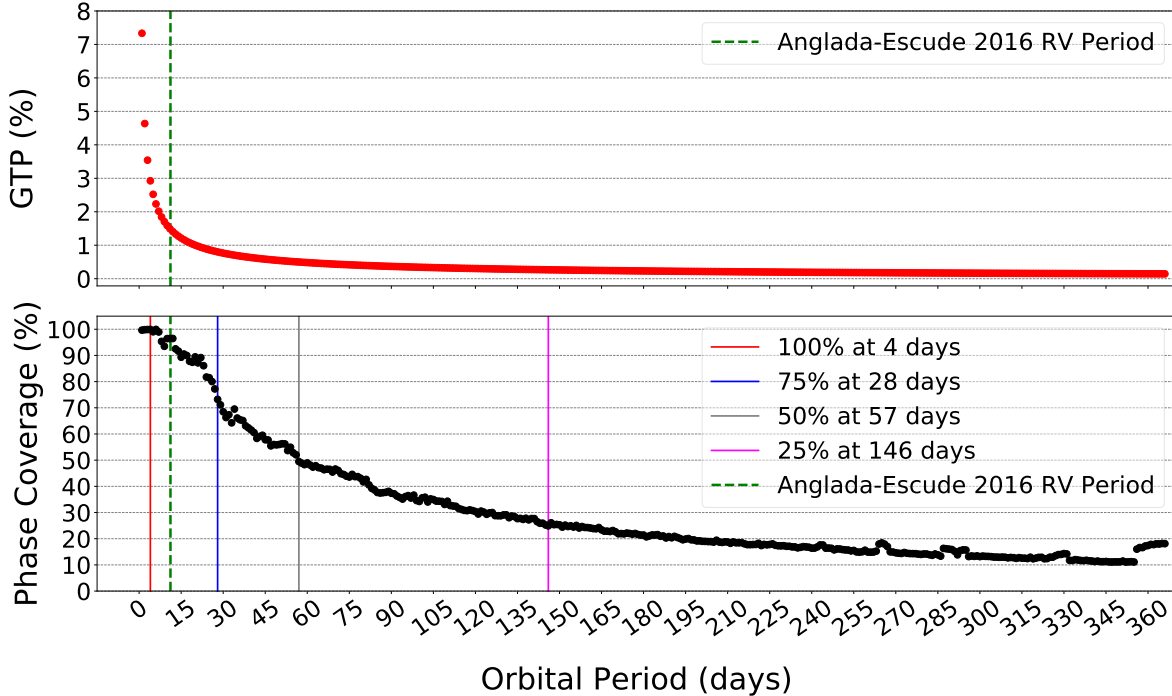
Figure 3.1: Top: The Geometric Transit Probability (GTP) of Proxima Centauri. At the orbital period of 11.186 days determined by the radial velocity discovery of Anglada-Escudé et al. 2016 the transit probability is $\sim 1.5\%$ based on their assumed planet density model. Bottom: Phase Coverage of the 329 individual light curves phase folded and binned into 5 minute bins, as described in Section 3.2.3. The colored solid lines mark the periods where phase coverage is 100%, 75%, 50% and 25%. The phase coverage of our data drops below $\sim 75\%$ around 30 days.

3.3 Methodology

3.3.1 Box-fitting Least-Squares Algorithm

The box-fitting least-squares (BLS) algorithm (Kovács et al., 2002) searches for periodic decreases in star brightness of a photometric time series. The BLS algorithm models transit events as simple step functions and identifies transiting planet candidates by phase folding light curves to trial frequencies and searching a grid of transit epochs and durations at each frequency, and then picking the parameters that maximize the transit depth significance with a least-squares optimization. We use the VARTOOLS software (Hartman & Bakos, 2016) to produce the BLS power spectrum shown in Figure 3.2. To determine the fractional transit length (transit duration divided by orbital period) q, we estimated a minimum value $q_{min} = 0.017$ to account for transit of at least

Table 3.1: Parameters used in BLS periodic searches

q_{min}	q_{max}	P_{max} (days)	P_{max} (days)	N_{freq}	N_{bin}	df (1/seconds)
0.017	0.1	1.01	30.5	920,492	120	1.05×10^{-6}

25 minutes duration for a minimum orbital period of 1.01 days, and q_{max} = 0.1 for events of $\sim$ 3 days for a maximum orbital period of 30.5 days. With q_{min}, a range of desired frequencies ($f_{max} = 1/P_{min}$, $f_{min} = 1/P_{max}$), and the total cumulative baseline of our full data set (T) , we can roughly estimate the number of frequencies required for our BLS search:

$$N_{freq} = (f_{max} - f_{min})/df \tag{3.4}$$

where the stepsize[9], df is defined as:

$$df = q_{min}/4T \tag{3.5}$$

To estimate the number of phase bins[2] (N_{bin}) to break up our cumulative light curve into, we used $2/q_{min} \sim 120$ bins. All parameters used in the BLS search are listed in Table 3.1.

3.3.2   False Alarm Probability

To determine the statistical significance of peaks in the BLS power spectrum, we define a false alarm probability (FAP) to be the probability of a peak having equal strength by random chance or due to the cadence of our sampling. This is done by randomly rearranging the detrended fluxes and error information while keeping the time stamps fixed, reapplying the BLS search and record-ing the BLS outputs for the top peak of each iteration. This random permutation is then repeated 1,000 times. The 0.1% FAP is the highest peak out of 1,000 permutations, the 1% FAP is the 10th

---

[9] https://www.astro.princeton.edu/~jhartman/vartools.html#BLS

highest peak out of 1,000 permutations and the 10% FAP is the 100th highest peak out of 1,000 permutations. In Section 3.4.2, we apply different variations of this definition of FAP.

3.3.3   Transit Injections

To test the sensitivity of the BLS algorithm in recovering transit-like events, we injected fake transits into our detrended data and ran the BLS algorithm on the injected data sets. We simulated these fake transits using a given transit depth δ, and orbital periods P, along with the stellar mass, stellar radius, the orbital eccentricity e, orbital inclination i and the argument of periastron w (all transit model parameters are listed in Table 3.2). With each permutation of our transit model parameters, we simulated a total of 550 Mandel-Agol transit models (Mandel & Agol, 2002a) using the Python package PyTransit, (Parviainen, 2015), which in addition to the parameters listed in Table 3.2, also uses quadratic limb darkening coefficients, u. To obtain values for u, we used the EXOFAST[10](Eastman et al., 2013) website to interpolate quadratic limb darkening coefficients from the limb darkening tables in Claret & Bloemen 2011. As seen in Table 2 of Paper I, the majority of our light curves were observed with an R filter and we were able to obtain u $\sim$[0.425, 0.298] for Proxima in the R band using the EXOFAST website, providing T_{Eff} = 3042 K, log g = 5.20, [Fe/H] = 0.21 (Ségransan et al., 2003) and as inputs. After model creation, we then use BLS to test our ability to successfully detect our injected transit events, as described in Section 3.4.6.

3.4   Results

3.4.1   BLS Power Spectrum

Using the parameters from Table 3.1, we applied the VARTOOLS (Hartman & Bakos, 2016) BLS algorithm on our combined and detrended 262 observations from the Skynet, KELT-FUN and

---

[10] http://astroutils.astronomy.ohio-state.edu/exofast/limbdark.shtml

Table 3.2: Parameters used in Transit injection Analysis

Parameter	Value / Model	Citation
Stellar Radius, R_{star}	0.1542 $R_\odot$	Kervella et al. 2017
Stellar Mass, M_{star}	0.122 $M_\odot$	Kervella et al. 2017
Effective Temperature, T_{Eff}	3042 K	Ségransan et al. 2003
log g	5.20	Ségransan et al. 2003
[Fe/H]	0.21	Schlaufman & Laughlin 2010
Transit Depth, δ (mmag)	1.0, 2.0, 3.0, 4.0, 5.0, 6.0, 7.5, 10.0, 15.0, 20.0	This work
Orbital Period, P (days)	1.1, 2.1, 3.1, 5.1, 7.6, 10.1, 11.186, 15.1, 20.1, 25.1, 30.1	This work
Orbital Phase	-0.4, 0.2, 0.0, 0.2, 0.4	This work
Eccentricity, e	0.0	This work
Inclination, i	$\pi/2$	This work
Argument of Periastron, w	$\pi/2$	This work
Quadratic Limb Darkening Coefficients	(0.425,0.298) for R band	Interpolated from Claret & Bloemen 2011 tables.

NOTE: The quadratic limb darkening coefficients are estimated using the EXOFAST website[10] to interpolate the quadratic limb darkening tables from Claret & Bloemen 2011 by providing log g, [Fe/H] and T_{Eff} as inputs.

RAE telescopes. In our application of BLS, we used the "nobinnedrms" option in VARTOOLS which calculates the Signal Residue, *SR(f)*, as defined in Kovács et al. 2002, with the average value of *SR(f)* subtracted, and divided by the standard deviation of *SR(f)*. This leads to points in the power spectrum that have *SR(f)* below the average value and will have a negative Spectroscopic Signal to Noise (*S/N(f)*, described in Section 3.4.3). We ran our BLS search from 1.01 to 30.5 days and found that all peaks in the power spectrum within orbital periods of 1.01 – 30.5 days fall below the majority of the calculated FAP and FAP(P) thresholds, as described in Section 3.4.2. The top peak of the BLS power spectrum corresponds to an orbital period of $\sim$ 1.808 days, which lies above the 10% FAP(P) threshold. As an example of the transit-like events detected by BLS in our data, Figure 3.3 displays the phase folded light curve of our data, using the orbital period and transit center time reported by the BLS algorithm. Figure A3 in Appendix B, shows the 32 individual light curves that contribute to this signal. Although there is some evidence for a transit-like event in Figure 3.3, the existence of such an event is not supported by analysis of the individual light curves.

We note that there is no significant power in the BLS power spectrum at the orbital period determined by the radial velocity of Proxima b (Anglada-Escudé et al., 2016) which is consistent with our failure to find transits in Paper I. In section 3.4.5, we describe a methodology to detect low power peaks like those near the 11.186 day RV period that are displayed in the inset panel of
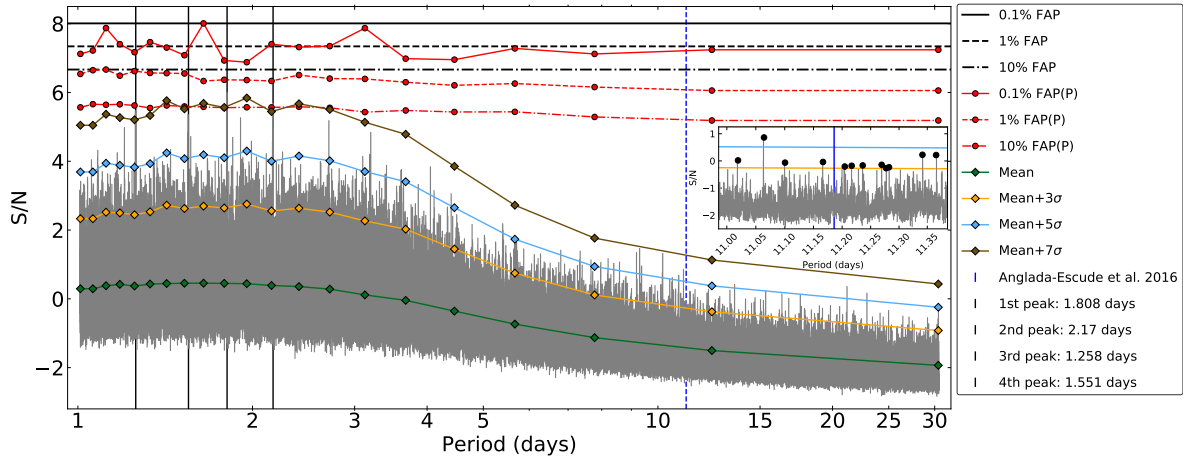
Figure 3.2.

Figure 3.2: We present a power spectrum from the VARTOOLS BLS transit search algorithm. The black vertical solid lines represent the orbital periods corresponding to the top 4 peaks of the power spectrum. The horizontal black lines correspond to the 0.1%, 1%, and 10% FAP as described in Section 3.3.2. The red lines are the FAP(P) thresholds calculated in 20 period ranges with equal N_{freq} as described in Section 3.4.4. The green, orange, cyan and brown lines represent the robust estimations for the mean and mean plus the 3σ, 5σ and 7σ of the S/N in each period range as described in Section 3.4.5. The inset figure is a close up of peaks in the power spectrum that are near the 11.186 day RV period and are also above the mean + 3σ and mean + 5σ lines, marked with black dots.
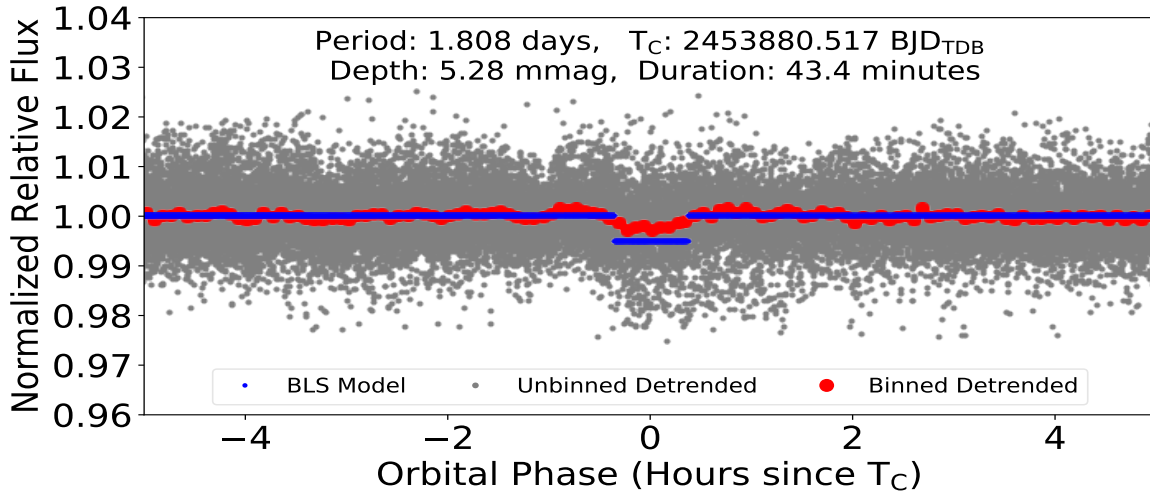
Figure 3.3: From the power spectrum in Figure 3.2, we took the orbital period corresponding to the top peak and phase folded our combined 262 light curves. The grey dots are the unbinned detrended data and the red dots are binned detrended data with 5 minute bin widths. The BLS model of this peak, shown as the blue line, has a transit depth and duration of ~ 5.28 mmag and 43.4 minutes. We do not believe this to be a real transit event as shown in Figure A3 and explained in Appendix B.

3.4.2 Testing Statistical Significance of BLS Power Spectra

3.4.3 FAP

In order for each power spectrum of the randomly permuted data sets to be on comparable scales, we normalized the power spectra using a modified version of the Spectroscopic Signal to Noise used in Hartman & Bakos 2016:

$$S/N(f) = \frac{SR(f)_{random} - \overline{SR}(f)}{\sigma_{\overline{SR}}} \qquad (3.6)$$

where we use the average and standard deviations of the BLS reported *SR(f)* of the power spectrum in Figure 3.2 with the *SR(f)* of the randomized data sets. Based on our definition of FAP in Section 3.3.2, we find FAP thresholds for the 0.1% FAP occurs at a S/N of ~ 7.61, 1% FAP at ~ 6.96 and the 10% FAP at ~ 6.35 as shown as horizontal black lines in Figure 3.2.

3.4.4 FAP As A Function of Period

To better assess the validity of peaks below the 0.1%, 1% and 10% FAP values, we divided N_{freq} into 20 period ranges, starting from 1.01 days and used Equations 3.4 and 3.5 to calculate the bounds of each subsequent period range so that each range contained the same number of frequencies.

$$P[i] = \frac{P[i-1]}{1 - P[i-1] \times (q_{min}/4T) \times (N_{freq}/20)} \forall\, i \in \{1, ..., 20\} \qquad (3.7)$$

These period ranges are displayed in Figure 3.4. For each period range, we then follow a similar process as our FAP procedure, where we randomly shuffle our data with fixed time stamps and then run a BLS search on the shuffled data. Within each period range, we then record information from the highest peak in the resulting BLS power spectra and repeat the process a total of 1,000
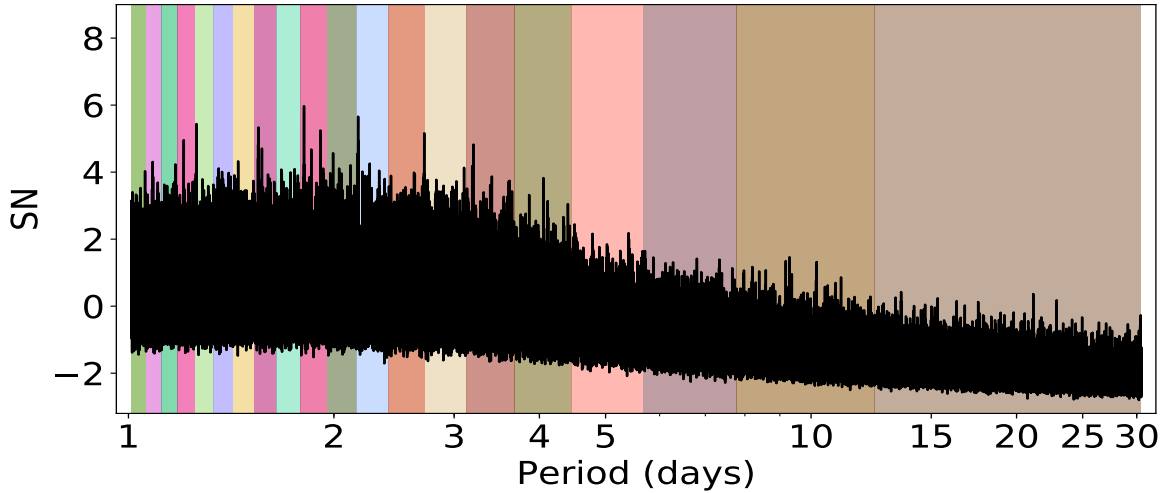
Figure 3.4: An illustration of the 20 period ranges used to define FAP(P). The edges of the ranges are calculated with Equation 3.7. Each colored shaded region is a different period range where each range has an even amount of frequencies, $N_{freq}/20$.

times. From these 1,000 permutations, we calculate the FAP thresholds within each period range. We then interpolated FAP values between edges of each period range which we refer to hereafter as FAP(P), which is shown as the red line-connected dots in Figure 3.2.

3.4.5 Robust Estimation Of The Mean S/N

As a visually intuitive alternative to identifying potentially significant, low power, peaks like those that are near the RV orbital period of 11.186 days, we utilized the Python package StatsMod-els[11] module for Huber's robust estimator of scale and location (Huber, 1981) to estimate the mean and standard deviation of the S/N of the power spectrum. By fixing the orbital period on these 12 low power peaks near the 11.186 day period, we then ran a BLS search to obtain parameters for transit center time, transit duration and transit depth. In Figure 3.5, we use these parameters to phase fold our data around these 12 orbital periods corresponding to peaks near the 11.186 day RV period, in addition to the 11.186 day RV period itself. We then carefully and critically examined curves all light curves that contribute to each of these 13 peaks. We find that on average, these

---

[11] https://www.statsmodels.org/stable/index.html

peaks correspond to transit depths of ~ 0.73 mmag and there are no consistent light curve events that display these periodic decreases in flux.

To apply this method as an additional transit detection criteria in Section 3.4.6, we calculated the robust estimations of mean and standard deviation of the transit injected power spectra S/N within each of the 20 defined period ranges described in Section 3.4.4 and shown in Figure 3.4. Similarly to our procedure in estimating our FAP(P) function in Section 3.4.4, we then interpolated values of the robust statistics between edges of each period range to use in our transit injection recovery described in Section 3.4.6. Using these robust statistics provides a better estimation for the location of the mean and standard deviation of S/N without rejecting outliers.
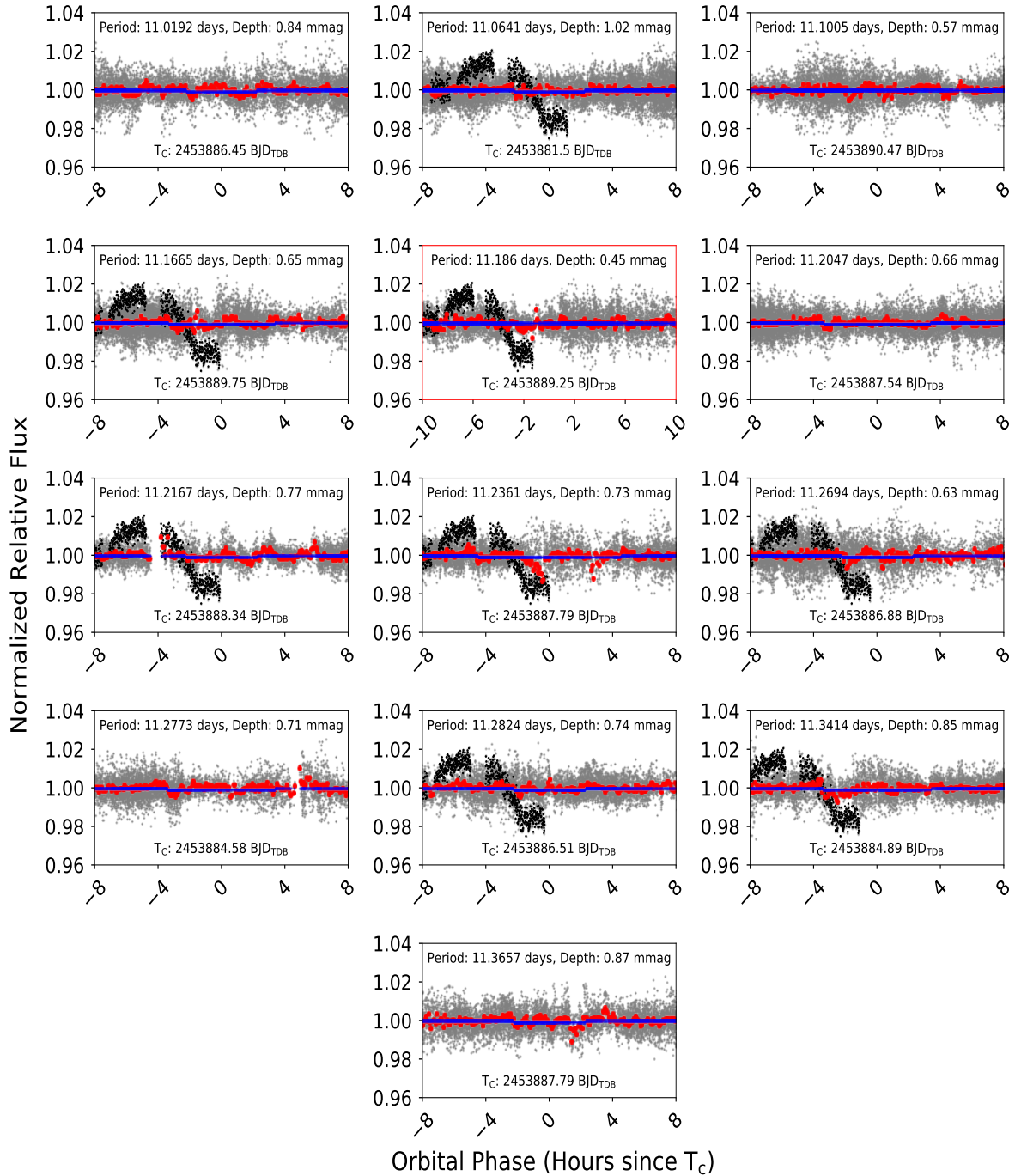
Figure 3.5: From the inset panel of Figure 3.2, we have identified 12 peaks that have S/N values larger than the robust mean + 3σ of the power spectrum's S/N within the corresponding period range. We then conducted a BLS search using a fixed period for each of these 12 peaks, in addition to the 11.186 day RV period, and phase folded our data with the corresponding transit center time output by the VARTOOLS BLS algorithm. In each panel of this figure, we have the phase folded light curves with the unbinned detrended data as grey points, the binned detrended data with 5 minute bins as red points and the BLS model as the blue lines. The black points are the detrended data from the UT April 11 2007 RAE light curve which is also in shown Figures A3 and discussed in Appendix B. In each case, the transit depths reported by BLS are on the order of 1 mmag or smaller which is reflected by the relatively weak peak strength as seen in Figure 3.2.

3.4.6   Transit Injection Recovery

To test the sensitivity of the BLS algorithm's transit detection ability on our data set, we injected 550 transit models into our detrended data as described in Section 3.3.3. We then ran the BLS algorithm using identical input parameters as in Table 3.1 and recorded the resulting power spectra and BLS reported transit parameters. In this analysis, a successfully recovered transit injection is defined as a peak in the power spectrum that is within $\pm 1\%$ of the injected transit model's orbital period and has a BLS Power above a detection threshold. We use the FAP, FAP(P) and robust estimations of the mean plus standard deviation of the S/N as three separate thresholds to gauge our ability to detect varying peak strengths in the transit injected power spectra.

We also considered harmonics and sub-harmonics (1/3, 1/2, 2 and 3 times) of the injected transit model periods in our detection criteria. We apply our detection criteria to the 550 transit injections and perform BLS searches to recover the injected transits across multiple orbital phases. As an example, Figure 3.6 displays 1 of our 550 transit injections that was successfully recovered. The results of using these three different thresholds along with our detection criteria can be seen in Figures 3.7, 3.8 and 3.9. The numbers of the color bars shown in Figures 3.7, 3.8 and 3.9 represent the number of orbital phases where a detection by BLS occurred, ranging from 0 (for no detections in any of the phases tested) to 5 (detections in all phases tested) for the FAP, FAP(P) and robust mean plus standard deviation thresholds, respectively.

As expected, the number of successfully recovered transit injections decrease for orbital periods beyond 15 days where our phase coverage decreases to about 90% as shown in Figure 3.1. For the injected transits with Proxima b's orbital period of 11.186 days and a transit depth of 5 mmag (highlighted by red and cyan colored boxes in Figures 3.7, 3.8 and 3.9) and higher, we successfully recover transit injections in at least 2 of the 5 orbital phases with and without the requirement of FAP or FAP(P), and recover 5 out of the 5 orbital phases with the robust mean plus standard devi-
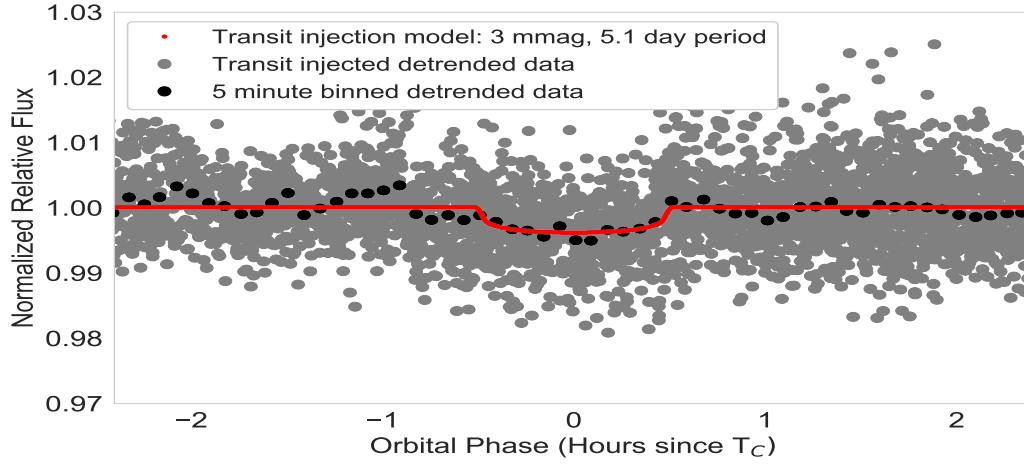
Figure 3.6: With the Pytransit (Parviainen, 2015) python pacakge, we were able to inject 550 Mandel-Agol (Mandel & Agol, 2002a) planet models into our detrended data. The model is displayed as a red line for one such simulated transiting planet with an orbital period of 5.1 days, a transit depth of 3 mmag and phase folded to the midpoint of our data set at 2455922.515188 BJD$_{\text{TDB}}$ with an orbital phase of 0. The grey points are our transit injected detrended data. The black points are our transit injected detrended data binned with 5 minute bins.

ation thresholds.

3.4.7 Constraints on Transiting Planet Properties

As a simple exercise, we also estimated which combinations of transit depth and orbital period could be detected by the Doppler semi-amplitude of Proxima b (~ 1.4 m/s) as reported by Anglada-Escudé et al. 2016. For a given planet radius ($R_p = \sqrt{\delta}R_*$), we can define the planet mass as:

$$M_p = \left(\frac{\rho_p}{\rho_\oplus}\right)\left(\frac{R_p}{R_\oplus}\right)^3 M_\oplus \tag{3.8}$$

We assume the planet density to be Earth-like ($\rho_p/\rho_\oplus = 1$). By keeping the Doppler semi-amplitude (K) fixed,

$$K = \frac{2\pi\, a\sin i}{P} \tag{3.9}$$

applying Kepler's Third Law, and assuming a circular orbit (e=0), we can solve for the orbital period:

$$P = 2\pi G \left(\frac{M_p \sin(i)}{K} \right)^3 \left(\frac{1}{M_*} \right)^2 \qquad (3.10)$$

The RV model roughly follows our transit detection recoverability up to an orbital period ~ 25 days and transit depths as low as ~ 6 mmag. We display this model over our transit injection recovery plots as red and cyan colored lines in Figures 3.7, 3.8 and 3.9. Each orbital period and transit depth cell in Figures 3.7, 3.8 and 3.9 that are above the line correspond to the transit depth and orbital period combinations that should be detectable in the RV data.

If Proxima b does transit and is not denser than Earth, then the planet would appear in a cell above the RV model; however our light curve data rule out any transit above the curve for orbital periods shorter than ~ 15 days. For other rocky planets (with Earth-like density) that might exist in the system, they must be below the RV model in Figures 3.7, 3.8 and 3.9 or else their RV signatures would presumably have been detectable. While our light curve data does not generally probe the regions under the RV model, we are able to rule out detectable transit events for orbital periods $\lesssim 5$ days and transit depths $\gtrsim 3$ mmag.
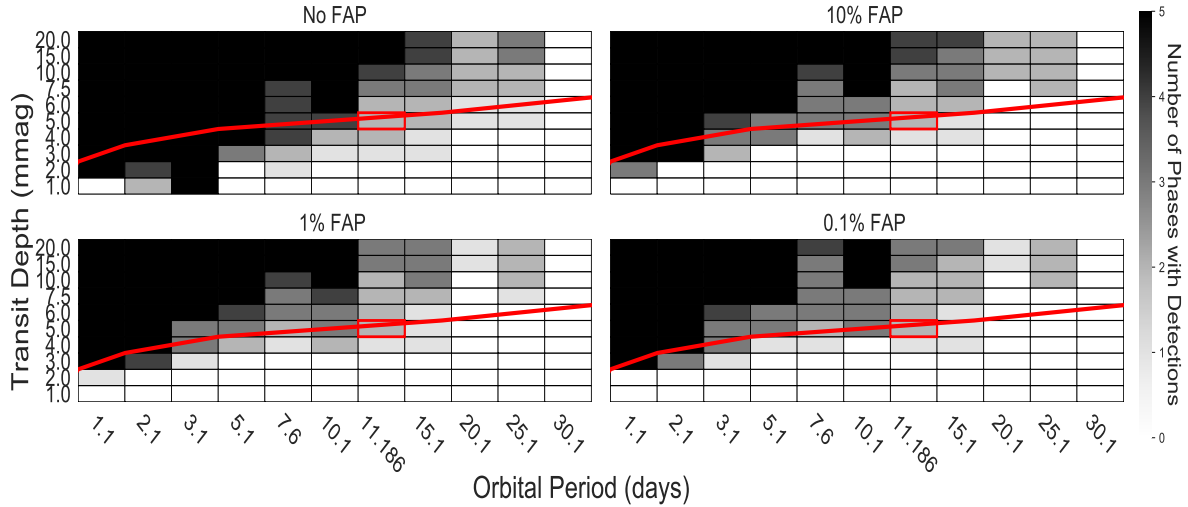
Figure 3.7: Applying the detection criteria described in Section 3.4.6 to our 550 transit injected data sets, we present a color map of transit detections that occurred in the orbital phases: -0.4, -0.2, 0, 0.2, 0.4. The upper left figure represents recovered transit injections within $\pm 1\%$ of their injected periods but considering no FAP threshold. The upper right figure represents recovered transit injections within $\pm 1\%$ of their injected periods and over the 10% FAP thresholds. Similarly the lower left and right figures represent recovered transit injections within $\pm 1\%$ of their injected periods and above the 1%, 0.1% FAP thresholds, respectively. The red line is our radial velocity model for an Earth-like exoplanet with constant Doppler semi-amplitude of 1.4 m/s, described in Section 3.4.7.
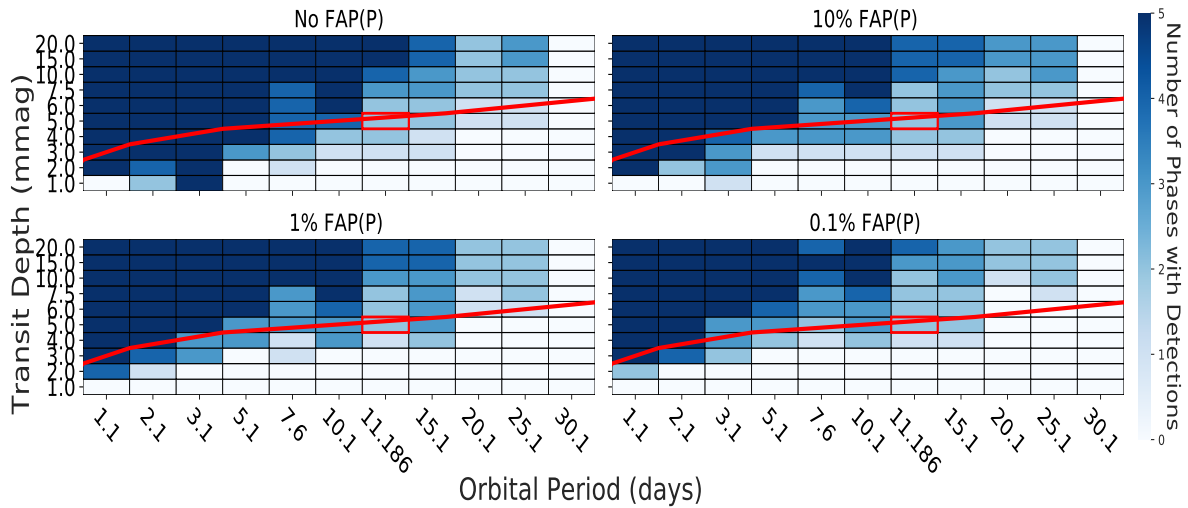

Figure 3.8: Similarly to Figure 3.7, we altered our detection criteria to use the FAP(P) function described in Section 3.4.4. The upper left figure represents recovered transit injections within $\pm 1\%$ of their injected periods but considering no FAP(P) threshold. The upper right figure represents recovered transit injections within $\pm 1\%$ of their injected period and over the 10% FAP(P) thresholds. Similarly the lower left and right figures represent recovered transit injections within $\pm 1\%$ of their injected period and above the 1%, 0.1% FAP(P) thresholds, respectively. The red line is our radial velocity model for an Earth-like exoplanet with constant Doppler semi-amplitude of 1.4 m/s, described in Section 3.4.7.
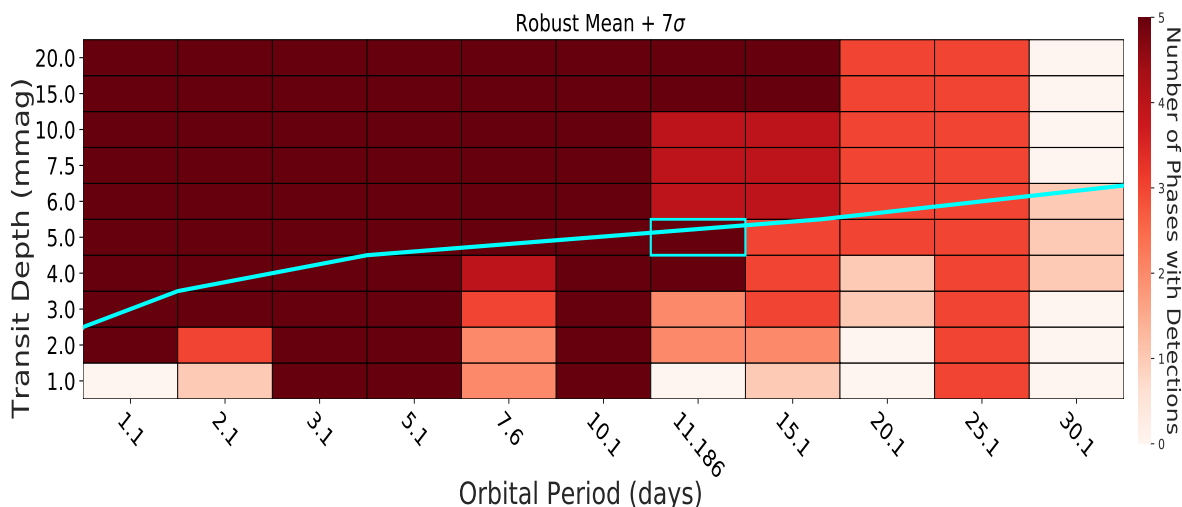
Figure 3.9: Similarly to Figure 3.7, we altered our detection criteria to use the robust estimation of mean, σ of the BLS power spectrum as described in Section 3.4.5. The recovered transit injections that are within $\pm 1\%$ of their injected periods and are over the robust mean $+ 7\sigma$ of the injected power spectra. An example of the robust mean of a power spectrum can be seen as the green line in Figure 3.2. The cyan line is our radial velocity model for an Earth-like exoplanet with constant Doppler semi-amplitude of 1.4 m/s, described in Section 3.4.7.

3.5   Discussion

Although we find no evidence for transits of Proxima b in the BLS analysis of our data, we cannot confidently rule out transits at the period of Proxima b due to incomplete orbital phase coverage and a lack of sensitivity to transits shallower than 4 mmag. However, we are able to virtually rule out any other unknown planet transits of Proxima with orbital periods shorter than 5 days and depths greater than 3 mmag. Furthermore, within our phase coverage and depth sensitivity limitations (see Section 3.4), we find no evidence for transits in our data for orbital periods in the range of 1 to 30 days.

In Paper I, we describe the selection criteria based on the amount of scatter in individual light curves that led to 262 of our 329 light curves to be included in our overall analysis. As shown in Figure 1 of Blank et al. 2018, the median standard deviation of individual unbinned light curves after the detrended and vetting processes is $\sim 0.52\%$ which is similar to the expected 0.5% transit depth for Proxima b. For the minimum mass of 1.27 $M_\oplus$ estimated by Anglada-Escudé et al. 2016,

smaller radii of Proxima b would translate to higher planet densities.

Brugger et al. 2016 determine the ranges of planet mass and radius of Proxima b to be (1.1 -1.46) $M_\oplus$ and (0.94 - 1.40) $R_\oplus$. In the case of the 1.1 $M_\oplus$, 0.94 $R_\oplus$ model of Proxima b, 65% of the planets mass is located in the core and the remaining 35% as part of the mantle. In the 1.46 $M_\oplus$, 1.4 $R_\oplus$ case, the corresponding composition is 50% of the planets mass being in the form of water and the remaining 50% in the mantle. We estimate a planet radius and mass of ~ 0.94 $R_\oplus$ and ~ 1.1 $M_\oplus$ corresponds to a transit depth of about 3 mmag and a planet density 1.32 $\rho_\oplus$ while a planet of radius 1.4 $R_\oplus$ and mass 1.46 $M_\oplus$ corresponds to a transit depth of about 7 mmag and a planet density of ~ 0.5 $\rho_\oplus$.

To determine our lower limit for detectable planet densities, we have extended our exercise Section 3.4.7 to also fix the planet mass to 1.27 $M_\oplus$ in addition to the fixed Doppler semi-amplitude of 1.4 m/s. Using Equation 3.10 gives an orbital period $\sim$13.09 days. The lowest recovered injected transit depth near that orbital period in Figures 3.7 and 3.8 is $\sim$ 3 mmag which corresponds to a planet radius $\sim$0.92 $R_\oplus$. This results in a planet density of $\sim$1.63 $\rho_\oplus$ which is below the minimum density of $\sim$2.07 $\rho_\oplus$ estimated from the lower bounds of the probabilistically constrained result from Bixel & Apai 2017 for their rocky planet model.

Loyd et al. 2018 discusses the mechanisms of flares potentially inducing photoionization heating of the upper atmosphere of planets orbiting very near their host stars. Through the authors' work, they determined that the extreme ultraviolet radiation during flare events can be intense enough to drive hydrodynamic escape. Howard et al. 2018 detected a super flare where Proxima's optical flux increased by 68 times in an hour long event. Through the two years of observations with the Evryscope telescope, they observed 23 other large flare events and determined that super flares of this scale occur roughly 5 times per year, and that this level of repeated flaring may be sufficient enough to reduce the ozone of an Earth-like atmosphere by 90% within five years and

complete depletion may occur within several hundred thousand years. In the event of Proxima b's planetary radius being smaller due to a different planet density or decreasing due to flare driven atmospheric loss, our data should have a sensitivity to transit depths up to $\sim 0.5\%$, supported by the 5 minute binned RMS of our data being $\sim 0.26\%$.

There are several areas for improvement within our data reduction pipeline. The main challenge of detrending our ground-based observations was obtaining as flat of a photometric baseline as possible. With the majority of our light curves coming from unguided telescopes, there existed discontinuous jumps in the raw data from meridian flips and telescope re-pointings. Our iterative 3-σ clipping of Proxima's frequent flare events followed by our detrending methodology did not completely flatten the baseline of light curves and may provide some periodic power in the BLS power spectrum. Figure A3 has a few examples of this such as the UT June 17, 2014 Prompt 1 and Prompt 4 light curves. Algorithms like BLS could fit a box model to these discontinuities or post 3σ-cut flare remnants and report an unlikely transit event.

In our transit injection analysis in Section 3.3.3, we injected our simulated planet models into our detrended data. With our current machinery, it is impractical to inject our 550 planet models and then detrend each injected data set individually with AstroImageJ. In our upcoming Paper III (D.L. Feliz et al., in preparation) we will approach our transit injection methodology to incorporate detrending after injection of simulated planet models.

It is likely that our data have residual correlated noise after our detrending process and there are a many ways to approach modeling the noise (e.g. Gaussian Processes). In addition to scatter due to the intrinsic variability of the star, Proxima is also a well known flare star (Shapley, 1951; Walker, 1981). There are numerous flares within our data set that can be quantified (Jayawardene et al., in preparation) and modelled to subtract the events from our light curves to obtain a flatter baseline more suitable for transit detection. Another alternative to estimate the FAP is with

Bayesian statistics rather than our Frequentist approach which assumes pure white noise.

3.6 Conclusion

In this work, we present an analysis of 262 photometric observations of Proxima Centauri where we search for periodic transit-like events. The light curves have been cleaned and detrended as described in Paper I, and then fed into the box-fitting least squares (BLS) period finding algorithm. To estimate the statistical significance of the peaks in the BLS power spectrum, we estimated 0.1%, 1% and 10% false alarm probability (FAP) thresholds. We also determined FAP as a function of orbital period (FAP(P)) by calculating the FAP thresholds for 20 period ranges, each with an equal number of frequencies to be searched for by the BLS algorithm. To explore peaks in the BLS power spectra that have low power, we used Huber's robust estimator of scale and location to estimate the mean and standard deviation of the power spectrum in each of the 20 period ranges. The majority of the highest peaks of the BLS power spectrum fall below the FAP and FAP(P) thresholds. We note that there is no significant power in the power spectrum near the orbital period of Proxima b (Anglada-Escudé et al., 2016); however we have identified 12 peaks that are above the robust mean plus 3 and 5 times the standard deviation. We then phase folded those 12 peaks and examined individual light curves that contribute to those periods. We conclude that these 12 peaks are unlikely to be caused by transit events.

To test our sensitivity for detecting transit-like events, we injected 550 fake transits with parameters differing in transit depth, orbital phase and orbital period. We were able to detect most injections at transit depths 4 mmag and greater up to an orbital period of 11.186 days across multiple orbital phases. Overall, we were unable to confirm the existence of transits of Proxima b. In our upcoming Paper III (D.L. Feliz et al., in preparation), we intend to model the numerous flares in our data as well as the correlated noise to reduce the scatter in our light curves and con-

duct a more thorough period finding search.

Software Used:

AstroImageJ (Collins et al., 2017), EXOFAST website[3] (Eastman et al., 2013), VARTOOLS (Hartman & Bakos, 2016), and PyTransit (Parviainen, 2015).

Chapter 4

NEMESIS: Exoplanet Tra*N*sit Surv*E*y of Nearby *M*-dwarfs in T*ES*S Full Frame *I*mage*S*

Abstract

In this work, we present the analysis of 33,054 M-dwarf stars located within 100 parsecs in the Transiting Exoplanet Survey Satellite (TESS) Full Frame Images (FFIs) of the observed sectors $1-5$. We present a new pipeline called NEMESIS which was developed to extract detrended photometry and perform transit searches of single sector data in TESS FFIs. As many M-dwarfs are faint and are not observed with a 2 minute cadence by TESS, FFI transit surveys can give an empirical validation of how many planets are missed by using the 30 minute cadence data. In this work, we detected 183 threshold crossing events and present 29 planet candidates for sectors $1-5$, 24 of which are new detections. Our sample contains orbital periods ranging from $1.25-6.84$ days and planetary radii from $1.26-5.31$ $R_{\oplus}$. With the addition of our new planet candidate detections along with previous detections observed in sectors $1-5$, we calculate an integrated occurrence rate of 2.49 ± 1.58 planets per star for the period range $\in [1,9]$ days and planet radius range $\in [0.5,11]$ $R_{\oplus}$. We project an estimated yield of 122 ± 11 transit detections of nearby M-dwarfs. 23 of our new candidates have Signal to Noise ratios > 7, Transmission Spectroscopy Metrics > 38 and

Emission Spectroscopy Metrics > 10. We provide all of our data products for our planet candidates through the Filtergraph data visualization service located at https://filtergraph.com/NEMESIS.

4.1   Introduction

The Transiting Exoplanet Survey Satellite (TESS; Ricker et al. 2014) is the first nearly all-sky space-based transit search mission and was launched on April 18, 2018. Over the course of its two year mission, TESS has covered $\sim 85\%$ of the sky which is split up into 26 observational sectors (13 per hemisphere). The TESS observing field-of-view covers a $24°\times96°$ region of sky, spanning from the ecliptic equator to an ecliptic pole ($6°$ to $96°$ in ecliptic latitude), with a time baseline of approximately 27 days per each of the 26 sectors per celestial hemisphere. In year one of the mission, the southern hemisphere was observed, with year two observing the northern hemisphere. Each sector is continuously covered by Full Frame Images (FFIs) with a 30 minute cadence and pre-selected stars are observed in smaller image cutouts called Target Pixel Files (TPFs) (also commonly referred to as "postage stamps") with a 2 minute cadence. All TESS images have a pixel scale of $21''$ per pixel. Full details of the TESS observing strategy and instrument characteristics can be found in the TESS Instrument Handbook[12].

One of the primary goals of the TESS mission is to survey over 200,000 stars in order to discover planets with periods < 10 days and radii < 2.5 R$_\oplus$ orbiting the brightest stars in the solar neighborhood. FFIs greatly increase the missions potential for new transit detections with some simulations projecting $\sim 10^3$ FFI transit detections (Barclay et al. 2018; Huang et al. 2018). Due to the large amount of storage and data processing required for FFIs, not every star in the TESS Input Catalog (TIC, Stassun et al. 2018, Stassun et al. 2019) receives 2 minute cadence observations.

The pre-selection of stars with 2 minute cadence observations are mostly comprised of bright, isolated stars while many dimmer stars, including M-dwarfs, are typically excluded and only are

---

[12] https://heasarc.gsfc.nasa.gov/docs/tess/documentation.html

observed with the 30 minute cadence. Interest in M-dwarf stars as hosts for planets has increased in recent years as the field of exoplanet discovery has grown (Plavchan, 2006). Due to being smaller, cooler main sequence stars, M-dwarfs typically have habitable zones (where liquid water can exist on a planet's surface) at much smaller orbital distances when compared to more luminous stars. As a result, planets that happen to orbit in these habitable zones will orbit more frequently. Since M dwarfs comprise roughly 70% of all stars in the Milky Way galaxy (Bochanski et al., 2010), they offer the best current chance of finding and characterizing habitable planets through sheer numbers and proximity to the Sun. M-dwarf stars also offer a plethora of observational opportunities for exoplanet transit detections. Due to M-dwarfs being small main sequence stars, small planets are easier to detect via the transit method as photometric transit depths are larger due to the smaller star to planet radius ratios.

Previous studies of occurrence rates of short period planets around Sun-like stars have revealed a bimodal distribution in planetary radii that is commonly referred to as the radius valley (Fulton et al. 2017; Fulton & Petigura 2018; Mayo et al. 2018). The transition between rocky and non-rocky planets around Sun-like and low mass stars have been found to be dependant on orbital period (Van Eylen et al. 2018; Martinez et al. 2019; Wu 2019; Cloutier & Menou 2020). The slope of the radius valley around Sun-like stars was measured by (Martinez et al. 2019, M19 hereafter) where they used the California-Kepler Survey (CKS) stellar sample from Fulton et al. 2017 and found their slope to be consistent with model predictions from thermally driven atmospheric mass loss (Lopez & Rice, 2018). Van Eylen et al. 2018 (VE18 hereafter) also measured the planet radius-period slope of the radius valley for their sample of FGK stars characterized by asteroseismology. Another interpretation for the existence of the radius valley around low mass stars is that thermally-driven mass loss is dependant on stellar mass and overall less efficient for mid to late M-dwarfs due to gas-poor environments (Cloutier & Menou 2020, CM20 hereafter). CM20 also found that for low mass stars, the transition between rocky planets and non-rocky planets in the

78

radius valley is centered around 1.54 $R_\oplus$.

The Science Processing Operations Center at NASA Ames (SPOC, Jenkins et al. 2016) which produce calibrated light curves and validation reports for Threshold Crossing Events (TCEs) that pass various tests vetted by humans, also produce TESS Objects of Interest (TOIs) for a subset of targets that are observed with 2 minute cadences. The MIT Quick Look Pipeline (QLP, Huang et al. 2020) also produces calibrated light curves and validation reports for stars observed in FFIs with TESS magnitudes < 13.5 and the QLP team also contributes to providing additions to the TOI catalog[13]. The DIAmante pipeline (Montalto et al., 2020) was used to conduct a transit survey that has produced 396 Community TESS Objects of Interest (cTOIs)[14] for a subset of FGKM stars observed in TESS FFIs from sectors 1 – 13. In this work, we explore the detectability of exoplanets transiting nearby M-dwarf stars using our custom pipeline, NEMESIS which was designed to extract photometry and detect transits observed in TESS FFIs for TESS sectors 1 – 5.

In Section 4.2, we describe the observations by TESS and our selection criteria for selecting target stars to conduct our transit survey on. In Section 4.3, we discuss our process of extracting photometric time series from the FFI images. In Section 4.4, we discuss our approach to searching for transiting exoplanets, our process for vetting planet candidates and testing the sensitivity of our pipeline's ability to detect transit events. In Section 4.5, we present our list of planet candidates and compare them to other known transiting exoplanets and planet candidates from the TOI and DIAmante catalogs as well as explore the ability of our pipeline to detect transits of short period planets (< 10 days). In Section 4.6, we discuss our results, the limitations of our analysis and areas for improvement for future work. In Section 4.7, we discuss our final conclusions.

---

[13] https://tess.mit.edu/toi-releases/   [14] https://archive.stsci.edu/hlsp/diamante

4.2 Target Star Selection

To filter through all stars observed by TESS, we utilized the Tess Input Catalog Version 8 (Stassun et al., 2019) to access stellar parameters and utilized the Barbara A. Mikulski Archive for Space Telescopes (MAST) CasJobs[15] service to get a target list of M-dwarf stars. The selection criteria used to create our stellar sample is: 2300 $K <$ $T_{eff} <$ 4000 K, TESS magnitude $<$ 18, distance $<$ 100 pc, $R_{Star} < 0.5$ $R_\odot$ and $M_{Star} < 0.5$ $M_\odot$. To assist in avoiding contamination of red giants in our target star sample, we also employ the use of surface gravity cuts (logg > 3). To remove high proper motion targets and stars that are bluer or redder than most of our sample stars, we employ a reduced proper motion cut in the J-band of $5 < RPM_J < 20$ and a color cut $0.4 < J - H < 0.75$ as shown in Figure 4.1. RPM_J is defined as:

$$RPM_J = J - 5\log(\sqrt{\mu_\delta^2 + \mu_\alpha^2 \cos\delta}) \tag{4.1}$$
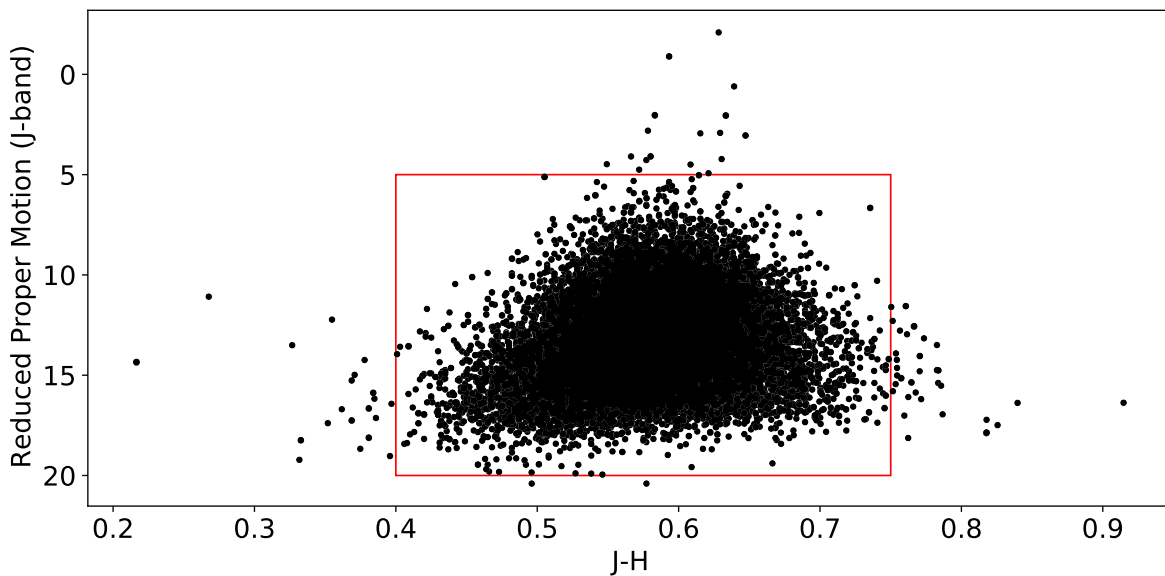
Figure 4.1: J-H color versus reduced proper motion (RPM_J). We selected a J-H cut of 0.4 to 0.75 and a reduced proper motion cut of 5 to 20 to exclude targets that differed from the majority of the stellar sample.

To ensure that our target stars are likely M-dwarfs, we also cross matched our sample with stars with the "cooldwarf_v8" flag from the Cool Dwarf Catalog (Muirhead et al., 2018) within the

---

[15] http://mastweb.stsci.edu/mcasjobs/

special lists category of the TIC. In Figure 4.2, we display the number of M-dwarf stars that meet our selection criteria that are observed with 2 minute and 30 minute cadences.
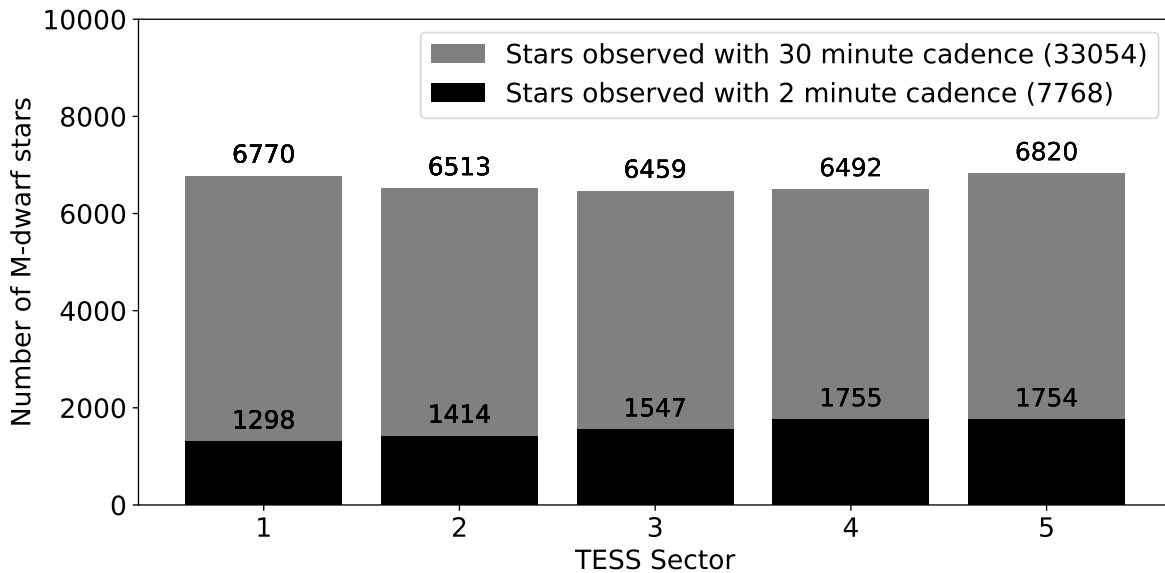
Figure 4.2: Number of M-dwarf stars observed with 2 minute and 30 minute cadences.

In Figure 4.3, we display the ecliptic coordinates of our M-dwarf target stars in TESS Sectors 1 – 5 along with other known planets from the Exoplanet Archive[1] and planet candidates from the TOI and DIAmante catalogs for nearby M-dwarf host stars. In Figure 4.4, we display the distributions of various stellar parameters of our target list.
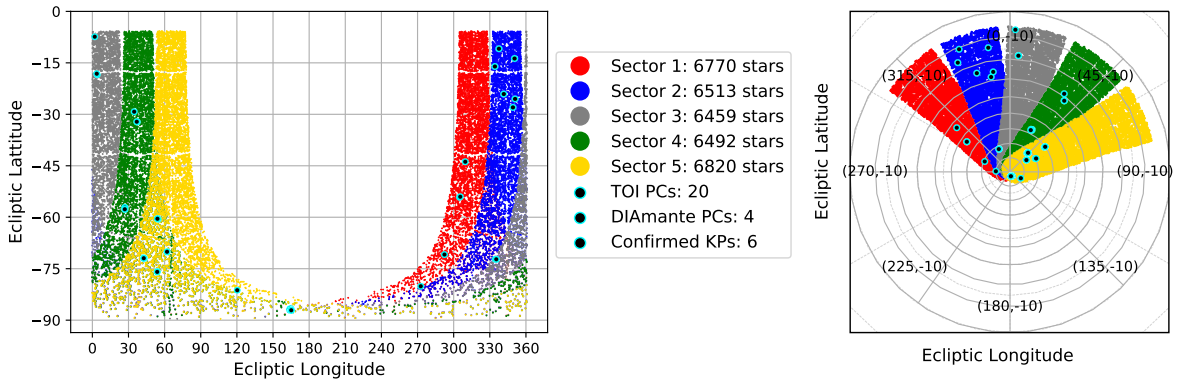
Figure 4.3: Coordinates of all M-dwarfs in TESS sectors 1 – 5 within 100 pc. *Left:* Target lists shown in ecliptic coordinates. *Right:* Target lists projected onto celestial sphere with southern ecliptic pole centered at (0,-90). Known transiting planets that are confirmed (KPs), TOI and DIAmante Planet Candidates (PCs) transiting their M-dwarf host stars that are observed in sectors 1 – 5 are marked as black points with cyan outlines.
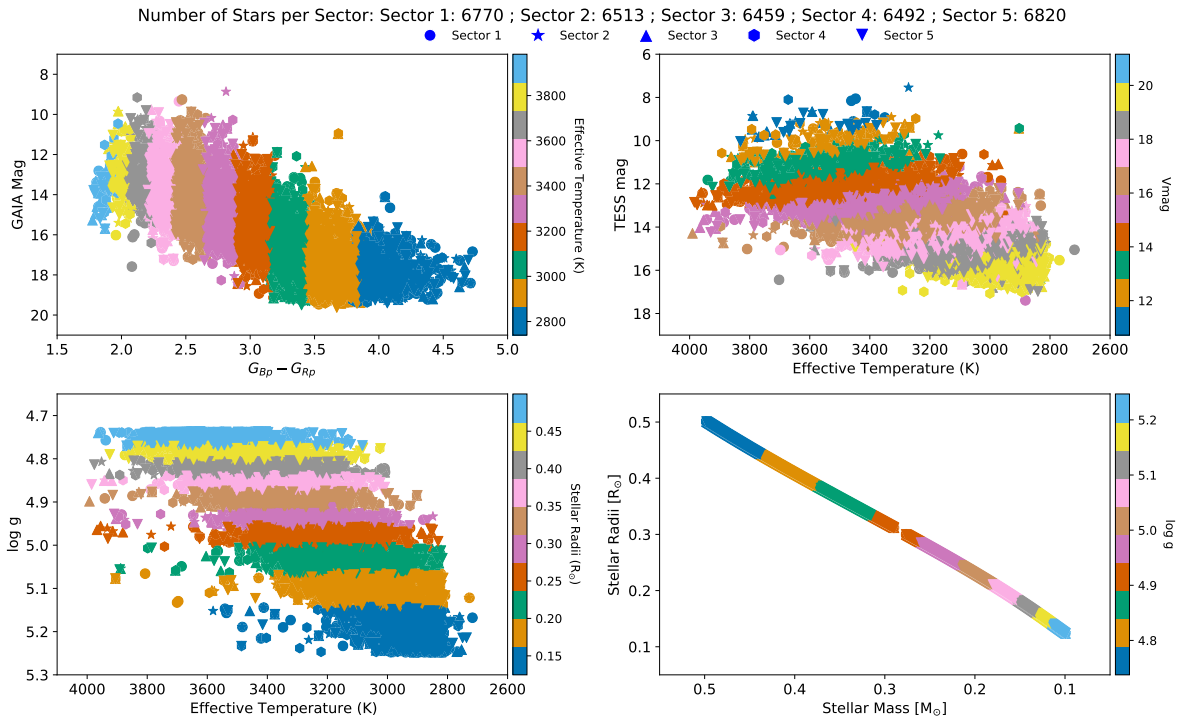
Figure 4.4: Stellar parameters of all M-dwarfs in TESS sectors 1 – 5 that follow our selection criteria as described in Section 4.2.

4.3   Data Acquisition and Reduction

In Sections 4.3.1 to 4.3.6, we describe our light curve extraction pipeline as outlined in Figure 4.5.
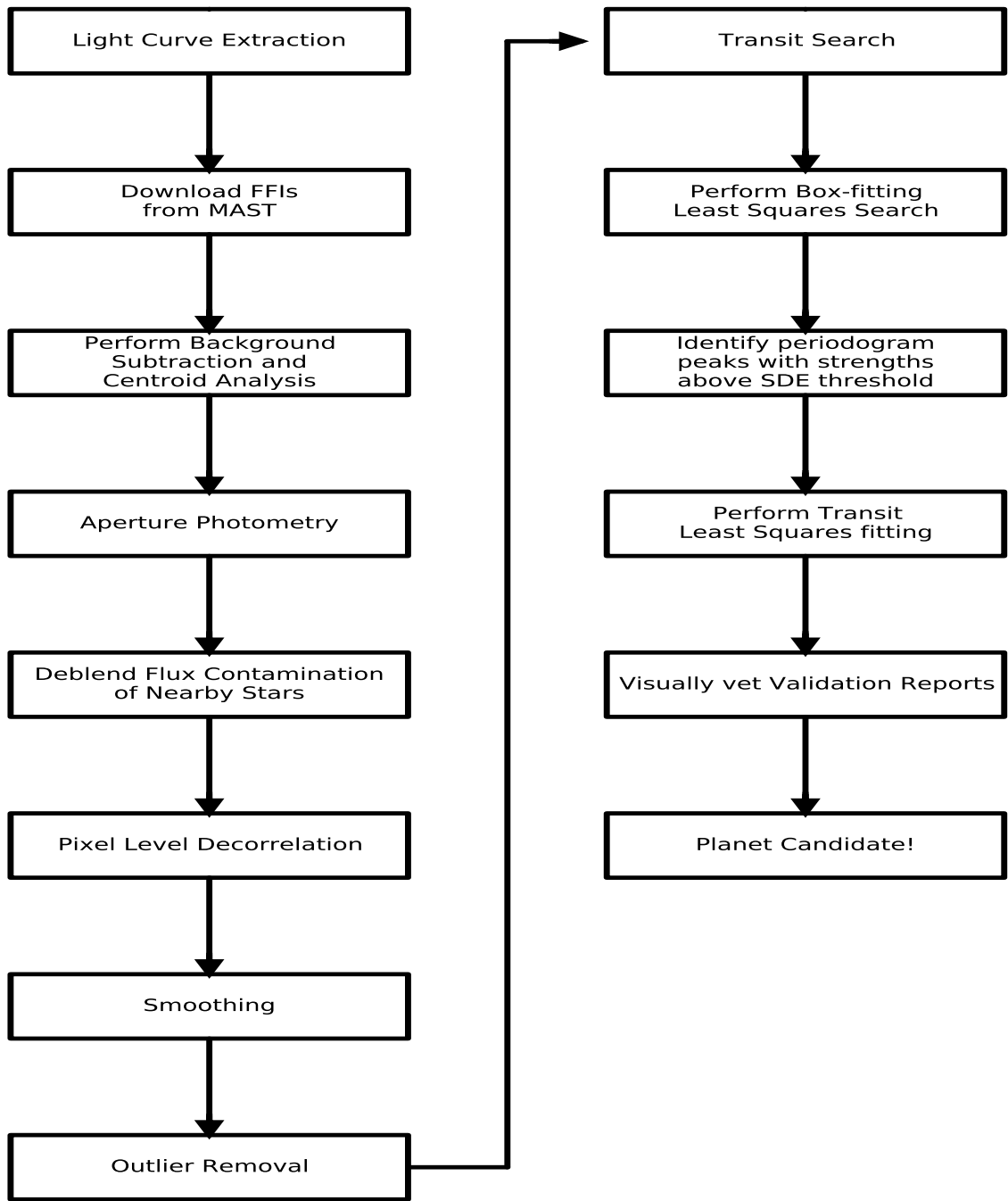
Figure 4.5: A schematic of the steps in our light curve extraction (left) and transit search pipeline (right). These steps are detailed in Sections 3.1-3.6.

4.3.1 Processing Full Frame Images

Using the Python package Astroquery (Ginsburg et al., 2019) to query the TIC from MAST, we obtain the stellar radius and mass which we can use to cross match the quadratic limb-darkening parameters from Claret 2017 for each target star by using the "catalog_info" function from the Transit Least Squares (Hippke & Heller, 2019) package. We then perform a radial cone search for each target star using a radius of $21''$ and obtain the Right Ascension and Declination coordinates. With the celestial coordinates, we then download each target star's FFI square cutout 11 × 11 pixels in size) from MAST using the TESSCut (Brasseur et al., 2019) service.

4.3.2 Background Subtraction and Aperture Photometry

TESS periodically fires its thrusters to unload the angular momentum built up from solar photon pressure at perigee and throughout its orbit. These are commonly referred to as momentum dumps and are described in more detail in the Data Release Notes (DRN)[16] that are produced for each sector. Additionally, the DRN have brief descriptions of when observations contain high amounts of telescope jitter or glare from the Earth and/or the Moon in the FFI field of view. For each FFI cutout around the target star, we first refer to the quality flags described by the DRN to remove specific cadences (with non-zero bitmask flag values) where various types of anomalies are detected. We also remove durations of spacecraft adjustments to maintain pointing stability, also discussed in the DRN.

To estimate the pixel masks for the sky background in each image, we find the dimmest pixels in the FFI cutout using a brightness threshold of 1/1000 standard deviations below the median flux of the images. We then sum the counts in the background mask and normalize the background flux. To identify the optimal aperture mask around the target star, we perform a centroid analysis around the target's pixel position on the median brightness image using a bivariate quadratic function to

---

[16] https://archive.stsci.edu/missions/tess/doc/tess_drn/

approximate the core of a Point Spread Function. This centroiding technique is also used in the Eleanor FFI pipeline (Feinstein et al., 2019) and is described in more detail in Vakili & Hogg 2016.

With the approximation of the target star's location in the FFI cutouts, we then look for pixels with flux above a brightness threshold of 7.5 standard deviations above the median flux of the images. When comparing to the SPOC optimal apertures for TPFs, we found that a brightness threshold of 7.5 standard deviations is typically a close approximation for both FFIs and TPFs. To calculate the background subtracted flux for our selected pixel masks, we use a Simple Aperture Photometry (SAP) approach defined as:

$$F_{BKG} = \frac{\sum_{i,j} F(ap_{BKG}(i,j))}{N_{pix,ap_{BKG}}} \tag{4.2}$$

$$F_{SAP} = \sum_{i,j} F(ap_{TGT}(i,j)) - F_{BKG} \times N_{pix,ap_{TGT}} \tag{4.3}$$

where F is the image flux, ap is the background (BKG) and target (TGT) pixel masks, i and j are the pixel coordinates of each image and N_{pix} is the number of pixels in the masks. With the background flux subtracted, we then normalize the SAP flux to have baseline centered at a value of 1. To remove the sharp changes in flux due to the momentum dumps that do not have quality flag values indicating bad data, we remove data points that occur 30 minutes before and after each thruster firing event.

4.3.3 Deblending Flux Contamination from Nearby Stars

To account for potential extra light from nearby stars that contaminates our aperture photometry, we query the TIC for all sources within 3 TESS pixels of the target star (∼1 arcminute) and record their TESS magnitudes. Typically, our automatically selected apertures spread across 2–3

TESS pixels so a radial cone search of 3 TESS pixels wide is a reasonable general approximation. We calculate the dilution factor as:

$$f = 1 - \frac{10^{-T_{\text{mag,target}}/2.5}}{\sum_i^{N_{\text{stars in aperture}}} 10^{-T_{\text{mag,i}}/2.5}} \tag{4.4}$$

We then subtract our background subtracted SAP flux by the dilution factor and then re-normalize.

4.3.4   Pixel Level Decorrelation

Pixel Level Decorrelation (PLD) is an effective technique (Deming et al., 2015; Luger et al., 2016, 2018) used to remove effects of intra-pixel fluctuations that can be attributed to telescope jitter or short term variations like those caused by momentum dumps that occur through TESS observations in each sector. By identifying instrumental systematics with methods like PLD, the rate of false positive detections can be decreased for period searching algorithms like Box-fitting Least Squares (BLS, Kovács et al. 2002). Using Equations 1 – 4 from Deming et al. 2015, we utilized a 3rd order PLD to calculate a noise model for the observed time series to model the intra-pixel correlations. We then perform a Principal Component Analysis (PCA) to reduce the number of eigenvectors in our PLD noise model in order to construct a PCA design matrix and solve for the weights of the PLD model. With the instrumental systematics modeled, we can then detrend our SAP flux using the PLD noise model. From our testing, we find that using a combination of a 3rd order PLD with 3 PCA terms is most optimal for removing short term intra-pixel trends in TESS FFI photometry.

4.3.5 Smoothing

With the instrumental systematics modeled and removed with a PLD noise model, we then remove long term trends, such as the rotational modulation of starspots, by utilizing a median-based, time-windowed smoother with an iterative robust location estimator based on Tukeys biweight (Beyer, 1981) using the Wōtan (Hippke et al., 2019) Python package. Removing these trends while keeping the shapes and durations of potential transits intact can allow easier detection by period searching transit finding algorithms. To decide the optimal window size of the smoothing filter, we calculated the longest transit duration for circular orbits (b=0, i=90°, w=90°, e=0) of an Earth-sized planet transiting every 14 days (minimum of about 2 transits per sector):

$$T_{dur} = \frac{P}{\pi} \arcsin\left((R_{Star} + R_{Planet})(\frac{4\pi^2}{GM_{Star}P^2})^{1/3}\right) \tag{4.5}$$

We then use 3 times this transit duration as our smoothing window which is calculated for each target star using the stellar radius and mass queried from the TIC.

4.3.6 Outlier Removal

Once the SAP flux is extracted, known systematics due to high jitter and momentum dumps are removed, short term trends at the pixel-level and long term trends in the time series are removed, we then begin a sliding window sigma clipping routine where we remove outliers higher than ± 2 median absolute deviations above and below the median flux in a given window of data spanning the same smoothing window estimated with Equation 4.5. We are careful to include outliers that have more than 2 consecutive data points ("good outliers") in a given window as to not remove potential transit events on ~1 hour timescales. While stellar flares are typically conserved with this approach, for our transit survey we chose to remove consecutive outliers that lie above the local noise thresholds. An example of the full processing of the light curve is displayed in Figure 4.6.
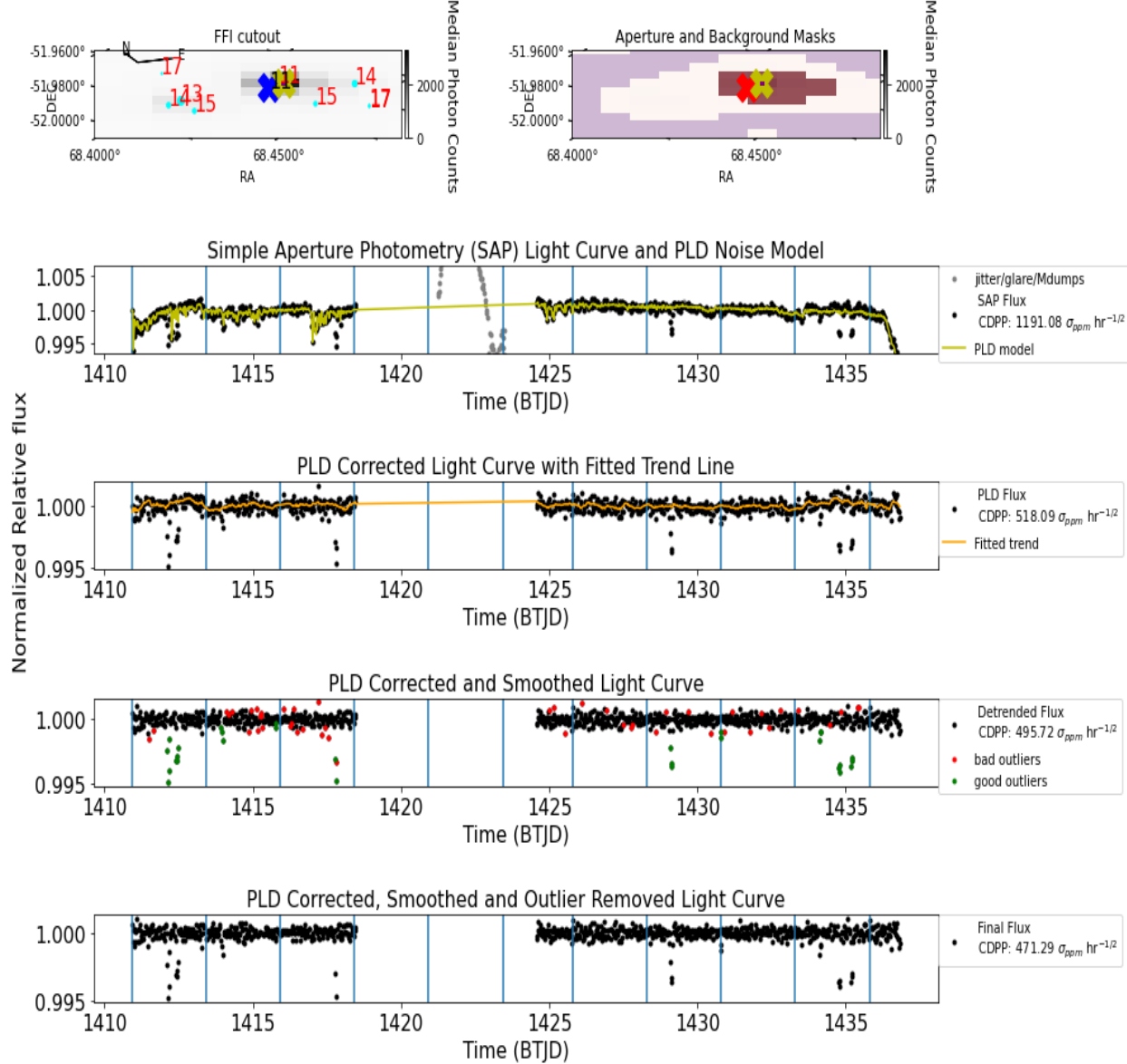
Figure 4.6: A step-by-step example of how the NEMESIS pipeline processes a light curve for TIC 259377017 observed in Sector 4. *Top Left Panel:* Displays the FFI cutout with nearby stars and their GAIA magnitudes marked with cyan colored points and red text on the left panel. The blue colored X marks the pixel coordinates listed in the FFI headers. The yellow colored X marks the location of the centroid of the selected aperture. Small purple dots marker the position of the centroid for all images observed in this sector. *Top Right Panel:* The selected aperture and background masks are marked as red and purple, respectively. The red colored X here marks the pixel coordinates listed in the FFI headers for visual contrast. *Second Row:* The normalized SAP light curve in black points. Grey points are known regions of bad data referenced by the DRN (see Section 4.3.2) and data removed around momentum dumps. Momentum dumps are marked by vertical blue lines. The yellow line is the PLD noise model. *Third Row:* The normalized PLD corrected light curve is in black points with the smoothing trend line marked as a orange line. *Fourth Row:* The normalized PLD corrected, smoothed light curve is in black points. Bad outliers that are not consecutive in time are marked in red points. Good outliers that are consecutive in time are marked in green points. *Fifth Row:* The final normalized PLD corrected, smoothed and outlier removed light curve. At all steps of processing, we display the Combined Differential Photometric Precision (CDPP) on the right side of each light curve. These step-by-step summary figures are produced for each star analyzed by NEMESIS.

To check the quality of our light curves produced by our pipeline at each step, we calculate the Combined Differential Photometric Precision (CDPP [ppm hr$^{-1/2}$]) as shown in Figure 4.7. We also compare our CDPP values with the pre-flight theoretical precision of TESS, estimated by Sullivan et al. 2015 and find that the quality of many of our processed light curves exceeds the predicted quality of this model.
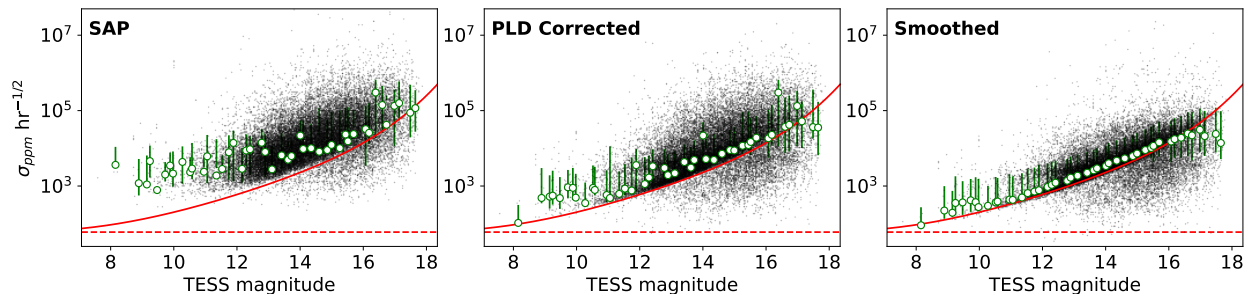
Figure 4.7: Combined Differential Photometric Precision (CDPP) for all processed light curves from our stellar samples observed in TESS sectors 1–5, from beginning of light curve extraction (left panel) to the end (right panel). The light curve extraction procedure is described in Section 4.3. The binned median CDPPs are shown as green circles with the error bars spanning from the 25th quantile to the 75th quantile in each TESS magnitude bin. The solid red line is the expected theoretical precision estimated in Sullivan et al. 2015 which is a combination of noise contributions from zodiacal light, instrumental read noise, photon counting noise and the systematic noise floor. The systematic noise floor (60 ppm hr$^{-1/2}$) is shown as a horizontal dashed red line.

4.4 Methodology: Transit Detection and Vetting

4.4.1 Transit Searches with BLS and TLS

The Box Least Squares (BLS) algorithm (Kovács et al., 2002, 2016) is a widely used tool in the exoplanet transit searching community. BLS approximates the transit light curve as a boxcar function with a normalized average out-of-transit flux of one and a fixed depth during the transit. BLS has a high Signal Detection Efficiency (SDE) for Neptune and Jupiter sized planet transits but for smaller planets where the transit depths are comparable to instrumental and stellar noise, the SDE becomes much lower. This can also prove to be challenging for dim stars like M-dwarfs that may have a lot of photometric scatter.

The Transit Least Squares algorithm (TLS[17], Hippke & Heller 2019) was created as an alternative analysis to the BLS algorithm in order to be more sensitive to smaller Earth-sized planetary transits. Unlike BLS that searches for box-like periodic flux decreases in the light curve, TLS utilizes a analytical transit model with stellar limb darkening (Manduca et al. 1977; Mandel & Agol 2002b). Hippke & Heller 2019 found that the false positive rate was suppressed when comparing algorithms on transit injected light curves due to higher detected signal-to-noise ratios. A comparison between the two algorithms on a simulated light curve is displayed in Figure 4.8. In this work, we utilize the Astropy implementation of BLS[18] alongside with TLS.
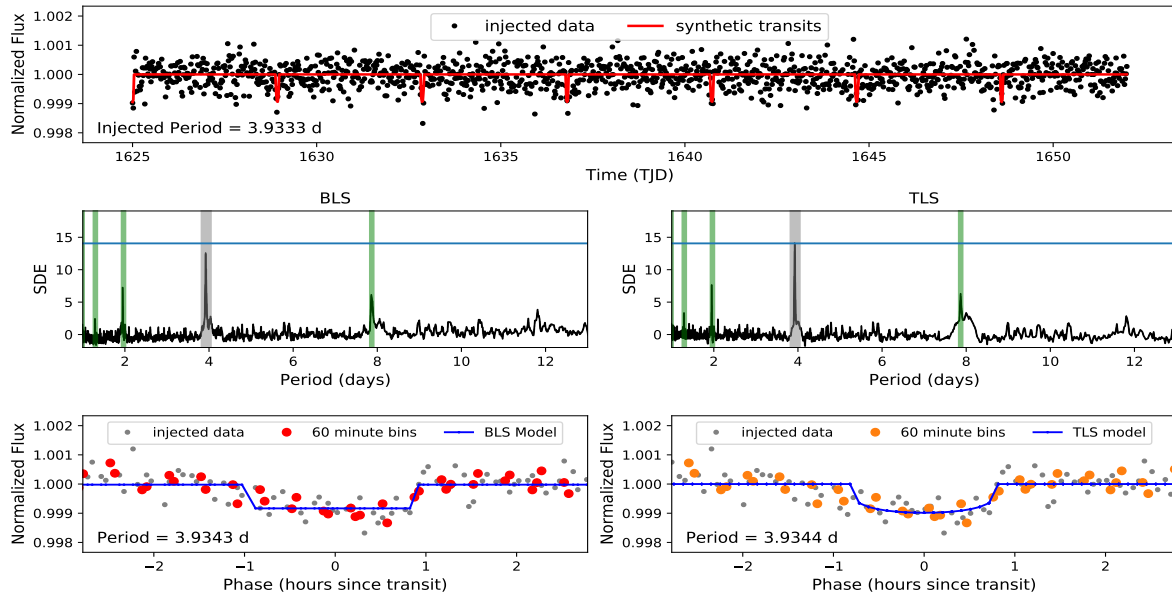
Figure 4.8: Example recovery of a simulated TESS light curve (30 minute cadence, 400 ppm scatter) injected with a synthetic planet transit (Period = 3.93 days, R_P = 1.5 $R_\oplus$, circular orbit) with both the Box Least Squares (BLS) and Transit Least Squares (TLS) methods. The vertical grey shaded line is the injected period and the vertical green shaded lines are aliases of the injected period. While the transits are detected by both BLS and TLS, TLS can be a favorable transit detection algorithm due to higher Signal Detection Efficiencies (SDE) measured for the fitted transit models when compared to the fitted box models that BLS produces.

While TLS may be more optimal at detecting smaller planets, it is more computationally expensive than BLS to run. To minimize the computation time of transit searches in this survey, we first perform a BLS search and look for the strongest peaks in the resulting BLS power spectra.

---

[17] https://transitleastsquares.readthedocs.io/en/latest/index.html   [18] https://docs.astropy.org/en/stable/timeseries/bls.html

To select the grid of trial periods to search over for each target star, we utilize TLS' "*period_grid*" function which estimates the optimal frequency sampling as a function of stellar mass and radius as detailed in Ofir 2014. Using this period grid, we also use TLS' "*duration_grid*" function to estimate the trial fractional transit durations (duty cycles) to fit various transit models over. For the period grid, we use a oversampling factor of 9 and for the duration grid, we use a logarithmic step size of 1.05. In order to avoid false positive detections due to fast stellar rotation of active M-dwarf stars that may have residual trends that survived our detrending process, we set the minimum period of our period grid to be 1 day. We also require each transit search have at least 3 modeled events which places an upper limit on the maximum period of our period grid to be ∼9 days which is ∼1/3rd of the duration of a single sector TESS light curve.

Other studies have found empirical SDE thresholds ranging from 6 to 10 (Siverd et al., 2012; Dressing & Charbonneau, 2015; Pope et al., 2016; Aigrain et al., 2016; Livingston et al., 2018; Wells et al., 2018) to be optimal in reducing the overall number of false positives. While higher SDE thresholds typically result in less false positives, lower SDE thresholds provide more completeness. With this in mind, we utilize a minimum TLS SDE threshold of 10 in this work to reduce the amount of potential false positive detections we may have encountered. Once we run the faster BLS transit searches, for any target stars that display strong SDEs ≥ 6 in the BLS power spectra, we then run a TLS transit search on the same light curve to get a better transit fit of the signal causing the initial detection. For the TLS transit searches, we use the same period and duration grids used for BLS. For both BLS and TLS transit searches, we record the transit parameters corresponding to the strongest peak in their respective power spectra.

4.4.2 Vetting Process

One of the many challenges of transit surveys is weeding out the false positive detections through a post-detection vetting process. Some scenarios that can trigger a false positive detection

can be short term periodic stellar variations, eclipsing binary stars, blended photometry from two stars on 1 pixel or periodic movement of the centroid. For our vetting process, we use a one page validation report (see Appendix C) that is similar to the validation reports from SPOC, QLP and DIAmante, which contains visual comparisons to other catalogs and archival images (e.g., Gaia, Digitized Sky Survey), as well as several tests to attribute periodic transit-like behavior to planetary transit events. With the metrics produced by these tests, we then visually vet each candidate and refine our TLS searches with finer period and duration grid step sizes. Additionally, we also perform an alternative Lomb-Scargle analysis on each SAP, PLD and Detrended light curve to search for stellar activity that may be triggering transit detections from BLS or TLS. For each TCE, we then vote on whether or not it may be due to planetary transits, as follows.

4.4.2.1   Odd/Even Mismatch Test

To search for potential transit detections that may be attributed to eclipsing binaries, we utilize the odd-even mismatch test which will compare the primary and secondary transit events in orbital phase. For an unequal size ratio eclipsing binary, the secondary event will be a smaller fraction of the primary events transit depth and if the orbit of the transiting star is circular, it will occur at an orbital phase = 0.5. To perform this test, we cut 1 day regions around the transit times modeled by TLS and append them separately into odd and even numbered transits. To produce a metric that compares the odd and even transits, we use:

$$\text{Odd Even Mismatch} = \frac{|\delta_{\text{odd}} - \delta_{\text{even}}|}{\sigma_{\delta_{\text{odd}}} + \sigma_{\delta_{\text{even}}}} \tag{4.6}$$

where δ and σ_{δ} denote the transit depth and transit depth uncertainty of the odd and even numbered transits as measured by TLS. In addition to the odd-even mismatch statistic, we also visually inspect the phase folded light curves at 0.5, 1 and 2 times the TLS detected period.

4.4.2.2 Centroid Motion Test

Another challenge of performing automated aperture photometry in an all-sky survey is making sure that the selected apertures stay on target throughout the duration of transit events. As described in Section 4.3.2, we utilize a bivariate quadratic function to estimate the photocenter around a target star's pixel position for the image corresponding to the median brightness. To verify whether or not there is motion of the centroid during the time of transit detected by TLS, we phasefold the pixel positions of the centroid over time. We track centroid motion by calculating the change in pixel position in the image columns and rows by subtracting their median pixel positions. If the centroid motion exceeds 5 standard deviations from the pixel position in the image columns and rows during the time of transit, we consider this a false positive detection.

4.4.3 EDI-Vetter Unplugged

To help provide an alternative reference analysis for our false positive tests, we utilize a modified version of the EDI-Vetter Python package (Zink et al., 2020). The EDI-Vetter tool was used to automatically vet planet candidates in campaign 5 of the Kepler K2 mission. The EDI-Vetter Unplugged[19] package is a simplified version of the base package that is modified to use the outputs from TLS. The various false positive tests that the EDI-Vetter Unplugged package performs are described in more detail in Section 3 of Zink et al. 2020 and are briefly summarized as followed:

– *Flux contamination Test:* A calculation done to check for significant contributions of flux from stars that might lie on neighboring pixels.

– *Outlier Detection Test:* A check for outliers during the transit time that might cause a false positive detection.

– *Individual Transit Test:* A comparative check of the signal to noise ratios of individual transits with the SDE threshold > 10 used in our transit search.

---

[19] https://github.com/jonzink/EDI_Vetter_unplugged

– *Even/Odd Mismatch Test:* A check to see if the odd/even mismatch metric output by TLS is greater than 5σ.

– *Uniqueness Test:* This test identifies cases where the phase folded light curve appears to contain several transit-like dips that may appear similar to the candidate transits.

– *Secondary Eclipse Test:* A check for statistically significant secondary transit events at 1/2x the TLS detected period.

– *Phase Coverage Test:* With all the data removed from times of momentum dumps and for having bad quality flags, it is possible for the phase folded data to contain large gaps in the transit signal. This test is to check if the transit detection lacks sufficient data to detect a statistically significant transit event.

– *Transit Duration Limit Test:* A check to see if the detected transit duration is too long for the detected transit period.

– *False Positive Flag:* If any of these above listed tests are flagged as being True, the candidate is flagged as being a potential false positive that should require a closer inspection.

4.5   Results

In this section, we present the results of our search for new transiting planet candidates among M-dwarf stars observed in the TESS FFIs, as well as numerical and modeling tests we performed to assess the detection sensitivity and survey completeness of our detections. A listing of previously identified candidates, and notes related to whether we confirm or miss those candidates, is provided in Appendix D. With our survey completeness and list of planet candidates, we also make an estimate of planet occurrence rates for M-dwarf planet hosts.

4.5.1   New Transiting Planet Candidates

Our transit survey of 33,054 stars observed across TESS sectors 1 – 5 revealed 183 TCEs with TLS SDEs $\geq$ 10. Of those 183 TCEs, 29 are planet candidates that fulfilled our automated search and vetting criteria, 24 of which are new detections. Of our 29 planet candidates, 5 are detected transits of TOIs 269.01, 270.03 (sectors 4 and 5), 393.01, 455.01 and 1201.01. For all of our PCs, we refined the orbital parameters that describe these transiting systems with an MCMC analysis as described in Section 4.5.2. The best-fit TLS and median posterior MCMC transit orbital parameters (P, T0, R_P and b) for each of our planet candidates are displayed in Table A3.

To provide context to our planet candidates in regard to planet demographics and the radius valley, we display our planet candidates in the planet radius-period space and compare with nearby candidates from the TOI and DIAmante catalogs and other confirmed transiting planets observed in sectors 1 – 5, as shown in Figure 4.9. Confirmed transiting planets (marked as +s) were queried from the Exoplanet Archive and the TOI planet candidates (marked as $\triangle$s) were queried from the TOI catalog. The DIAmante planet candidates (marked as $\times$s) were queried from the MAST portal[14]. Planet candidates from this work are marked as $\bigcirc$s. Additionally, we highlight the planet radius-period slopes of the radius valley measured from M19 (for Sun-like stars), VE18 (for FGK stars) and CM20 (for low mass stars). We also color each confirmed planet and planet candidate by incident stellar flux (S), defined in Earth units, $S_\oplus$ as:

$$\frac{S}{S_\oplus} = \left(\frac{R_{Star}}{R_\odot}\right)\left(\frac{T_{eff}}{5777 \text{ K}}\right)^4 \left(\frac{1 \text{ AU}}{(\frac{M_{star} \text{ G P}^2}{M_\odot \text{ } 4\pi^2})^{\frac{1}{3}}}\right)^2 \tag{4.7}$$

In Figure 4.9, we also display the Kernel Density Estimate of the planet radius-period space for all planet hosting M-dwarf stars from the Exoplanet Archive using the following criteria: $T_{eff} < 4000K$, $R_{Star} < 0.5R_\odot$, $M_{Star} < 0.5M_\odot$ and $logg > 3$. In Figure A5 of Appendix D, we present a gallery of the phase folded light curves for our detected planet candidates. Each panel contains the detrended and phase folded light curve (in black points) and the median transit model

obtained through an MCMC analysis (red line) as described in Section 4.5.2. Our planet candidates range in orbital periods ranging from 1.25 – 6.84 d and planetary radii from 1.26 – 5.31 $R_\oplus$. In terms of relative incident stellar flux, our candidates range from 3.82 – 116.18 $S_\oplus$ which likely excludes any of our candidates from orbiting in the habitable zones of their host stars.
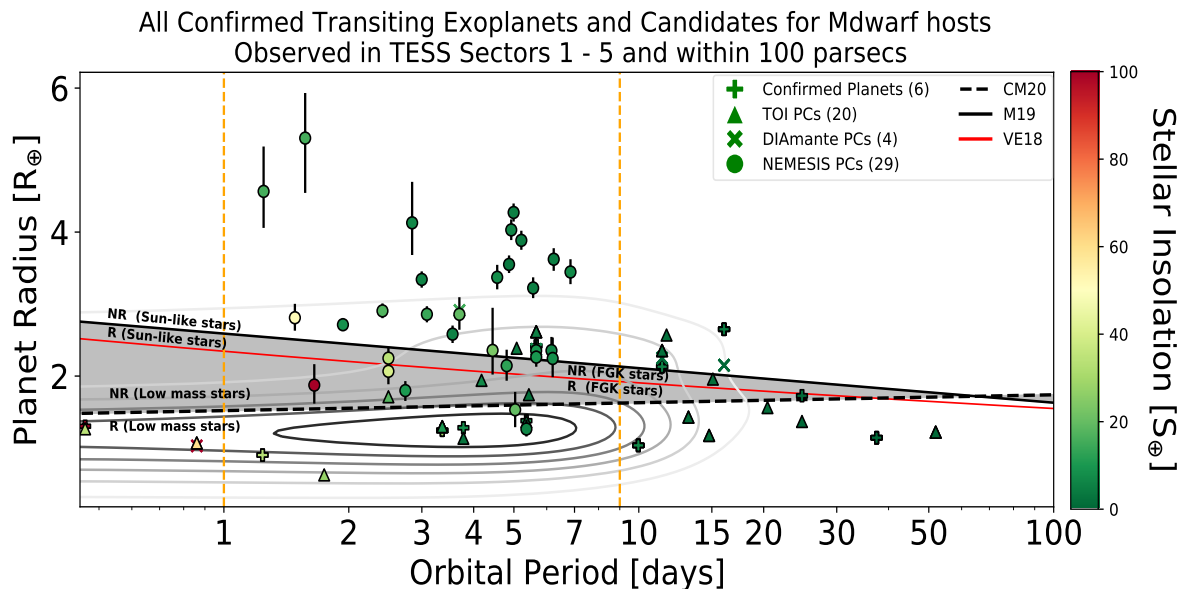
Figure 4.9: Period-radius diagram of all confirmed transiting exoplanets and exoplanet candidates observed in TESS sectors 1 – 5. Confirmed transiting planets (+s) were queried from the Exoplanet Archive[1] and the TOI planet candidates (△s) were queried from the TOI catalog[13]. The DIAmante planet candidates (×s) were queried from the MAST portal[14]. Planet candidates from this work are marked as ◯s and the vertical dashed orange lines represent the range of periods searched by our survey. All points are colored by their respective incident stellar flux (in Earth units), calculated with Equation 4.7. For comparison, over plotted are the radius valley slope for FGK stars characterized by asteroseismology (red colored line, Van Eylen et al. 2018, VE18), the approximate period-dependent radius valley slope of Sun-like stars from the CKS (solid black line, Martinez et al. 2019, M19) and the approximate period-dependent radius valley slope of low mass stars (dashed solid line, Cloutier & Menou 2020, CM20). The shaded region highlights the parameter space between the two model estimations of the radius valley from M19 and CM20. Regions above and below these slopes are inferred to be rocky (R) or non-rocky (NR) type planets. The contour lines are the Kernel Density Estimation of the period-radius space for all planet hosting M-dwarf systems from the Exoplanet Archive.

4.5.2 MCMC Transit Modeling

To model the transits of our TCEs which were denoted as planet candidates after the vetting process as described in Section 4.4.2, we employ the use of the exoplanet Python package (Foreman-Mackey et al., 2020) and model various transits in each step of our Markov Chain Monte Carlo

(MCMC) simulation. To model transits in general, **exoplanet** uses an analytical transit model computed with the **STARRY** Python package (Luger et al., 2019). Our noise model contains the following free parameters: the orbital period P, time of mid-transit T0, planet to star radius ratio R_P/R_S and impact parameter b. To define our prior distributions for the orbital period we use a log-normal distribution with a mean value set to the TLS detected period and the standard deviation set to the TLS period error. For the prior distributions used for the mid-transit time, we use a normal distribution with the mean value set to the TLS transit time and the standard deviation set to the TLS transit duration. For our prior distribution of planet to star radius ratio, we use a uniform distribution ranging from 0.01 to $R_P/R_S + \sigma_{RP/RS}$. To calculate the uncertainty for the planet to star radius ratio, $\sigma_{RP/RS}$, we query the TIC to obtain the stellar radius and its uncertainty (R_S, σ_{RS}) and propagate the errors of the stellar radius along with the planet radius uncertainty (σ_{RP}) as measured by TLS:

$$\sigma_{RP/RS} = \frac{R_P}{R_S} \sqrt{\left(\frac{\sigma_{RP}}{R_P}\right)^2 + \left(\frac{\sigma_{RS}}{R_S}\right)^2} \tag{4.8}$$

To define our prior distributions for quadratic limb darkening coefficients and impact parameter, we utilize the distributions available within the **exoplanet** package. To determine the fiducial prior distribution for quadratic limb darkening coefficients, we use a reparameterization of the two-parameter limb darkening model to allow for efficient and uninformative sampling as implemented by Kipping 2013. For the prior distributions of impact parameter, we utilize a uniform distribution ranging from 0.01 to $1 + R_P/R_S$. Our adopted model parameter priors are listed in Table 4.1. For each transit model produced in the MCMC analysis, we oversample the light curve on a fine time grid and numerically integrate over the exposure window to avoid smearing of the light curve due to TESS FFI's 30 minute cadence.

An initial maximum a posteriori (MAP) solution was found and used to initialize the parameters sampled with an MCMC analysis. The MCMC sampling was performed using the No U-Turns step-method (Hoffman & Gelman, 2014). We ran four chains with 10,000 tuning steps (tuning

samples were discarded) and 12,500 draws with a target acceptance of 99% for a final chain length of 50,000 in each parameter. Once all our runs are sampled, we then convert our posterior distributions of planet to star radius ratio to planet radii in Earth units. An example of the final posterior distributions for our free parameters and our median transit model from our MCMC analysis can be seen in Figures 4.10 and 4.11 for TOI 270 c (TIC 259377017).

Table 4.1: Example of MCMC priors used for modeling planet candidates

Parameter	Units	Prior
Period	Days	$\mathcal{N}(\ln P, \sigma_P)$
T0	BTJD	$\mathcal{N}(T0, Dur)$
$\frac{R_P}{R_S}$	–	$\mathcal{U}(0.01, R_P/R_S + \sigma_{RP})$
b	–	$\mathcal{U}(0.01, 1 + R_P/R_S)$

NOTE: For the input values of our prior distributions, we use the best-fit parameters determined by TLS: Period (P), Period error (σ_P), Transit Time (T_0), Transit Duration (Dur), Planet Radius (R_P). We calculate the planet to star radius ratio (R_P/R_S and its propagated error (σ_{RP}) with Equation 4.8.
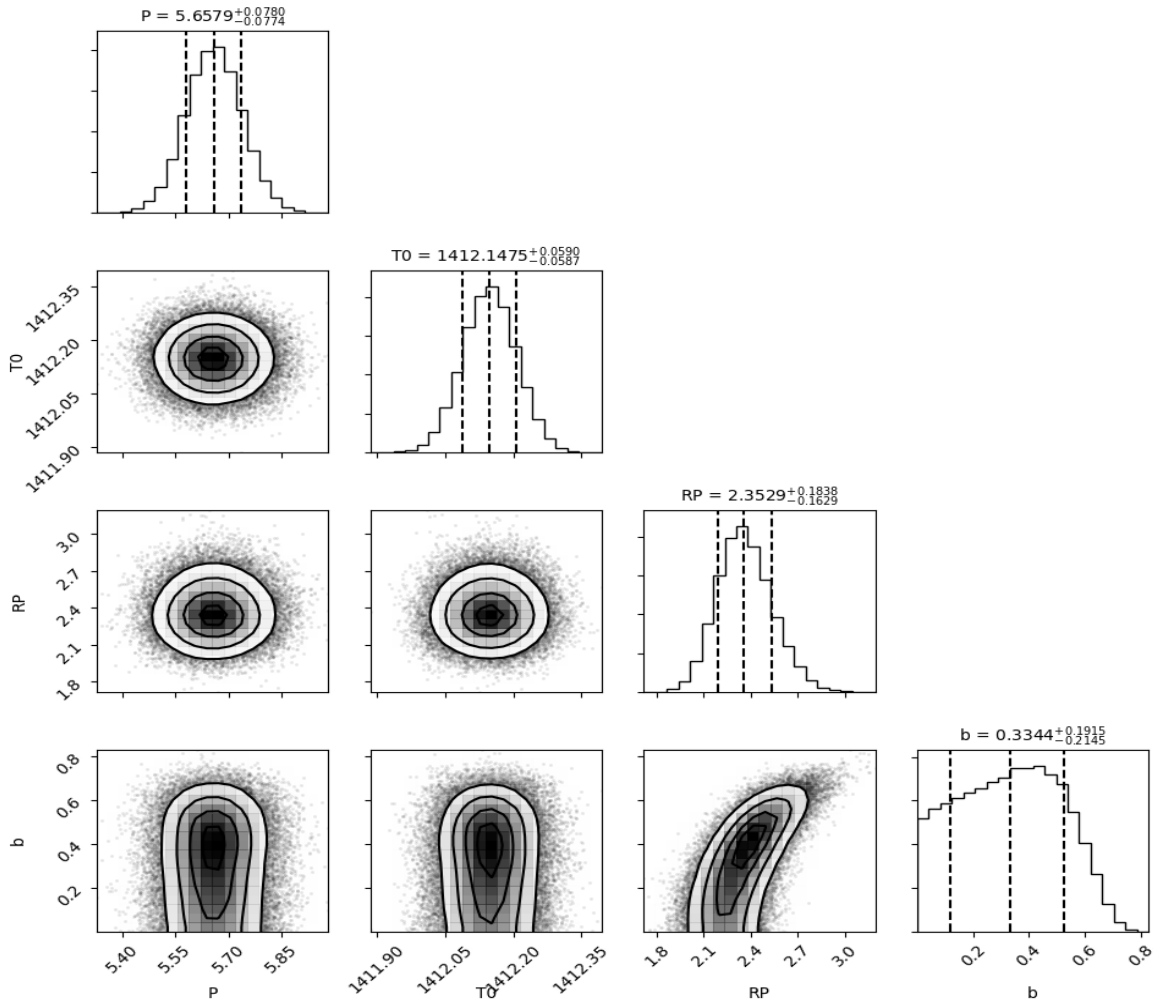
Figure 4.10: Distribution of transit model orbital parameter posteriors for planet TOI 270 c (TIC 259377017).
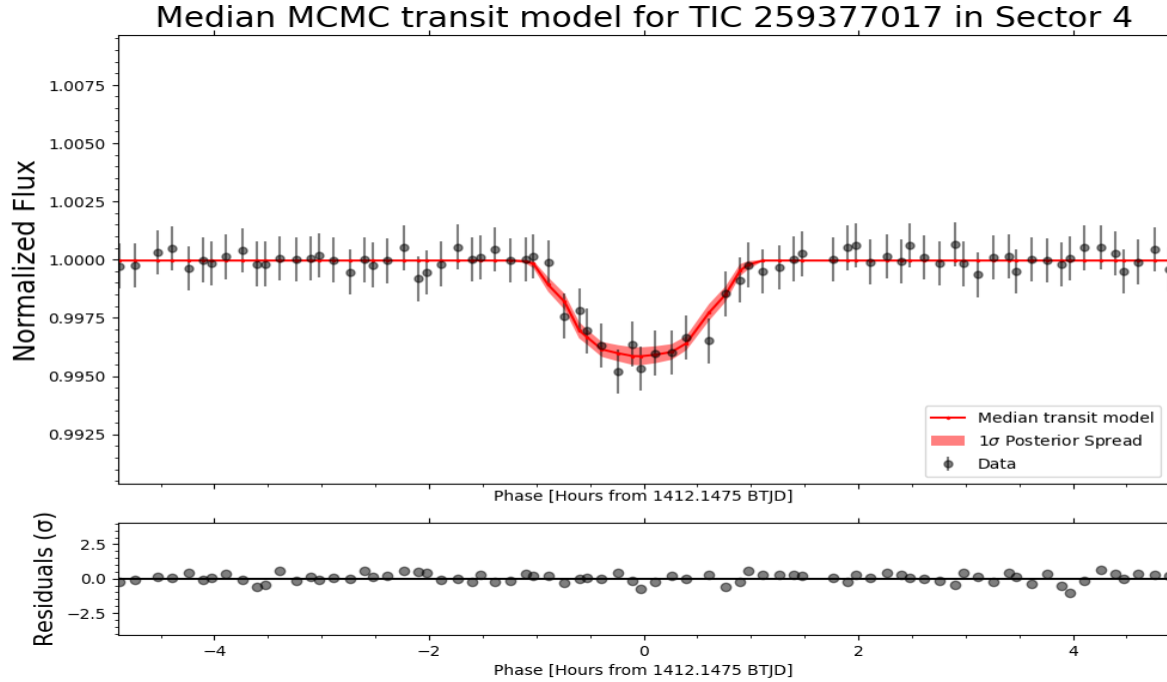
Figure 4.11: Median MCMC transit model for planet TOI 270 c (TIC 259377017).

4.5.3 Transit Injection Analysis

4.5.3.1 Transit Injection Recovery and Sensitivity

To test the detection ability of our pipeline, we used a set of simulated data. To select stars that best represented the quality of our data, we looked at our CDPP noise metrics and divided our light curves into 11 bins of TESS magnitudes as shown in Figure 4.12. For each magnitude bin, we then identified light curves that have CDPPs closest to the 0.025, 0.5 and 0.975 quantiles as representations of the best, average and worst quality data which are shown as cyan, red and orange lines in Figure 4.12, respectively. For each sector, we selected 30 stars to represent our sample. We randomly sampled uniform distributions of orbital periods ranging from 0.5 to 9 days and planet radii from 0.5 to 11 Earth radii and calculated simulated transit models using the BATMAN Python package (Kreidberg, 2015).
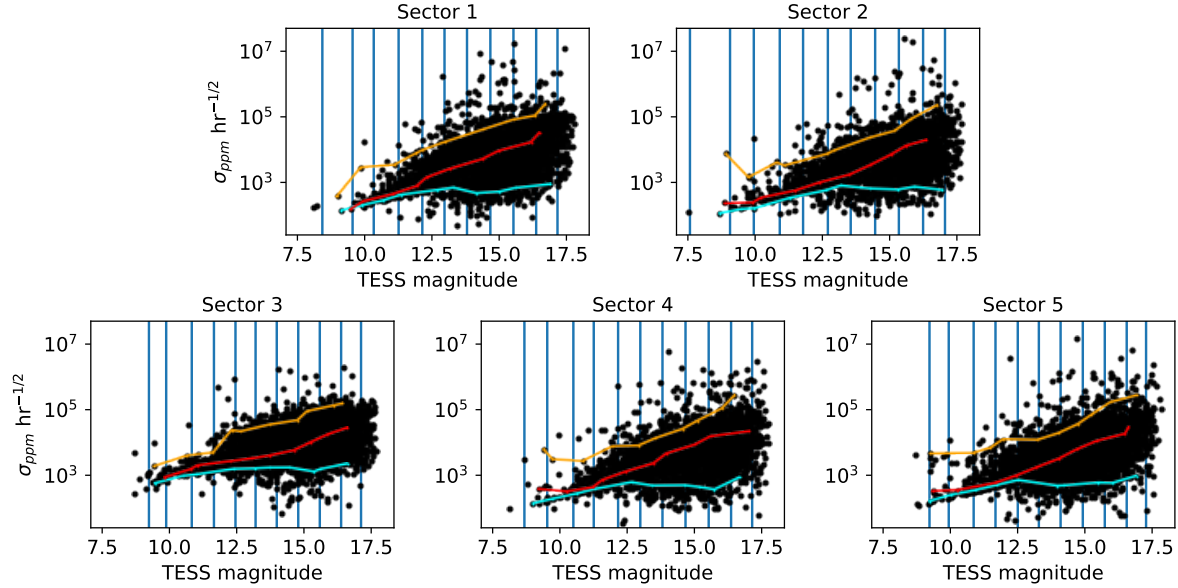
Figure 4.12: The achieved Combined Differential Photometric Precision (CDPP) for the PLD corrected and smoothed light curves from sectors $1-5$. To select stars that represent the best, average and worst quality of our light curves, we divided our data into bins of TESS magnitude and selected stars that were the closest to the 0.025, 0.5 and 0.975 quantiles of their respective magnitude bins. The stars with CDPPs closest to the 0.025, 0.5 and 0.975 quantiles are displayed by the orange, red and cyan colored line connected points, respectively.

After aperture photometry is performed on the FFI cutout of a representative star, we inject the our simulated transits, starting randomly within the first orbit of TESS in a given sector and then applied the rest of our pipeline's processes as described in Section 4.3. For each of the 30 representative stars, we used 12 randomly selected orbital periods and planet radii for a total of 21,600 transit injections across TESS sectors $1-5$. Our criteria for a successfully recovered transit is if the orbital period of the transits detected by TLS is within 1% of the injected period. To test the sensitivity of our pipeline, we add an extra criteria of checking if the injected planet radius is within the measured error of the TLS modeled planet radius. We display our 2D injection recovery rate and detection sensitivity maps in Figure 4.13. From our transit injection analysis, we can see that in the $1-9$ day regime that our transit search operates, our pipeline is sensitive to detect more than 30% of transiting planets with radius > 1 R$_\oplus$ and periods between $2-5$ days. For periods between $2-8$ days, we maintain sensitivity about > 30% for planet radii > 4 R$_\oplus$. For injected transits across the full period space explored and radii > 1 R$_\oplus$, the lower limit of our detection

sensitivity is $\sim 14\%$.
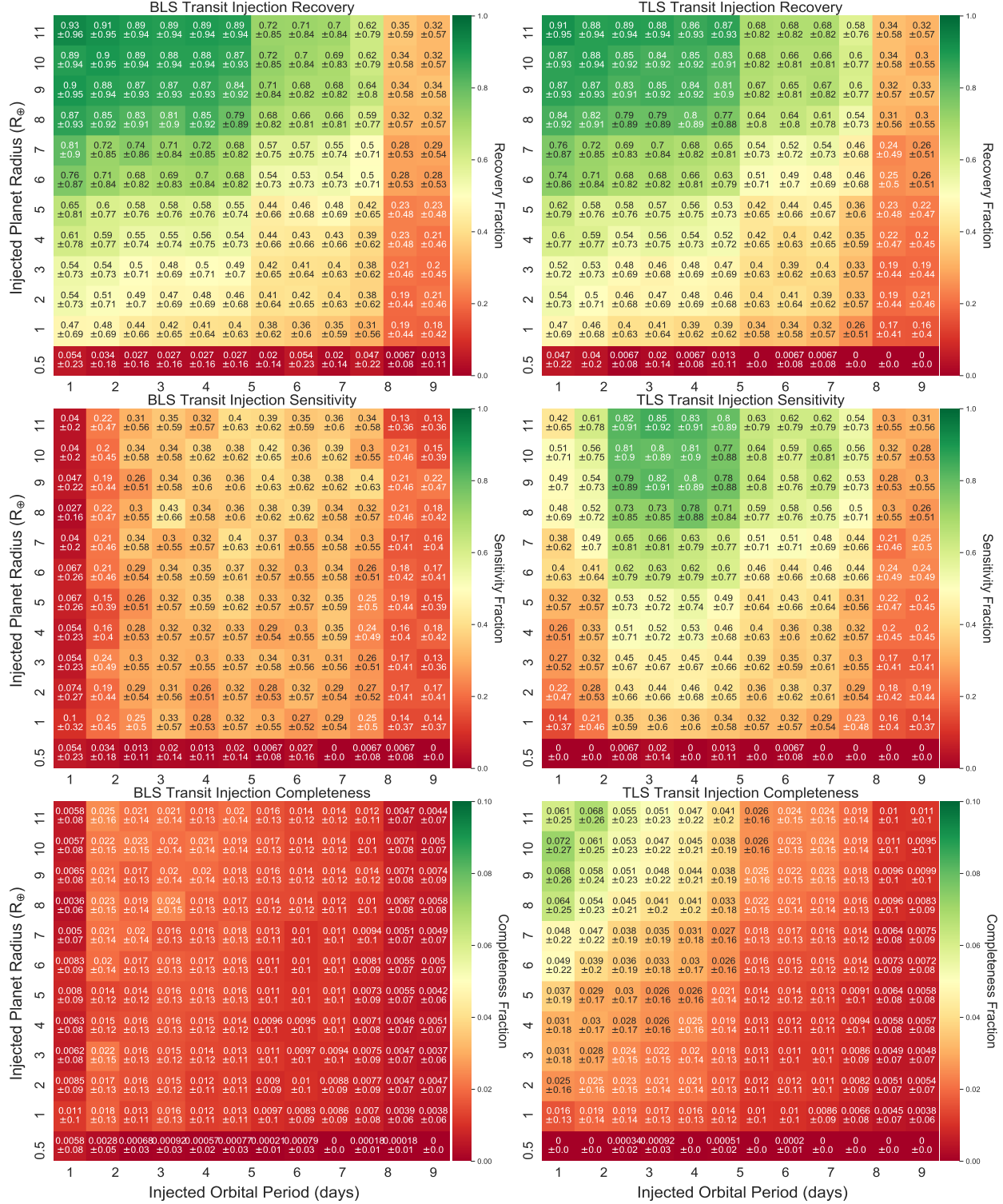
Figure 4.13: Transit injection analysis of 21,600 injected light curves across TESS sectors 1 – 5 as described in Section 4.5.3. *Top Row:* Fraction of detected injected transits from both BLS and TLS that meet our recovery criteria: recovered period within 1% of injected period. *Middle Row:* Fraction of detected injected transits from both BLS and TLS that meet our sensitivity criteria: recovered period is within 1% of injected period and injected radius is within recovered planet radius ± planet radius uncertainty. *Bottom Row:* BLS and TLS completeness maps that are results of the product of the detection sensitivity and the geometric transit probability as described in Section 4.5.3.2. The uncertainty of these 2D maps are Poisson counting errors for each cell of orbital period and planet radius.

104

4.5.3.2 Survey Completeness and Occurrence Rates for M-dwarf stars

Derivation for exoplanet occurrence rates requires the distribution of planet detections to be corrected for imperfect survey completeness. To account for detectable but not transiting planets, we compute the geometric transit probability for each star (n) at each orbital period and planet radius grid cell (i,j) in our 2D sensitivity maps as:

$$P_{transit}(n,i,j) = \frac{R_{star,n} + R_{Planet,j}}{\left(\frac{G\ M_{star,n}\ P_i^2}{4\pi^2}\right)^{1/3}} \tag{4.9}$$

The product of our 2D detection sensitivity maps with the geometric transit probability yields a 2D completeness map which can be seen in Figure 4.13. To estimate the occurrence rate of planets per star for our M-dwarf host stars, we choose to use the TLS 2D completeness map which is more complete due to the higher detection sensitivity. For the period-radius parameter space explored in our survey and the 5 TESS sectors searched, there are only a few dozen planet candidates that occupy a small region of the period-radius parameter space. Without a more diverse catalog of planet candidates that occupy more of the period-radius parameter space, making a meaningful 2D occurrence rate map is difficult. For this reason, we instead use an integrated occurrence rate to estimate, on average, how many planets per star there are for M-dwarf host stars.

By counting the number of times our planet candidates occur within our period and planet radius grid cells $N_{detected}(P,R_P)$, we can calculate the integrated occurrence rate $O(P,R_P)$ as a double integral over the period and planet radius space:

$$O(P,R_P) = \int\int \frac{N_{detected}(P,R_P)}{N_{stars} \times Completeness(P,R_P)}\ dPdR_P \tag{4.10}$$

For the full parameter space of $P \in [1, 9]$ days and $R_P \in [0.5, 11]$ $R_\oplus$, we calculate the integrated occurrence rates as 1.61 ± 1.27 planets per star. In the same range of periods with $R_P \in [0.5, 4]$ $R_\oplus$, we calculate the integrated occurrence rates as 1.45 ± 1.2 planets per star. If we also include all other confirmed planets, TOI and DIA planet candidates in the range $P \in [1, 9]$ days

and $R_P \in [0.5, 11]$ $R_\oplus$, we calculate the integrated occurrence rates as 2.49 ± 1.58 planets per star. In the same range of periods with $R_P \in [0.5, 4]$ $R_\oplus$, we calculate the integrated occurrence rates as 3.62 ± 1.9 planets per star. Other studies that have explored occurrence rates for M-dwarf host stars observed in the Kepler and K2 missions (Morton & Swift 2014, Dressing & Charbonneau 2015, Gaidos et al. 2016, Hardegree-Ullman et al. 2020, Cloutier & Menou 2020 and Hsu et al. 2020) have all found occurrence rates ranging in values from $\sim 1 - 2.5$ planets per star for periods < 200 days which are in agreement with our results. A more detailed comparison can be found in Section 4.6.3.

4.6 Discussion

4.6.1 Prospects for Mass Characterization via the Radial Velocity Method

One of the primary goals of the TESS mission is to discover at least 50 planets with radii $<$ 4 $R_\oplus$ and with measured masses via radial velocity follow up observations. Many of our planet candidates have radii less than 4 $R_\oplus$ (See Figure 4.9 and Table A3). In an effort to infer the expected radial velocity semi-amplitude of our planet candidates, we utilize the empirical mass-radius relation from Chen & Kipping 2016 to compute the planet masses for our planet candidates. We assume circular orbits (e=0, i=90°) to calculate the expected radial velocity semi-amplitude as:

$$K = \left(\frac{2\pi G}{\text{Period}} \right)^{1/3} \left(\frac{M_{\text{Planet}} \sin i}{M_{\text{Star}}^{2/3}} \right) \left(\frac{1}{\sqrt{1 - e^2}} \right) \tag{4.11}$$

The expected radial velocity semi-amplitude values are displayed in Table A4 and Figure 4.14. Some radial velocity spectrometers, such as ESPRESSO, NEID and EXPRES, are able to remain stable at the level of a few tens of cm/s. However, due to photon noise and stellar activity, radial velocities can be limited to maintaining accuracy of a few m/s (Fischer et al., 2016). All of our planet candidates have expected radial velocities ranging from 1.8 to 43.9 m/s, most of which are

above this sensitivity limit.

4.6.2 Prospects for Follow-Up Atmospheric Characterization

To further assist in providing an assessment for the suitability for follow-up atmospheric char-
acterization, we also calculate the Transmission Spectroscopy Metric (TSM) and Emission Spec-
troscopy Metric (ESM) as outlined in Equations 1 and 4 of Kempton et al. 2018. TSM is propor-
tional to the expected transmission spectroscopy signal to noise ratio and with the inferred planet
masses, is calculated as:

$$\text{TSM} = \text{C} \times \frac{\text{R}_{\text{planet}}^3 \text{T}_{\text{eq,planet}}}{\text{M}_{\text{planet}} \text{R}_{\text{star}}^2} \times 10^{-\text{J mag}/5} \tag{4.12}$$

Where C is defined as:

$$C = \begin{cases} 0.19, & \text{if } \text{R}_{\text{planet}} < 1.5\,\text{R}_\oplus \\ 1.26, & \text{if } 1.5\,\text{R}_\oplus < \text{R}_{\text{planet}} < 2.75\,\text{R}_\oplus \\ 1.28, & \text{if } 2.75\,\text{R}_\oplus < \text{R}_{\text{planet}} < 4\,\text{R}_\oplus \\ 1.15, & \text{if } 4\,\text{R}_\oplus < \text{R}_{\text{planet}} < 10\,\text{R}_\oplus \end{cases} \tag{4.13}$$

ESM is proportional to the expected S/N of a James Webb Space Telescope secondary eclipse
detection at mid-infrared wavelengths and is calculated as:

$$\text{ESM} = 4.29 \times 10^6 \times \frac{\text{B}_{7.5(\text{T}_{\text{day}})}}{\text{B}_{7.5(\text{T}_{\text{eff,star}})}} \times \frac{\text{R}_{\text{planet}}}{\text{R}_{\text{star}}}^2 \times 10^{-\text{K mag}/5} \tag{4.14}$$

where B is Plancks function evaluated for a given temperature at a representative wavelength
of 7.5 μm and T_{day} is the dayside temperature in Kelvin which we calculate as 1.1 times the

equilibrium temperature of the planet ($T_{eq,planet}$). Assuming albedo (A=0) and heat redistribution factor (f=1), we calculate $T_{eq,planet}$ as:

$$T_{eq,\,planet} = T_{eff}\sqrt{\frac{R_{star}}{a}}\left(\frac{1-A}{4f}\right)^{1/4} \tag{4.15}$$

Additionally, we also calculate the Signal-to-Noise Ratio (SNR) of our detected transit events as a function of the transit depth, photometric precision, number of transits, transit duration and cadence as:

$$SNR = \frac{\delta_{transit}}{\sigma_{CDPP}}\sqrt{\frac{N_{transits}\ T_{duration}}{cadence}} \tag{4.16}$$

The TSM, ESM and SNR values are displayed in Table A4 and Figure 4.14. For planet candidates with Signal to Noise ratios > 7, 23 of our new candidates have Transmission Spectroscopy Metrics > 38 and Emission Spectroscopy Metrics > 10 which make them promising targets for follow up characterization.

4.6.3   Comparison to Exoplanet Yield Estimates and Occurrence Rates

Previous studies by Sullivan et al. 2015, Barclay et al. 2018 and Ballard 2019 have predicted that the TESS mission will discover thousands of planets over the course of the two year mission. In terms of M-dwarf stars, Sullivan et al. 2015 predict about 1,700 transiting planets from about 200,000 stars observed with a 2 minute cadence, with about 419 planets with radii $> 2\,R_{\oplus}$ orbiting M-dwarfs. Barclay et al. 2018 predict that TESS will find 496 planets orbiting M-dwarfs, of which 371 orbit stars observed at 2-minute cadence. Ballard 2019 performed yield estimations focused on M-dwarfs with effective temperatures ranging from $3200 - 4000$ K and found that TESS will find about 1274 planets orbiting 1026 M-dwarf stars.
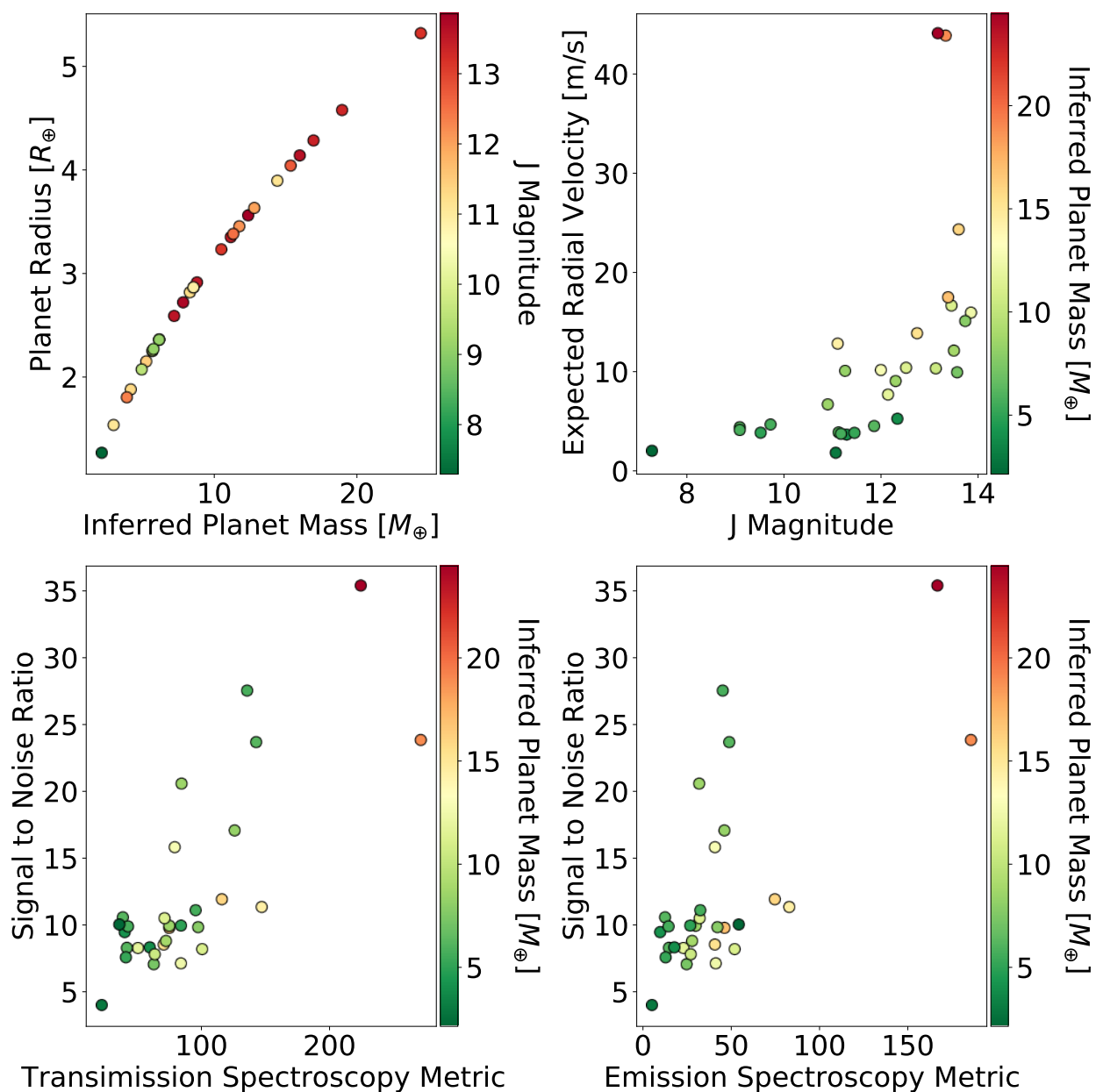
Figure 4.14: *Upper Left:* Using the planet mass-radius relations from Chen & Kipping 2016, we calculated the inferred planets masses for our planet candidates. *Upper Right:* Expected values of the radial velocity semi-amplitudes for our planet candidates as a function of J-band magnitude. *Lower Left and Right:* With the inferred planet masses, we calculate the Transmission and Emission Spectroscopy metrics introduced by Kempton et al. 2018 as functions of the Signal to Noise Ratio.

In this study, we found 33,054 nearby M-dwarf stars that fit in our selection criteria outlined in Section 4.2. Applying the selection cuts of $2300\,K < T_{eff} < 4000\,K$, $R_{Star} < 0.5\,R_{\odot}$, $M_{Star} < 0.5 M_{\odot}$ and $\log g > 3$ to the TESS Candidate Target List[20] (CTL Version 8), we find 138,962 M-dwarf stars within 100 pc and 1,562,038 M-dwarf stars total. Using the predicted number of M-dwarf TESS planets from Ballard 2019, the expected planet yield from sectors $1 - 5$ is 1,274 planets $\times$ 33,054 stars / 1,562,038 stars $\sim 27 \pm 5$ planets where the uncertainty is $\sqrt{N}$. Our yield of 29 planet candidates in TESS sectors $1 - 5$ matches very well with this predicted yield estimate. Propagating our rates of detection to the M-dwarf stars in the CTL, we expect to detect (29 planets / 33,054 stars) $\times$ 138,962 stars $\sim 122 \pm 11$ planets of nearby stars from FFI data for the two year TESS mission. If we extend our search to farther stars (> 100 pc) and assume similar rates of detection, we can expect to detect (29 planets / 33,054 stars) $\times$ 1,562,038 stars $\sim 1370 \pm 37$ planets total from FFI data for the two year TESS mission.

Various studies over the last few years have studied occurrence rates for M-dwarfs using confirmed planets and planet candidates from the NASA Kepler and K2 missions. Morton & Swift 2014 found an occurrence rate of Kepler M-dwarf planet hosts to be 2 ± 0.45 planets per star for P < 150 days and $R_P \in [0.5, 4]\,R_{\oplus}$. Gaidos et al. 2016 found an occurrence rate of 2.2 ± 0.3 planets per star for P $\in [0.5, 180]$ days and $R_P \in [1, 4]\,R_{\oplus}$. Dressing & Charbonneau 2015 found Kepler M-dwarf planet hosts to have an occurrence rate of 2.5 ± 0.2 planets per star for P < 200 days and $R_P \in [1, 4]\,R_{\oplus}$; for Earth-sized planets ($R_P \in [1, 1.5]\,R_{\oplus}$) and Super-Earths ($R_P \in [1.5, 2]\,R_{\oplus}$) in the ranges P < 50 days, the occurrence rate is 0.56 ± 0.06 and $0.46^{+0.07}_{-0.05}$ planets per star, respectively. Hardegree-Ullman et al. 2020 explored occurrence rates of Kepler M-dwarfs by spectral type and computed an occurrence rate of $1.19^{+0.70}_{-0.49}$ planets per star in the parameter space of P $\in [0.5, 10]$ days and $R_P \in [0.5, 2.5]\,R_{\oplus}$. Cloutier & Menou 2020 explored the parameter space in the ranges of P $\in [0.5, 100]$ days and $R_P \in [0.5, 4]\,R_{\oplus}$ and found occurrence rates for the Kepler and K2 missions in the ranges of 2.485 ± 0.32 and 2.26 ± 0.38 planets per star, respectively. Hsu et al. 2020 found occurrence rates of Kepler M-dwarf planet hosts to be 4.2 ± 0.6 or $8.2^{+1.2}_{-1.1}$, depending on their choice

---

[20] https://filtergraph.com/tess_ctl

of priors in sampling their distribution, for the ranges $P \in [0.5, 256]$ days and $R_P \in [0.5, 4]$ $R_\oplus$. Hsu et al. 2020 also found that for small planets at short periods in the range $P \in [2, 32]$ days and $R_P \in [1, 2.5]$ $R_\oplus$, their occurrence rate is $0.9^{+0.2}_{-0.1}$ or $1.6^{+0.3}_{-0.2}$ (depending on prior chosen).

As mentioned in Section 4.5.3.2, our integrated occurrence rate for the ranges $P \in [1, 9]$ days and $R_P \in [0.5, 11]$ $R_\oplus$ is 2.49 ± 1.58 planets per star when including known transiting planets, TOI and DIAmante planet candidates. This occurrence rate is within the uncertainty of the estimations of occurrence rates from previous studies in similar period-radius parameter space. Out of our 29 planet candidates, 24 of them have planet radii < 4 $R_\oplus$ with measurable planet masses (see Table A4) and can thus help aid to meet the Level 1 science requirement of the TESS mission[21].

4.6.4 Limitations of this Survey Strategy

Although there are more M-dwarfs observed by TESS with 30 minute cadences than 2 minute cadences, the lack of time resolution hinders the kinds of transits that can be detected. Using Equations 4.5 and 4.16, for a planet with a radius of 1 $R_\oplus$ transiting a small star with $M = 0.1$ $M_\odot$, $R = 0.1$ $R_\odot$ once per day, the transit duration is about 17 minutes with a SNR ~ 127 with a 2 minute cadence and a SNR ~ 33 with a 30 minute cadence. For a larger star ($M = 0.5$ $M_\odot$, $R = 0.5$ $R_\odot$) and the same transiting planet, the transit duration is about 47 minutes with a SNR about 8 with a 2 minute cadence and a SNR about 2 with a 30 minute cadence.

With enough coverage of observed transit events, it is possible to detect these short duration, small transit events in FFI data but with the various instrumental systematics and astrophysical noise that each of these faint targets present, these $1 - 2$ data points per transit may be removed in processing of the data through common data reduction practices like smoothing or outlier removal. With our single sector approach of searching for transit events, the types of transits we can detect

---

[21] https://tess.mit.edu/followup/

with the 30 minute cadence data is somewhat limited as shown in Figure 4.13 where we maintain a detection sensitivity of roughly 30% for radii larger than 1 $R_\oplus$. In Years 3 and 4 of the TESS extended mission, the FFIs will be observed with a 10 minute cadence which will certainly help detection of these types of transit events become easier as they will likely have higher SNRs due to the improved time resolution.

Another challenge encountered in this survey is making sure our automatically selected apertures stayed on target throughout observations in each sector of data. As mentioned in Section 4.3.2, we utilized a bivariate quadratic function to approximate the core of a Point Spread Function for each FFI cutout where we chose pixels that were brighter than 7.5 standard deviations above the median brightness of the time series. For isolated targets, this works fairly well but for crowded fields, especially for dim targets (TESS magnitude > 15), our centroiding procedure often fails and the selected aperture centers on other bright stars in the 11×11 pixel cutouts.

4.6.5   Future Work

Early in the testing phase of our pipeline's application, we noticed that each sector of TESS data has varying amounts of instrumental effects due to telescope jitter or glare in the TESS field of view from Earth and/or the Moon near the beginning or ends of data collection in each orbit of the satellite. For this reason, we opted to focus on performing transit searches on individual sectors which limited the upper limit to the longest periods we can search per sector to about 9 days. This choice was cautiously selected early in the development of our pipeline to avoid increasing the amount of false positives we may have encountered with a multi-sector approach that could possibly be attributed to residual instrumental effects in our processed light curves.

We intend to continue our survey for TESS sectors 6 – 13 in the southern hemisphere and 14 – 26 in the northern sectors in order to gain a longer baseline of coverage for our M-dwarf target

lists so we can extend the range of periods to search for transits with a multi-sector approach. With a longer baseline of observations, we can also consider searching for multiple planets per target with higher confidence than in our single sector approach by analyzing other peaks in the TLS power spectrum with strong SDEs (see Appendix D, TOI-270). We also intend to vet our threshold crossing events that have lower Signal Detection Efficiencies in the range of $6 - 10$ in order to potentially find transit detections that may have been missed by using a higher threshold.

Although we were careful in our promotion of planet candidates from TCEs, there is still the element of human judgement and the potential for bias. As a quick check and alternative analysis to our vetting report, we used the automated EDI-Vetter Unplugged tool which uses our TLS outputs to conduct false positive tests as described in Section 4.4.2. Some other community tools like TESS-ExoClass (TEC[22]) or Discovery and Vetting of Exoplanets (DAVE, Kostov et al. 2019b) are vetting tools that were built upon the Kepler vetting algorithm RoboVetter (Coughlin et al., 2016), and were developed for use in K2 (Hedges et al., 2019) and TESS data (Crossfield et al. 2019, Kostov et al. 2019a). For our future endeavors, to minimize opportunities of human selection bias and reduce the overall human vetting time, we may explore automating our vetting process or use tools like DAVE or TEC as the first round of vetting in our overall vetting process.

In future work, we may revisit our centroiding process or employ a multi-aperture approach similar to what is used in other FFI pipelines (Feinstein et al. 2019; Nardiello et al. 2019; Bouma et al. 2019; Montalto et al. 2020). We currently keep track of the change in pixel directions during any detected transit-like events and exclude threshold crossing events that have a change in pixel direction more than 5 standard deviations to help reduce the amount of false positive detections but an alternative approach to centroiding may prove more consistent for targets fainter than TESS Magnitude > 15.

---

[22] https://github.com/christopherburke/TESS-ExoClass

All of these candidates were observed by TESS roughly two years ago and the southern hemisphere has already started being observed by TESS again in Year 3 of its extended mission. In the extended TESS mission, Full Frame Images will have an improved time resolution of 10 minute cadences whereas in the Years 1 and 2 the time resolution was 30 minutes. After working through the Year 1 and 2 data, we also intend extract light curves from Year 3 data to revisit these candidates with the improved time resolution. With a longer baseline from analyzing the FFI data from the TESS mission and its extended mission, we also intend to revisit our detection recoverability, sensitivity and survey completeness of the NEMESIS pipeline for longer orbital periods. With more future planet candidate detections, we can also revisit our estimation of planet occurrence rates for M-dwarf host stars with more resolution in the orbital period-planet radius domain.

4.7   Conclusion

In this work, we have developed a new pipeline called NEMESIS to extract photometry from the TESS Full Frame Images, remove instrumental systematics, long term stellar variations and conduct transit searches. We applied the NEMESIS pipeline to 33,054 M-dwarfs located within 100 parsecs and were observed by TESS in sectors 1 – 5. We then presented our transit search approach and discussed the overall transit detection recoverability, sensitivity and completeness of our pipeline with a transit injection analysis. Our methods have proved successful with the production of 183 threshold crossing events with Signal Detection Efficiencies greater than 10.

Of those 183 candidates, 29 were voted as planet candidates through our vetting process; 24 of which are new detections and are now listed as Community TESS Objects of Interest (CTOIs)[23]. Our planet candidates have orbital periods ranging from 1.25 – 6.84 d and planet radii from 1.26 – 5.31 $R_\oplus$. We then discussed the context of these planet candidates in regards to the radius valley for M-dwarf stars and find that many of our candidates exist near this planet radius-period domain.

---

[23] https://exofop.ipac.caltech.edu/tess/view_ctoi.php

With the addition of our new planet candidate detections along with previous detections observed in sectors $1 - 5$, we calculate an integrated occurrence rate of 2.49 ± 1.58 planets per star for the period range $\in [1,9]$ days and planet radius range $\in [0.5,11]$ $R_{\oplus}$. We project an estimated yield of 122 ± 11 transit detections of nearby M-dwarfs for the two year TESS mission. 23 of our new candidates have Signal to Noise ratios > 7, Transmission Spectroscopy Metrics > 38 and Emission Spectroscopy Metrics > 10 which make them promising targets for follow up characterization.

As shown in this work, our pipeline is able to produce transit detections for M-dwarf stars with 30 minute cadence light curves and provides a sample of hidden gems that are still left to find in FFI data of other sectors observed by TESS. The results of this work is also a testament to the high quality of the Full Frame Images and invokes a sense of excitement for what other worlds may lay hidden within the data.

All of our data products for our planet candidates will be released through the Filtergraph visualization portal at https://filtergraph.com/NEMESIS.

Chapter 5

Future Directions and Summary

5.1 Ongoing and Future Work

During my PhD, I led a collaborative effort to search for transits of 33,054 nearby M-dwarf stars located within 100 parsecs that were observed in TESS sectors 1–5. In Feliz et al. 2021 (Chapter 4), we created a custom Python pipeline called NEMESIS, which is designed to extract instrumental systematics corrected high-quality light curves from the TESS Full Frame Images (FFIs) and conduct a blind transit survey for short period planets (< 9 days). In this work, we detected 183 strong transit-like events and after several rounds of group vetting and additional analyses, we identified 24 planet candidates that were not announced by the TESS mission and are now listed as Community TESS Objects of Interest (TOIs, Guerrero et al. 2021). As of March 2022, there are 5,243 TOIs[13], of which 217 are planet candidates transiting nearby M-dwarf host stars (logg > 3, $T_{eff} < 4000$ K, $R_{star} < 0.5$ $R_\odot$, $M_{star} < 0.5$ $M_\odot$, d < 100 pc) and out of 3,811 confirmed transiting exoplanets[1], 113 are planets with measured masses that orbit nearby M-dwarf host stars. When this sub-sample is compared to the total exoplanet population of 4,935 planets[1], combined with the fact that M-dwarfs are the most abundant type of star in our galaxy, it is clear that there is much to be learned about the population and diversity of M-dwarf hosted exoplanetary systems.

5.1.1 Understanding the Radius Valley around Low Mass Stars

In Figure 5.1, the radius-period slope that marks the location of the radius valley for Sun-like stars (Martinez et al., 2019) is shown as a horizontal solid black line and for Sun-like stars, the radius valley is thought to be dominated by thermally-driven atmospheric mass loss for short period planets as Sun-like stars typically have higher absolute extreme Ultraviolet luminosities than their M-dwarf counterparts. The radius-period slope that marks the location of the radius valley for low mass stars (Cloutier & Menou, 2020) is shown as a horizontal dashed-line and for low mass stars, is thought to be dominated by the late formation of terrestrial planets in a gas poor environment. These distinct slope predictions naturally carve out a subspace in radius-period space wherein knowledge of planetary bulk compositions can directly constrain the applicability of each class of model. However, there are comparatively few discovered and characterized M-dwarfs planet systems, and we need more to study the gap robustly. Therefore, populating this subspace with more planets with known bulk compositions will inform the prevalence of each model as a function of host stellar mass.
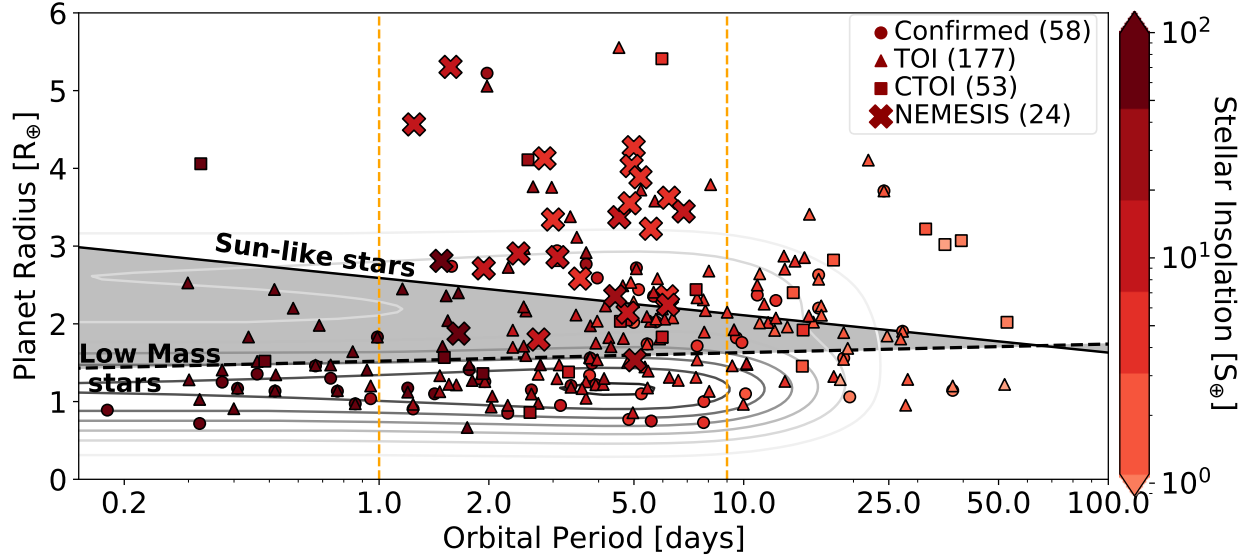
Figure 5.1: Similarly to Figure 4.9, this Period-Radius diagram displays the parameter space occupied by all nearby (< 100 parsecs) confirmed transiting exoplanets and exoplanet candidates that eclipse nearby M-dwarfs according to the selection criteria outlined in Section 4.2. Confirmed transiting planets (◯) were queried from the Exoplanet Archive[1] and the TOI planet candidates (△s) were queried from the TOI catalog[13] (March 1st, 2022). Planet candidates that were contributed by the TESS community are queried from the Community TESS Object of Interest (CTOI, □s) catalog[23]. NEMESIS planet candidates produced in this work are marked with ✖s. The vertical dashed orange lines represent the range of periods searched by our survey. All points are colored by their respective incident stellar flux (in Earth units), calculated with Equation 4.7. For comparison, over plotted are the approximate period-dependent radius valley slope of Sun-like stars from the CKS (solid black line, Martinez et al. 2019, M19) and the approximate period-dependent radius valley slope of low mass stars (dashed solid line, Cloutier & Menou 2020, CM20). The shaded region highlights the parameter space between the two model estimations of the radius valley from M19 and CM20. Regions above and below these slopes are inferred to be rocky (R) or non-rocky (NR) type planets. The contour lines are the Kernel Density Estimation of the period-radius space for all planet hosting M-dwarf systems from the Exoplanet Archive.

I will build upon my PhD work to produce high quality light curves and conduct transit searches for TESS sectors 1–26, increasing my initial target list from 33,054 stars to 191,244 stars located within 100 parsecs from the Sun, as shown in Figure 5.2. This transit survey will yield a catalog of planet candidates some of which will be suitable for spectroscopic follow-up with current technology and will lead to a catalog of confirmed planets. With this catalog of confirmed planets from the transit and spectroscopy surveys, I will reanalyze the exoplanet demographics of M-dwarf planet systems and help identify the primary planet formation pathways that sculpt the radius valley.
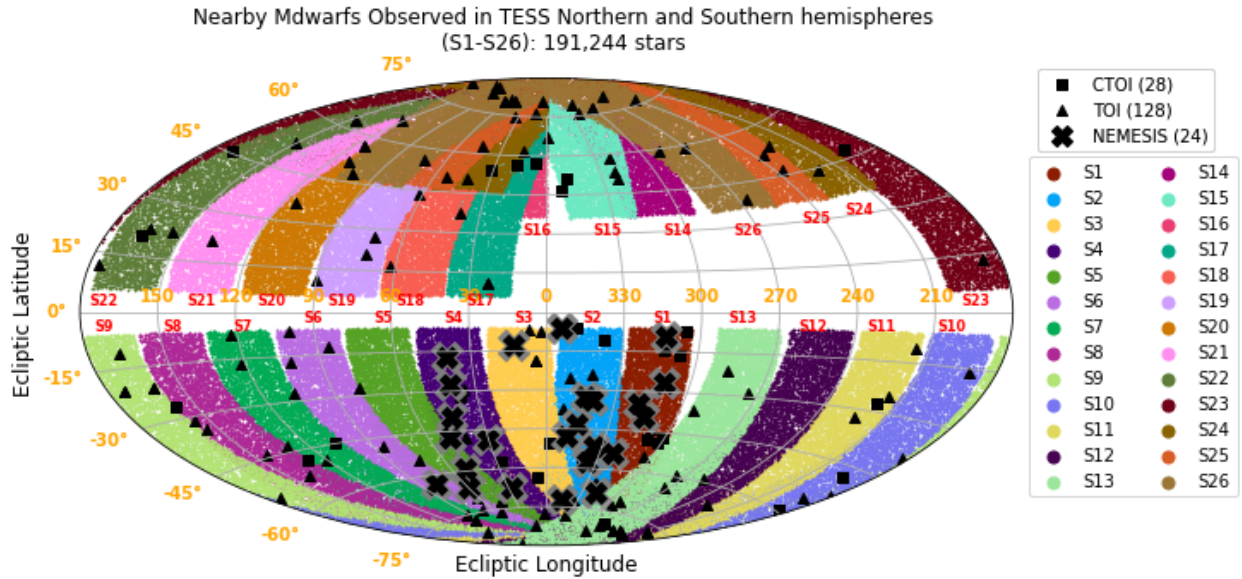
Figure 5.2: Coordinates of all M-dwarfs observed by TESS in sectors 1–26 within 100 parsecs. M-dwarfs were filtered using the selection criteria outlined in Section 4.2. This target list is displayed in ecliptic coordinates as a Mollweide projection. Community TESS Objects of Interest (CTOIs) are marked as □s, TESS Objects of Interest (TOIs) are marked as △s and NEMESIS planet candidates are marked as ✖s.

5.1.2 Determining the Empirical TESS FFI Planet Occurrence Rate for M-dwarfs

In Feliz et al. 2021, we explored the detection sensitivity of the NEMESIS pipeline and from our survey completeness, we were able to calculate an integrated occurrence rate of 2.49 ± 1.58 planets per M-dwarf star for orbital periods between 0.5–9 days and planet radii 0.5–11 Earth radii. Since every sector of TESS data has unique systematics, the detection sensitivity of the NEMESIS pipeline will be have to reevaluated with light curves from the full primary mission in order to get more a more robust estimation of the empirical FFI planet occurrence rate. As many M-dwarfs are faint and are not observed with a 2 minute cadence by TESS, FFI transit surveys can give an empirical validation of how many planets are missed by using the 30 minute cadence data of the primary mission. In Feliz et al. 2021, we projected an estimated yield of 122 ± 11 transit detections for the prime TESS mission based on the detection sensitivity of the NEMESIS pipeline and the 138,962 M-dwarfs in the TESS Candidate Target List (Stassun et al., 2018). Our proposed target list is

larger than the CTL and based on the 191,244 target stars and our transit detection rate, I project that I will detect 168 $\pm$ 13 transiting M-dwarf planet candidates from the prime TESS mission. This estimated yield is slightly less than the 261 $\pm$ 38 transiting planet candidates predicted by Kunimoto et al. 2022 which incorporates both 30-minute and 2-minute cadences in its estimation for exoplanet yield (Table 4) from the prime TESS mission (years 1–2). I will also conduct a multi-sector transit search to search for transiting exoplanet candidates with orbital periods > 9 days that may potentially orbit in their host stars habitable zone.

To explore the detection sensitivity of the NEMESIS pipeline across sectors 1–26, I will follow stars that best represent the photometric precision of all the extracted NEMESIS light curves, I will inject tens of thousands of simulated transit models into the raw unprocessed light curves and use the NEMESIS pipeline to process and recover the injected signals in terms of planet radius and orbital period. This will produce a two dimensional map of detection sensitivity as functions of planet radius and orbital period, similar to Figure 4.13. In Feliz et al. 2021, we explored the detection sensitivity for periods < 9 days to allow at least 3 transits to be detected in a 27 day window of observations (the typical length of TESS observations in a given sector). Having access to multi-sector observations of target stars also allows the exploration of detection sensitivity to injected transits at longer periods. The estimation of detection sensitivity of the NEMESIS pipeline is crucial to estimating the FFI planet occurrence rate. The NEMESIS light curves produced in this all-sky transit survey have the potential to contribute to dozens of publications by other groups on exoplanet and other astrophysical phenomena (such as M-dwarf eclipsing binaries, flare rates or rotation periods) and I intend to release them as a public High Level Science Product on MAST[24]. Currently, the NEMESIS planet candidates are listed as CTOIs on ExoFOP[23]. I also intend to publicly release the NEMESIS pipeline as open source software written in the Python programming language that will be pip installable. The work of this project will result in a follow-up publication to the initial NEMESIS study. With a larger catalog of M-dwarf planet candidates detected from this FFI transit survey using my NEMESIS pipeline, I will estimate a more robust occurrence rate

---

[24] https://archive.stsci.edu/hlsp/

of planets per M-dwarf star for larger bins of orbital periods and planet radii.

5.1.3 Spectroscopic Survey and Characterization of M-dwarf Planet Candidates

From the larger catalog of transiting exoplanet candidates that I will produce from the TESS prime mission, I will then identify which candidates are most suitable for follow-up observations for confirmation of the planet candidates presence. To do so, I propose conducting a large spectroscopic survey of stars that show evidence of hosting transiting planet candidates with Signal-to-Noise Ratios > 7. I will submit observing proposals for facilities like the Habitable zone Planet Finder, NEID, MAROON-X, TRES, MINERVA, Carnegie Planet Finder Spectrograph and/or HARPS-N spectrographs. All of these resources are fully capable of obtaining precise radial velocity measurements that will help measure masses for these planet candidates; thus filling in the planet population for M-dwarf stars in the process and illustrating the underlying mechanisms for planet formation. Many of these facilities have their own in-house data reduction pipelines (such as SERVAL; Zechmeister et al. 2018) to obtain radial velocities from the observed spectra and through Python packages like Juliet (Espinoza et al., 2019) or EXOFAST (Eastman et al., 2019) to create joint models of photometric and spectroscopic data. Additionally, the Las Cumbres Observatory telescopes and other resources available through the TESS Follow-up Observing Program will be particularly useful for obtaining ground-based follow-up photometry of planet candidates. For particularly interesting systems that I will find, such as those that have orbital periods in the habitable zones of their host stars, this work will result in several individual planet discovery publications. With tightly constrained planet masses and radii, I will then calculate estimations of their bulk compositions to help answer this question of whether the transition between rocky and non-rocky type planets arises from processes like thermally-driven atmospheric mass loss or if it is the natural by-product of processes like rocky planet formation in a gas-poor environment.

For each star system that I obtain measured planet masses for, I will compare predictions of different mass loss models to identify the primary planet formation pathway in M-dwarf stars as a function of stellar mass. Cloutier & Menou 2020 estimate that TESS observations of ∼85,000 mid-to-late M-dwarfs are required to distinguish between model predictions of photoevaporation and core-powered mass loss or gas-poor formation at 3σ for stars observed with 2-minute cadences. The NEMESIS pipeline has already demonstrated its ability to detect planet candidates near the estimated radius valley around low-mass stars (see Figure 4.9). For the target list of 191,244 stars observed by TESS with 30-minute cadences, I expect to further constrain the central location of the radius valley of M-dwarf host stars. This will then allow me to test different physical models of photoevaporation, core-powered mass loss, and gas-poor formation as functions of stellar mass to identify the primary planet formation pathway of M-dwarf star systems. The work I will carry out on this large sample analysis of nearby M-dwarf stars will open new doors in exoplanet population demographic studies, allowing further insight into the diversity of this category of planet systems and help to uncover the dominant planet formation pathways that sculpt the radius valley around M-dwarfs.

5.1.4   Measuring M-dwarf Rotational Periods and Flare Rates with NEMESIS Light Curves

From the results of Project 1, there will be a large sample of photometric observations of nearby M-dwarf stars that can be used to assess the distribution of stellar rotation periods. Understanding the rotation periods of stars that may host planets is important because the rotation signal can be spotted in both photometric and spectroscopic observations which can make planet detection and confirmation challenging. Additionally, for early M dwarfs, the typical rotation periods for older field stars coincides with orbital periods of planets in the habitable zone (Newton et al. 2016a; Vanderburg et al. 2016). In previous studies of M-dwarfs observed in Kepler/K2 data (Newton et al., 2016a), there is a bimodality in the distribution of rotational periods ∼10 days that splits

the stellar population into fast rotators ($P_{Rot} < 10$ days) and slow rotators ($P_{Rot} > 10$ days). In past studies, the use of gyrochronology models based on rotation periods of stars has proven as a effective method to obtain Bayesian estimation of stellar age (Angus et al. 2018, Angus et al. 2019). Through use of time series analysis techniques like Lomb-Scargle Periodograms, Auto-correlation functions or Quasi-Periodic Gaussian Processes modeling, it is possible to detect and measure periodic or quasi-periodic events in light curves that can be attributed to stellar rotation. By increasing the population of M-dwarfs with measured photometric rotation periods that have a range of masses on both sides of the fast/slow rotator regime, I can begin to further constrain the age at which M-dwarfs begin to transition from fast to slow rotators, a long-standing question in astrophysics.

Previous studies based on the Hα and Ca II emission lines as well as the coronal X-ray emission found that the stellar activity has a close relation with rotational period (Reiners, 2012). For active stars, flares are very common and can be identified in photometric data, and their statistical properties are a good proxy for stellar activity. Hawley et al. 2014 found that the occurrence rate of numbers of flares per flare energy bin satisfied a power-law relation, dN/dE $\sim$ 2 using five M dwarfs and reported the strong correlation between flare energy, amplitude, duration, and decay time. As a member of the ESA PLATO (Rauer et al., 2014) Flares Working Group, I have constructed a flare detection pipeline based on the FINDFLARE algorithm (Chang et al., 2015) and an empirical flare template (Davenport et al., 2016) that was tested on several G and M type flare stars in Kepler/K2, TESS and simulated PLATO light curves. This flare detection and modeling pipeline will be useful for the determination of each target star's flare rate. By further constraining this power law relation along with rotational periods (and thus gyrochronology ages) of M-dwarfs, this work can help pinpoint which M-dwarf systems are relatively quiet in terms of stellar activity and may make suitable planet hosts for planets that orbit in their respective habitable zones as stars that are very active and flare often may vaporize the atmospheres of close in planets through processes like photoevaporation. My results on the frequency of flares will provide useful constraints

for exoplanet atmospheres and habitability models.

5.2 Summary

M-dwarf stars are plentiful in the Milky Way and are favorable stars to search for orbiting planets when employing the transit method. However, due to their intrinsic faintness, stellar activity and low geometric transit probabilities, they can prove challenging to study. For example, Proxima Centauri, the nearest M-dwarf which flares on average $\sim$63 times per day (Davenport et al., 2016), also hosts an exoplanet with a minimum mass of $\sim$1.3 M$_\oplus$ (Anglada-Escudé et al., 2016) and has a geometric transit probability of 1.5% (See Section 3.2.2) due to having an orbit that may not be in our line of sight. This was the case in Sections 2 and 3 where transits of Proxima Centauri b were not detected despite having ground-based photometry spanning 11 years and efforts by many other teams of researchers, such as Gilbert et al. 2021 who found no evidence of transits in TESS data in the period range of $\sim$1–30 days. The TESS mission which was designed to conduct an all-sky survey provides the best current opportunity to search for transits of M-dwarf stars. With the experience of searching for transits of Proxima Centauri b, we were able to produce the NEMESIS software which is capable of producing high quality TESS light curves that are optimized for transit searches of M-dwarf stars. From this work, 183 target stars produced transit-like features and after rounds of vetting through visual inspection, 24 of them were voted as being new planet candidates that were previously undetected by the TESS mission.

The results of this project provide a framework for conducting all-sky transit surveys from the prime TESS mission and can potentially produce a yield of hundreds of planet candidates that transit nearby M-dwarf host stars. As the field of exoplanetary science continues to move toward an era of big data, there continues to be opportunities for new scientific results to be discovered on scales that were previously impractical. As TESS continues to observe in its extended mission,

there is plenty of work to be done to understand the strengths, weaknesses and limitations for the various TESS photometry and transit survey pipelines that exist. By thoroughly understanding the transit detection capabilities of TESS pipelines like SPOC, QLP or NEMESIS, much like how it was done for the Kepler mission (Christiansen et al., 2015), the assessment of planet occurrence rates can be computed more accurately. Conducting these large transit and spectroscopic surveys can get us closer to answering the question of where nearby Earth-like planets may exist in these nearby M-dwarf stars and by studying the diversity of those planets, we may learn what habitability looks like around M-dwarfs and how it may be different from our own Solar System.

Chapter 6

Appendix

A   Full Light Curve Data of Proxima Centauri

In Figure A1 we present all 85 of our new Proxima light curves, along with the literature light curves, that contribute within $\pm 2\sigma$ of the K2017 RV-based ephemeris. The figure is best viewed electronically due to its large format. All light curves are folded on the K2017 RV-based ephemeris and shifted relative to each other on the vertical axis for clarity. The "20060605 RAE" light curve from Figure 2.8 does not fall within the phase range covered by Figure A1. If we extended our x-axis, this light curve would appear at ~ -1.5 days from K2017 RV-based ephemeris.

The grey vertical bars at $\sim \pm 1.2$ days indicate the extents of the 2σ uncertainty, which is altogether ~ 2.5 days, but varies depending on the amount of time since the reference epoch, T_0, due to the cumulative uncertainty in the period. Also shown are the transit centers at each displayed epoch, extracted from other literature ephemerides listed in Table 2.1, after phasing to the K2017 RV-based ephemeris. The transit centers predicted by the A2016 RV-based ephemeris are displayed as blue vertical lines. The transit centers predicted by the D2017 ephemeris are displayed as magenta vertical solid lines. The K2017 Signal C and L2017 ephemerides are shown as black and light blue vertical bars, respectively.

127

Each light curve is binned at 5 minute intervals. The data from this work are displayed as dark and light grey dots for alternate light curves for clarity when overlapping. The MOST data are displayed as black dots, and the BSST data are displayed as light blue dots. The L2017 transit models are displayed as black and green solid lines for the MOST and BSST events, respectively.

The K2017 Model $\mathcal{M}_1$ ephemeris does not overlap within $\pm 2\sigma$ of the K2017 RV-based ephemeris. In Figure A2 we present our 10 light curves that contribute within ± 3 hours of the K2017 Model $\mathcal{M}_1$ ephemeris. Each light curve is binned at 5 minute intervals. The light curves from this work are displayed as grey dots. The MOST data are displayed as black dots. The $\mathcal{M}_1$ transit models are over-plotted as black solid lines on the MOST light curves.

All of our light curve data will be provided in machine readable format as part of Paper II.
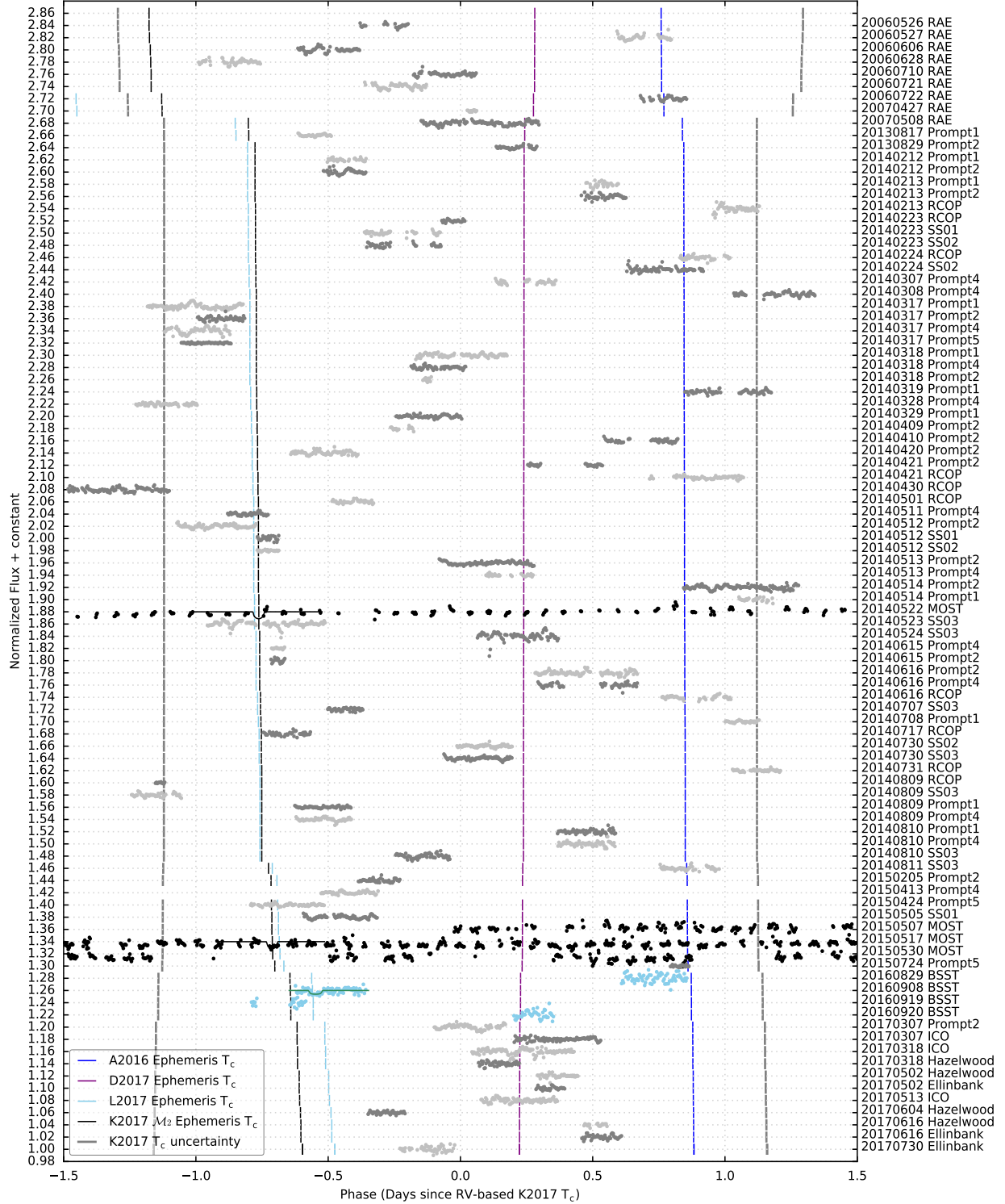
Figure A1: The full set of 85 light curves, along with the literature light curves, that contribute within $\pm 2\sigma$ of the K2017 RV-based ephemeris. The grey vertical bars at $\sim \pm 1.2$ day mark the extents of the 2σ uncertainty. Each light curve is binned at 5 minute intervals. The data from this work are displayed as dark and light grey dots for alternate light curves for clarity when overlapping. The MOST data are displayed as black dots, and the BSST data are displayed as light blue dots. The K2017 $\mathscr{M}_2$ and L2017 transit models are displayed as black and green solid lines for the MOST and BSST events, respectively. The transit centers predicted by the A2016 RV-based, D2017, K2017 Signal C, and L2017 ephemerides are shown as blue, magenta, black, and light blue vertical bars, respectively.

129
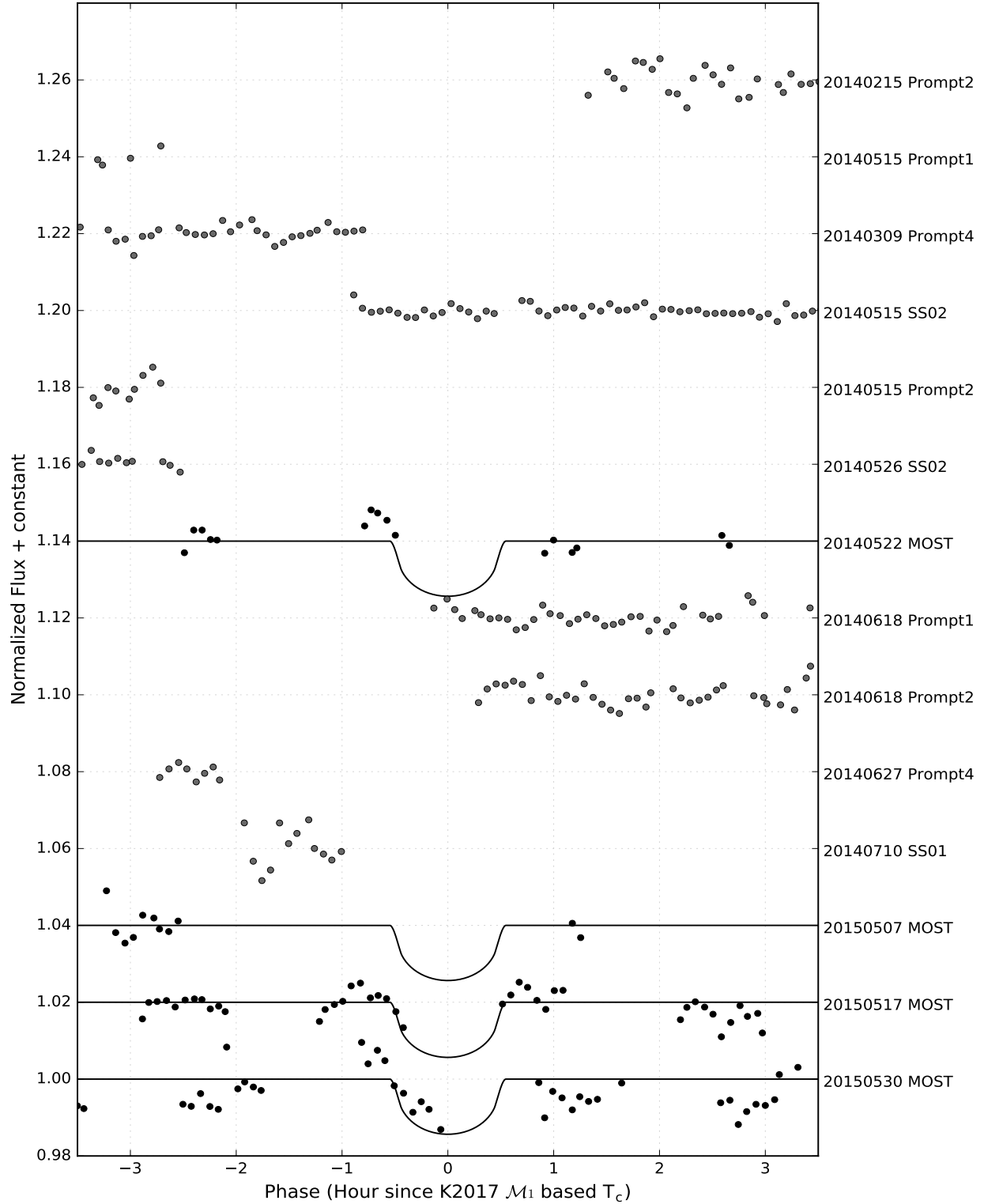
Figure A2: The full set of 10 light curves that contribute within ±3 hours of the K2017 Model $\mathcal{M}_1$ ephemeris. The light curves from this work are shown as grey dots. The MOST data are shown as black dots. The K2017 $\mathcal{M}_1$ transit models are over-plotted as black solid lines on the MOST light curves.

B Exploration of the 1.808 day Signal and Photometry of 262 Light Curves of Proxima Centauri

To verify whether or not the top peak of the BLS power spectrum is due to a transit-like event, we phase folded our 262 light curves around the orbital period corresponding to the top peak which is ~ 1.808 days. We then examined a subset of 32 light curves that contribute data points to within ± 3 hours of the transit center time reported by the BLS algorithm, $T_C \sim = 2453880.516604$ BJD$_{\text{TDB}}$. In Figure A3, the individual light curves are then binned with 5 minute bins and are vertically offset from one another. In Figure 11 of Paper I, we modeled the best fit transit model of the Skynet Prompt 2 UT 2014 May 14 light curve where we deemed it unlikely to be caused by a transiting exoplanet. The Skynet RCOP light curve from UT 2014 August 2 has a decrease in flux near phase 0 relative to T_C but this is due to the remaining points after our iterative 3-σ cut of a flare event that is followed by another smaller pair of flare events. The KELT-FUN Ivan Curtis Observatory light curves from UT 2017 March 7 and UT 2017 March 18 display decreases in flux near phase 0 in relation to T_C. In the UT 2017 March 7 light curve, the decrease at the end of the light curve are suspected to be due to atmospheric fluctuation but remained in our quality checks in Paper I. The UT March 18 2017 has a relatively high amount of scatter compared to the rest of our data but also passed our quality check due to the transit-like feature shown. In Figure 3.5, we highlighted data from the UT April 11 2007 RAE light curve which displays a ~ 20 mmag dip which we've chosen to include in our ensemble of light curves. We conclude that the that top peak of the BLS power spectrum shown in Figure 3.3 is unlikely to be due to a transiting exoplanet as there is no consistent transit events in all other light curves near orbital phase 0 relative to T_C.
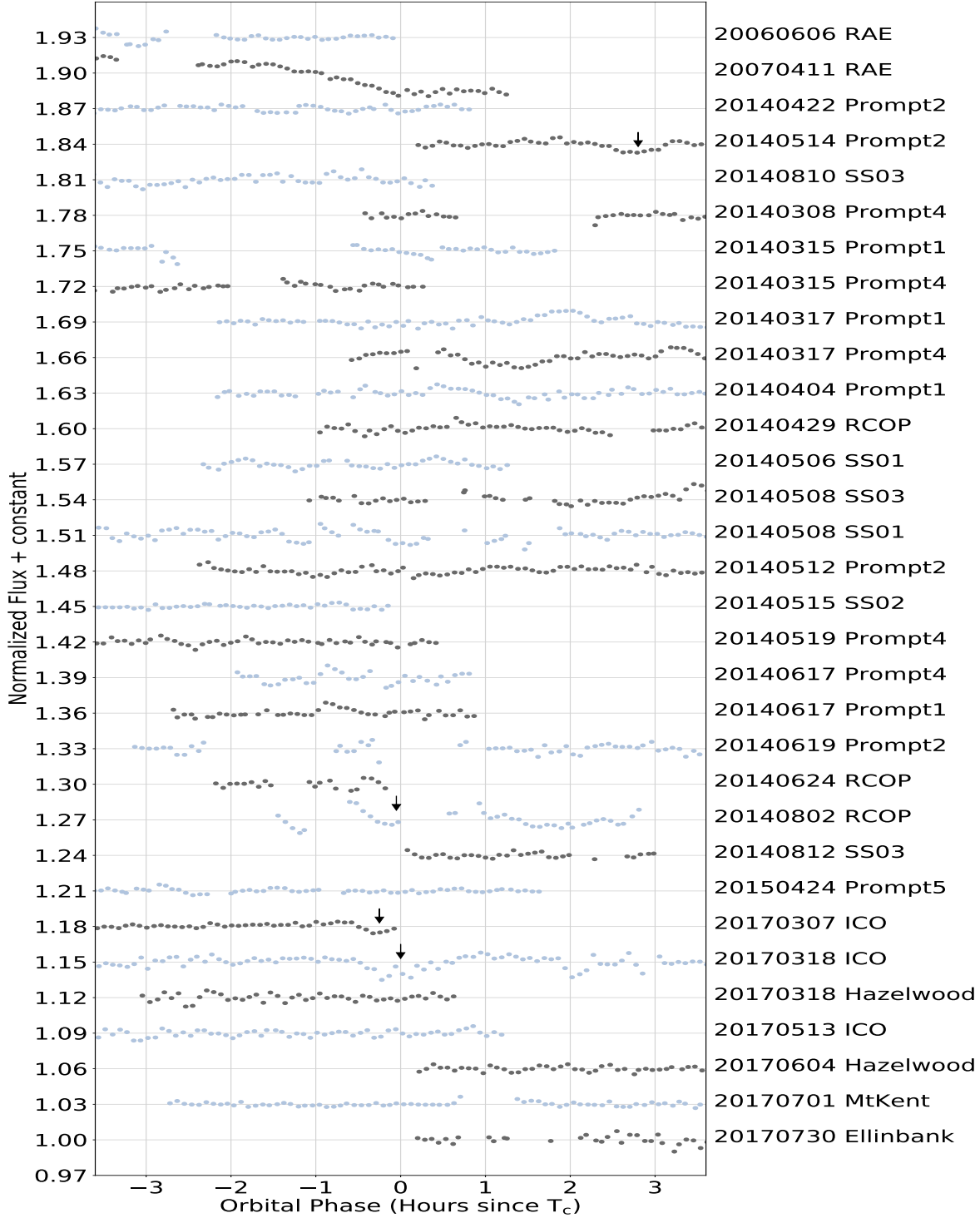
Figure A3: These detrended light curves correspond to the contributions in phase of Figure 3.3. Each light curve is phase folded around the orbital period and transit center time from the highest peak from the VARTOOLS BLS algorithm. The orbital period for this peak is 1.808 days and has a transit depth of 5.28 mmag. We vertically separated each light curves by a constant and alternated their colors for easier distinction between observation. Each light curve is binned at 5 minute intervals and contributes at least one data point within ±1 hour of the transit center time. We discuss the light curves highlighted by arrows in more detail in the Appendix section.

132

Table A1: Photometry of Proxima Centauri

BJD$_{\text{TDB}}$	Normalized Relative Flux	Uncertainty
2453879.916949	1.03734	0.00461
2453879.917331	1.02921	0.00439
2453879.917713	1.02177	0.00427
2453879.918095	1.01875	0.00410
2453879.918477	1.01907	0.00405
2453879.918870	1.01457	0.00392
⋮	⋮	⋮
2457965.105301	1.028180	0.004330
2457965.108993	1.032670	0.003000
2457965.109398	1.002570	0.004370
2457965.109838	1.038580	0.004730
2457965.110706	1.018970	0.003880
2457965.111134	1.035270	0.003390

This table contains photometry of the 262 combined light curves used in Blank et al. 2018 and this work. This data set is undetrended and iteratively 3-sigma clipped. The time stamps are the barycentric julian date in the barycentric dynamical time of observation (BJD$_{\text{TDB}}$). The data in its entirety is in the electronic version of *The Astrophysical Journal*. A portion is shown here for guidance regarding its form and content.

Table A2: Detrended Photometry of Proxima Centauri

BJD$_{\text{TDB}}$	Normalized Relative Flux	Uncertainty
2453879.928989	1.005052	0.003787
2453879.929371	1.010987	0.003808
2453879.929764	1.010987	0.003740
2453879.930135	1.007096	0.003693
2453879.930517	1.002253	0.003618
2453879.930899	0.990985	0.003557
⋮	⋮	⋮
2457965.104885	1.008081	0.004403
2457965.105301	1.003847	0.004225
2457965.108993	1.007049	0.002922
2457965.109838	1.012655	0.004612
2457965.110706	0.992760	0.003777
2457965.111134	1.008889	0.003305

This table contains photometry of the detrended 262 combined light curves used in Blank et al. 2018 and this work. This data set is processed as described in Blank et al. 2018. The time stamps are the barycentric julian date in the barycentric dynamical time of observation (BJD$_{\text{TDB}}$). The data in its entirety is in the electronic version of *The Astrophysical Journal*. A portion is shown here for guidance regarding its form and content.

C   NEMESIS Validation Reports

Within the validation reports, we display the light curve in various formats to provide a visual aid to identify the transits detected by TLS. As shown in the upper right panel of Figure A4, we display the light curve in black points with the best-fit TLS model in red. We also mark the transits times with cyan colored arrows and the momentum dump times by vertical blue lines. We display the CDPP noise metrics for the light curve before and after processing for the SAP light curve and the detrended light curve. In the middle right panel, we display the TLS power spectrum where the strongest peak is marked by a solid red vertical line, aliases are marked by dashed red vertical lines and the momentum dump rate for the observed TESS sector is marked by dashed grey vertical line. In the middle panels, we display the light curves folded in phase and zoomed in on the transit times using 1/2x, 1x and 2x the TLS detected period. This folding test is to help identify if transits folded on 1/2x or 2x the TLS period appear visually more convincing and to aid in the detection of eclipsing binaries where the primary or secondary transits may display different depths. For each validation report, we display the FFI with our selected aperture and background masks colored in red and purple as shown in the bottom left panel of Figure A4. In each FFI cutout, we also display other nearby stars by referencing Gaia DR2 (Gaia Collaboration et al. 2017, Gaia Collaboration et al. 2018) and marking their pixel positions with cyan circles and their Gaia magnitudes in red text. For comparison, we also utilize archival images from the Digitized Sky Survey (DSS) where the image cutouts cover the same region of sky as the TESS FFIs and are centered on the target star. The pixel scale of the DSS is approximately $1.7''$ per pixel and makes visual confirmation of nearby stars easier to determine. Using the best-fit transit parameters initially output by TLS, we display an example of our vetting reports in Figure A4 for the planet TOI-270 c (TIC 259377017), observed in Sector 4.
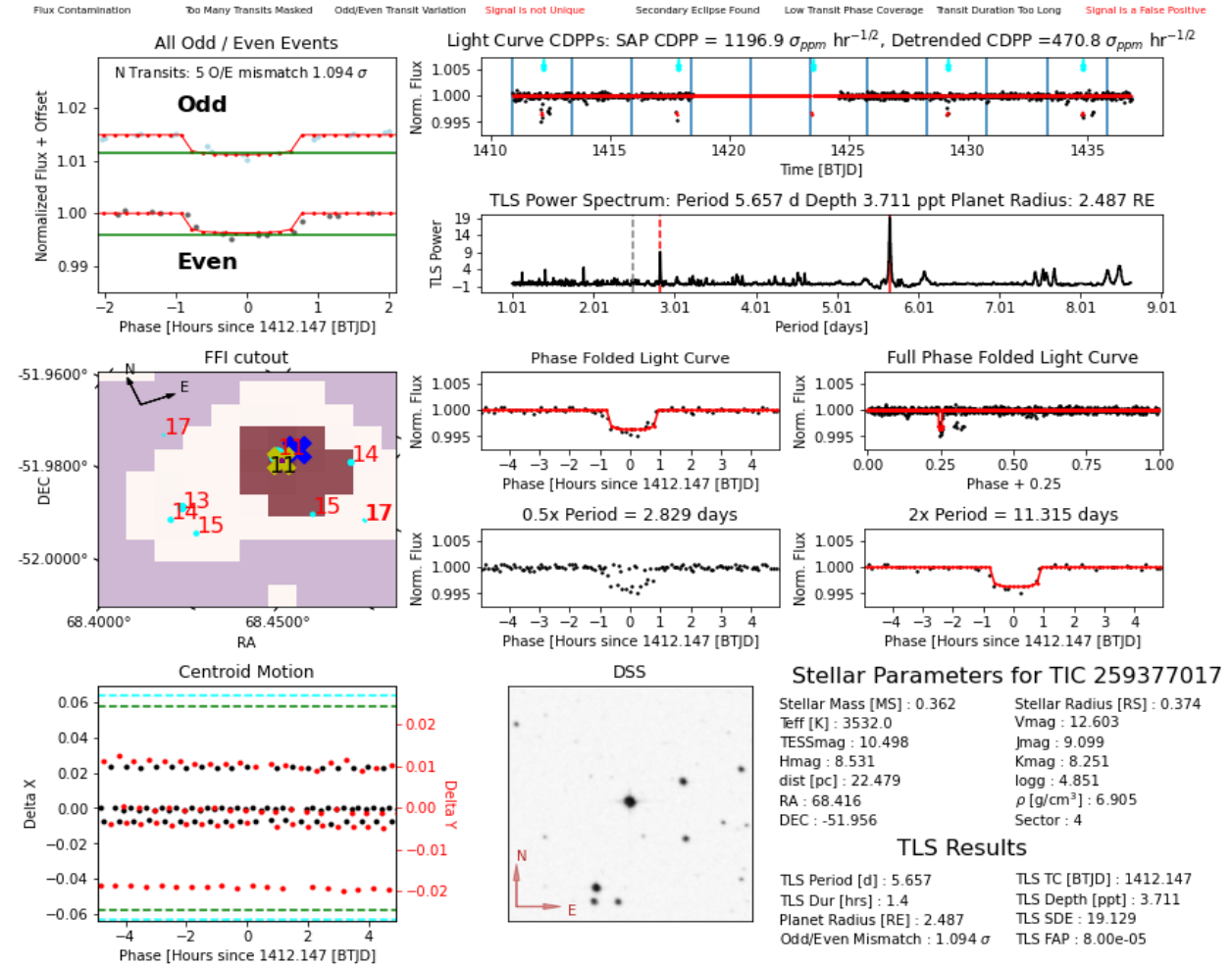
Figure A4: Example of NEMESIS TLS Validation Report for the transiting planet TOI 270 c (TIC 259377017). **Top Left:** *Odd/Even Mismatch test,* we take the odd and even numbered transits and compare how much each transit depth compare while visually verifying that transit duration and shape are consistent. We also display the best-fit TLS transit model in red. **Middle Left:** *FFI image cutout,* an 11×11 pixel cutout of the FFI. We display the target star as a blue X with the center of the centroid of as a yellow X and the selected aperture mask in red with the background shown in purple. Nearby stars are labeled with their GAIA magnitude with cyan colored circles and red text. To visually check whether the centroids are on target, we also place small purple dots marking the centroid positions at each cadence. **Lower Left:** *Centroid Motion,* to help keep track of centroid positions we also plot the motion in the image column (black points) and image row (red points) pixel positions in time and then phase fold the timestamps relative to the TLS detected transit time and period. **Upper Right:** *Light Curve,* we display the full light curve in black points with the best-fit TLS model in red. The transits times are marked by cyan arrows and the momentum dumps are marked with vertical blue lines. We also display the CDPP noise metrics for the light curve before processing for the SAP light curve and afterwards for the detrended light curve. **Middle Right:** *TLS Power Specrum,* we display the TLS power spectra in terms of Signal Detection Efficiency (SDE) as a function of orbital period in days. We mark the momentum dump rate with a vertical grey dashed line, the TLS period corresponding to the strongest SDE peak is marked with a solid red line and 0.5x and 2x harmonics of the TLS period are marked with dashed red lines. **Middle:** *Phase Folded Light Curves,* we fold our light curve centered on the transit time, for the full orbital phase and at 0.5x, 1x and 2x the TLS period. **Lower Middle Right:** *DSS Cutout,* to help visualize our target star we also query the Digitized Sky Survey (DSS) catalog which has a smaller pixel scale than TESS for quick reference. **Lower Right Text:** We display various stellar parameters queried from the TIC and best-fit planet parameters output by TLS. **Top Center Text:** *EDI Vetter Unplugged,* using a modified version of the EDI Vetter tool[19] which uses outputs from TLS, we conduct several automated planet candidate vetting tests with false positive results marked in red colored text which suggest the candidate requires a closer inspection

135

D Planet candidates detected and missed from the TOI catalog

TIC 29960109 (TOI 393) and TIC 29960110 (TOI 1201): From the observing notes listed on the Exoplanet Follow-up Observing Program for TESS (ExoFOP-TESS) website[25], TOI 393 is listed as "Nearby Eclipsing Binary" (NEB) while TOI 1201 remains an active planet candidate. TOIs 393 and 1201 are located on the same TESS pixel and follow-up observations indicate that the transit signal is likely from TOI 1201.

TIC 98796344 (TOI 455): is a multi-star system where three mid-to-late M-dwarfs lie on a single TESS pixel. The planet discovered by Winters et al. 2019 has a radius of 1.38 $R_\oplus$ and an orbital period of 5.35882 days. As shown in Table A3, our initial TLS detection has an accurate match for the orbital period and the planet radius of 1.3391 $R_\oplus$. Our MCMC analysis also provided a comparable radius of 1.26 $R_\oplus$ which is within the published uncertainty and makes this a successful detection.

TIC 259377017 (TOI 270): TOI 270 is a three planet system discovered by Günther et al. 2019 that consists of TOI 270 b (R_P = 1.247 $R_\oplus$, P = 3.36 days), TOI 270 c (R_P = 2.42 $R_\oplus$, P = 5.66 days) and TOI 270 d (R_P = 2.13 $R_\oplus$, P = 11.38 days). The planets orbit close to a mean-motion resonant chain with TOIs 270 b and c in a period ratio of 5:3 and TOIs 270 c and d have a period ratio 2:1. The TLS power spectra of our initial detection of TIC 259377017 has strong power at both the 3.36 and 5.66 day periods with the 5.66 day signal having more power due to being a larger transit. Due to our transit search strategy of only considering the strongest peak in the TLS power spectra and searching only up to 9 days, we did not automatically detect TOI 270 b and TOI 270 d with our pipeline although other transits are visually present as seen in the upper right panel of Figure A4. As for TOI 270 c, we detected the planet in both sectors 4 and 5. TOI 270 c was also observed in Sector 3 but was missed by our pipeline due to particularly high scatter for that light curve. Our initial TLS measured planet radii closely match the published results but our MCMC

---

radii for both sectors are slightly undersized but are still within the published uncertainty.

TIC 220479565 (TOI 269): is an active planet candidate initially detected by the SPOC pipeline with $R_P = 2.9519\ R_\oplus$ and P = 3.698 days which was observed with a 2 minute cadence. We detected TOI 269 in Sector 5 with a close matching period and radius from our MCMC analysis. TOI 269 was also observed in sectors 3 and 4 but our pipeline missed those transit detections. Our sector 3 and 4 SAP light curves have significant instrumental effects near the beginning and end of the satellite orbits. Our PLD, smoothing and outlier rejection processes was able to reduce from the light curve CDPP from 2940 to 2440 ppm in Sector 3 and 4100 ppm to 800ppm in Sector 4 but there still remained regions of higher than average scatter that may have interfered in the automated detection of the transits.

TIC 200322593 (TOI 540) hosts a small, short period planet ($R_P = 0.9\ R_\oplus$, P = 1.239 days) that orbits a rapidly rotating M-dwarf (P_{rot} = 17.43 days), discovered by Ment et al. 2021. We detected a transit signal with $R_P = 0.767\ R_\oplus$ and P= 2.488 days which is about twice the published period but ultimately did not appear transit-like in our validation report and was voted as a false positive. With the automated nature of our pipeline, our smoothing window (for this star, about 4.86 hours) is possibly under-optimized for fully removing the stellar rotation signal.

Both TIC 231702397 (TOI 122) and TIC 305048087 (TOI 237) were missed by our pipeline but are both published planets, discovered by Waalkes et al. 2021. Our pipeline detected a transit event for TOI 122 with $R_P = 2\ R_\oplus$, P = 8.37 days that was vetted to be a false positive and differs from the published values of $R_P = 2.72\ R_\oplus$, P = 5.078 days. For TOI 237, our pipeline detected a transit event with $R_P = 1.4\ R_\oplus$, P = 8.03 days (which also differs from the published values of R_P = 1.44 $R_\oplus$, P = 5.436 days) and was voted as a planet candidate but due to it having a SDE of 8.4, was excluded from this work.

There are a handful of other known planet and planet candidate hosting stars that were missed by our pipeline. TIC 150428135 (TOIs 700 b, c d), TIC 410153553 (TOI 136 b; LHS 3844 b), TIC 12822545 (K2-54 b), TIC 92226327 (TOI 256 b and c; LHS 1140 b and c), TIC 410153553 (TOI 136), TIC 415969908 (TOI 233), TIC 12421862 (TOI 198), TIC 153065527 (TOI 406), TIC 153077621 (TOI 454), TIC 259962054 (TOI 203) and TIC 77156829 (TOI 696) were all missed by our pipeline due to having published/catalog periods being too short (< 1 day) or too long (> 9 days).

Figure A5: A gallery of our 29 planet candidate phase folded light curves (black points). The red lines are the median transit models from our MCMC analysis. The The median of the posteriors for the transit model parameters for each candidate can be found in Table A3. Planet Candidates outlined by green borders are TOIs.

139

Table A3: Best-Fit and Median Posterior Solutions for Planet Candidate Transit Models from TLS and MCMC

TIC ID	TESS Sector	TLS Period	TLS Planet Radius	TLS Transit Time	MCMC Period	MCMC Planet Radius	MCMC Transit Time	MCMC Impact Parameter
139456051	1	2.8424 ± 0.0019	3.2028 ± 0.3378	1325.3616	$2.8424^{+0.0056}_{-0.0056}$	$4.1286^{+0.5690}_{-0.4470}$	$1325.3617^{+0.0296}_{-0.0291}$	$0.8256^{+0.1036}_{-0.0605}$
143996634	1	4.9268 ± 0.0110	3.7148 ± 0.6298	1327.406	$4.927^{+0.0536}_{-0.0536}$	$4.0301^{+0.1455}_{-0.1411}$	$1327.4058^{+0.0433}_{-0.0426}$	$0.7067^{+0.0270}_{-0.0298}$
234299676	1	6.8442 ± 0.0159	2.9942 ± 0.7537	1329.841	$6.8449^{+0.1084}_{-0.1073}$	$3.4455^{+0.1775}_{-0.1686}$	$1329.8405^{+0.0584}_{-0.0583}$	$0.7169^{+0.0380}_{-0.0469}$
281461138	1	5.2113 ± 0.0131	3.8348 ± 0.6506	1325.5449	$5.2109^{+0.0688}_{-0.0677}$	$3.8846^{+0.1309}_{-0.1340}$	$1325.5453^{+0.0450}_{-0.0445}$	$0.7433^{+0.0225}_{-0.0263}$
290048573	1	1.4829 ± 0.0030	2.1006 ± 0.1330	1326.6596	$1.4829^{+0.0044}_{-0.0045}$	$2.8102^{+0.1931}_{-0.1799}$	$1326.6598^{+0.0334}_{-0.0333}$	$0.7044^{+0.0535}_{-0.0708}$
389662862	1	2.9981 ± 0.0044	3.2191 ± 0.3366	1325.9514	$2.998^{+0.0132}_{-0.0131}$	$3.342^{+0.1122}_{-0.1143}$	$1325.9516^{+0.0352}_{-0.0352}$	$0.6259^{+0.0328}_{-0.0411}$
9632592	2	4.9924 ± 0.0087	3.8078 ± 0.6487	1355.3707	$4.9921^{+0.0431}_{-0.0426}$	$4.2722^{+0.1250}_{-0.1262}$	$1355.3707^{+0.0602}_{-0.0601}$	$0.5511^{+0.0433}_{-0.0592}$
50270480	2	1.6514 ± 0.0034	1.7106 ± 0.1129	1354.5419	$1.6514^{+0.0056}_{-0.0057}$	$1.8744^{+0.2509}_{-0.2570}$	$1354.5419^{+0.0456}_{-0.0455}$	$0.6734^{+0.1126}_{-0.1947}$
80315892	2	6.1589 ± 0.0114	2.3433 ± 0.4739	1356.3507	$6.1593^{+0.0702}_{-0.0693}$	$2.3539^{+0.1900}_{-0.1868}$	$1356.3505^{+0.0520}_{-0.0523}$	$0.6948^{+0.0672}_{-0.0914}$
101991992	2	2.7375 ± 0.0032	1.6507 ± 0.1726	1355.861	$2.7375^{+0.0088}_{-0.0088}$	$1.7981^{+0.1319}_{-0.1439}$	$1355.8611^{+0.0358}_{-0.0363}$	$0.6287^{+0.0872}_{-0.1354}$
183231138	2	3.5578 ± 0.0036	2.558 ± 0.3320	1355.1669	$3.5578^{+0.0128}_{-0.0129}$	$2.582^{+0.1198}_{-0.1226}$	$1355.1668^{+0.0362}_{-0.0439}$	$0.6665^{+0.0520}_{-0.0645}$
184111843	2	3.0855 ± 0.0096	2.8029 ± 0.3234	1354.2508	$3.0854^{+0.0293}_{-0.0291}$	$2.8583^{+0.1121}_{-0.1117}$	$1354.2509^{+0.0444}_{-0.0439}$	$0.3814^{+0.0917}_{-0.1502}$
220570288	2	4.4427 ± 0.0057	1.8601 ± 0.3149	1356.232	$4.4427^{+0.0252}_{-0.0247}$	$2.3565^{+0.5918}_{-0.3356}$	$1356.233^{+0.0656}_{-0.0670}$	$0.8089^{+0.0502}_{-0.1072}$
281851658	2	6.1993 ± 0.0153	2.2804 ± 0.5746	1359.8757	$6.2007^{+0.0951}_{-0.0944}$	$2.2441^{+0.2911}_{-0.2588}$	$1359.8751^{+0.0689}_{-0.0685}$	$0.632^{+0.1245}_{-0.1798}$
408038524	3	1.2465 ± 0.0017	2.4323 ± 0.1706	1386.952	$1.2465^{+0.0022}_{-0.0021}$	$4.565^{+0.6234}_{-0.5071}$	$1386.952^{+0.0236}_{-0.0235}$	$0.8776^{+0.0894}_{-0.0613}$
10934226	4	4.8034 ± 0.0105	2.1807 ± 0.3692	1410.9917	$4.8034^{+0.0508}_{-0.0501}$	$2.1443^{+0.2219}_{-0.2090}$	$1410.9919^{+0.0516}_{-0.0517}$	$0.5252^{+0.1459}_{-0.2569}$
23138732	4	4.5577 ± 0.0057	3.3202 ± 0.5654	1410.9822	$4.5579^{+0.0260}_{-0.0263}$	$3.3721^{+0.1673}_{-0.1727}$	$1410.982^{+0.0380}_{-0.0376}$	$0.6925^{+0.0431}_{-0.0557}$
29960109	4	2.4917 ± 0.0077	2.2634 ± 0.2362	1411.6721	$2.4918^{+0.0192}_{-0.0192}$	$2.2487^{+0.1444}_{-0.1479}$	$1411.6719^{+0.0504}_{-0.0498}$	$0.183^{+0.1761}_{-0.1278}$
29960110	4	2.4918 ± 0.0075	2.1157 ± 0.2212	1411.673	$2.4917^{+0.0185}_{-0.0183}$	$2.0664^{+0.1479}_{-0.1790}$	$1411.6728^{+0.0485}_{-0.0479}$	$0.2366^{+0.2070}_{-0.1630}$
98796344	4	5.3591 ± 0.0106	1.3391 ± 0.2709	1412.7064	$5.3596^{+0.0558}_{-0.0565}$	$1.2645^{+0.1300}_{-0.1040}$	$1412.7064^{+0.0491}_{-0.0495}$	$0.3311^{+0.2354}_{-0.2228}$
161478895	4	4.8672 ± 0.0059	3.7196 ± 0.6281	1412.2682	$4.8674^{+0.0286}_{-0.0285}$	$3.5509^{+0.1247}_{-0.1196}$	$1412.268^{+0.0346}_{-0.0346}$	$0.5627^{+0.0485}_{-0.0443}$
206468250	4	5.5669 ± -0.2128	3.3042 ± 0.6695	1411.4297	$5.5641^{+0.0782}_{-0.0772}$	$3.2233^{+0.1481}_{-0.1408}$	$1411.4356^{+0.0445}_{-0.0439}$	$0.6588^{+0.0476}_{-0.0553}$
209457622	4	5.0354 ± 0.0079	1.6253 ± 0.3287	1414.9743	$5.0353^{+0.0400}_{-0.0395}$	$1.5319^{+0.2482}_{-0.2419}$	$1414.9748^{+0.0734}_{-0.0739}$	$0.2612^{+0.2482}_{-0.1798}$
259377017	4	5.6574 ± 0.0139	2.4869 ± 0.5032	1412.1471	$5.6579^{+0.0780}_{-0.0774}$	$2.3529^{+0.1838}_{-0.1629}$	$1412.1475^{+0.0590}_{-0.0587}$	$0.3344^{+0.1915}_{-0.2145}$
406478079	4	1.57 ± 0.0014	2.5025 ± 0.1749	1412.295	$1.57^{+0.0021}_{-0.0022}$	$5.3054^{+0.2629}_{-0.7614}$	$1412.2949^{+0.0221}_{-0.0221}$	$1.0075^{+0.0343}_{-0.0530}$
7688647	5	1.9359 ± 0.0035	2.4759 ± 0.2062	1439.1884	$1.9359^{+0.0066}_{-0.0067}$	$2.7132^{+0.0818}_{-0.0835}$	$1439.1887^{+0.0332}_{-0.0339}$	$0.541^{+0.0381}_{-0.0463}$
44669739	5	2.4111 ± 0.0048	2.7747 ± 0.2673	1438.0304	$2.411^{+0.0116}_{-0.0112}$	$2.9053^{+0.1039}_{-0.1014}$	$1438.0305^{+0.0373}_{-0.0372}$	$0.6064^{+0.0417}_{-0.0469}$
192833836	5	6.2378 ± 0.0193	3.487 ± 0.8803	1442.9738	$6.2368^{+0.1219}_{-0.1190}$	$3.6226^{+0.1534}_{-0.1609}$	$1442.974^{+0.0669}_{-0.0677}$	$0.6221^{+0.0505}_{-0.0663}$
220479565	5	3.6944 ± 0.0106	2.0914 ± 0.3052	1441.0207	$3.6946^{+0.0391}_{-0.0387}$	$2.8577^{+0.2376}_{-0.2144}$	$1441.0206^{+0.0549}_{-0.0546}$	$0.7316^{+0.0562}_{-0.0697}$
259377017	5	5.6605 ± 0.0157	2.5068 ± 0.5077	1440.4501	$5.6604^{+0.0893}_{-0.0880}$	$2.2633^{+0.1538}_{-0.1336}$	$1440.4503^{+0.0705}_{-0.0708}$	$0.2968^{+0.1794}_{-0.1941}$

Table A4: Atmospheric Characterization Rankings For Follow-Up Observations

TIC ID	TESS Sector	RA [deg]	Dec [deg]	TESS magnitude	J magnitude	K magnitude	RP [$R_\oplus$]	MP [$M_\oplus$]	SNR	Doppler Semi-Amplitude [m/s]	TSM	ESM
139456051	1	336.783859	-47.229283	15.34970	13.600	12.714	4.128602	15.986691	11.874213	24.230491	116.030822	74.903532
143996634	1	335.753765	-53.327428	14.43140	12.745	11.965	4.030119	15.347696	8.495298	13.790703	70.734930	41.019245
234299676	1	358.611649	-61.818088	13.65490	12.148	11.294	3.445461	11.758089	8.235459	7.627944	50.721908	23.240705
281461138	1	5.988896	-55.528776	13.01530	11.112	10.245	3.884640	14.417693	11.298390	12.750291	147.036441	83.062000
290048573	1	319.188844	-25.786300	12.67990	11.265	10.514	2.810214	8.301153	17.013639	10.010448	125.998483	46.421523
389662862	1	323.275188	-42.574423	15.24620	13.452	12.529	3.341961	11.163913	8.154024	16.573354	100.699639	52.192536
9632592	2	357.198331	-7.863519	15.01790	13.382	12.562	4.272193	16.950659	9.739416	17.412758	75.026066	46.449747
50270480	2	29.168067	-71.953540	12.46420	11.296	10.550	1.874404	4.167672	9.421817	3.608885	40.362280	10.097319
80315892	2	8.196481	-44.715797	13.38990	11.862	11.020	2.353903	6.152647	8.246789	4.467794	42.069438	15.043026
101991992	2	15.369636	-46.542464	14.01590	12.340	11.565	1.798130	3.891827	8.286213	5.196333	59.920862	18.107811
183231138	2	357.055156	-38.684239	15.28160	13.568	12.769	2.581981	7.200179	7.023134	9.866667	63.008718	25.058121
184111843	2	359.132827	-36.364779	13.82280	12.304	11.477	2.858288	8.559577	9.896756	8.988186	75.106971	30.192509
220570288	2	46.572050	-64.829543	12.45500	11.131	10.291	2.356532	6.160028	10.528961	3.820460	38.934106	12.855060
281851658	2	14.821597	-59.204671	12.69350	11.180	10.328	2.244115	5.672862	9.847903	3.685254	42.977857	14.839293
408038524	3	16.778423	-6.879304	15.05720	13.334	12.480	4.565040	18.945825	23.763564	43.716183	270.929945	185.734208
10934226	4	42.793311	-1.337914	12.87200	11.458	10.657	2.144324	5.250814	7.541693	3.779542	41.305156	13.173706
23138732	4	46.255879	-11.093959	14.06900	12.519	11.702	3.372111	11.335044	10.461356	10.325772	71.365712	32.434492
29960109	4	42.249290	-14.537842	11.20030	9.733	8.875	2.248694	5.693698	11.058413	4.619607	95.623689	32.799796
29960110	4	42.246970	-14.537484	10.94730	9.528	8.646	2.066381	4.931000	9.909295	3.792616	84.208728	27.087291
98796344	4	45.464137	-16.593340	8.84294	7.294	6.496	1.264512	2.139913	9.992555	1.973426	36.164831	54.524599
161478895	4	73.302476	-44.393777	15.61980	13.853	13.009	3.550880	12.378486	7.091324	15.862767	84.175164	41.503154
206468250	4	57.037751	-50.795835	14.67190	13.130	12.341	3.223327	10.499727	7.767496	10.257237	63.799177	27.414030
209457622	4	46.612506	-33.942109	12.37050	11.073	10.235	1.531888	2.964851	3.977976	1.778832	22.528110	5.474758
259377017	4	68.415501	-51.956232	10.49810	9.099	8.251	2.352926	6.149659	23.604753	4.343076	142.742900	49.139620
406478079	4	53.433858	-22.214483	14.95450	13.172	12.359	5.305437	24.450171	35.294599	43.955433	224.217887	166.763819
7688647	5	65.362813	-39.013727	15.57150	13.735	12.922	2.713195	7.832774	9.791784	15.018084	97.561991	42.452327
44669739	5	59.891484	-28.249734	14.91290	13.502	12.702	2.905316	8.797528	8.766469	12.044053	72.519333	28.164262
192833836	5	83.103441	-39.833811	13.69400	12.001	11.096	3.622602	12.805514	15.762378	10.096336	79.303364	41.048627
220479565	5	75.846088	-54.177201	12.29580	10.909	10.100	2.857674	8.551350	20.506703	6.641619	84.642565	32.150844
259377017	5	68.415501	-51.956232	10.49810	9.099	8.251	2.263309	5.756908	27.452164	4.065023	135.695670	45.460875

BIBLIOGRAPHY

Agol, E., Luger, R., & Foreman-Mackey, D. 2020, The Astronomical Journal, 159, 123

Aigrain, S., Parviainen, H., & Pope, B. J. S. 2016, Monthly Notices of the Royal Astronomical Society, 459, 2408

Anglada-Escudé, G., Amado, P. J., Barnes, J., et al. 2016, Nature, 536, 437

Angus, R., Morton, T., Aigrain, S., Foreman-Mackey, D., & Rajpaul, V. 2018, Monthly Notices of the Royal Astronomical Society, 474, 2094

Angus, R., Morton, T. D., Foreman-Mackey, D., et al. 2019, The Astronomical Journal, 158, 173

Ballard, S. 2019, The Astronomical Journal, 157, 113

Barclay, T., Pepper, J., & Quintana, E. V. 2018, The Astrophysical Journals, 239, 2

Barnes, R., Deitrick, R., Luger, R., et al. 2016, ArXiv e-prints, arXiv:1608.06919

Beyer, H. 1981, Biometrical Journal, 23, 413

Bixel, A., & Apai, D. 2017, The Astrophysical Journal, Letters, 836, L31

Blank, D. L., Jayawardene, B., Shankland, P., et al. 2007, in GEMSS Search For Transiting Exoplanets Around Proxima Centauri, ESO Workshop, Santiago, Chile

Blank, D. L., Feliz, D., Collins, K. A., et al. 2018, The Astronomical Journal, 155, 228

Bochanski, J. J., Hawley, S. L., Covey, K. R., et al. 2010, The Astronomical Journal, 139, 2679

Bonfils, X., Forveille, T., Delfosse, X., et al. 2005, Astronomy & Astrophysics, 443, L15

Bonfils, X., Delfosse, X., Udry, S., et al. 2013, Astronomy & Astrophysics, 549, A109

Borucki, W. J., & Summers, A. L. 1984, Icarus, 58, 121

Borucki, W. J., Koch, D., Basri, G., et al. 2010, Science, 327, 977

Bouma, L. G., Hartman, J. D., Bhatti, W., Winn, J. N., & Bakos, G. Á. 2019, The Astrophysical Journals, 245, 13

Boutle, I. A., Mayne, N. J., Drummond, B., et al. 2017, Astronomy & Astrophysics, 601, A120

Brasseur, C. E., Phillip, C., Fleming, S. W., Mullally, S. E., & White, R. L. 2019, Astrocut: Tools for creating cutouts of TESS images, ascl:1905.007

Brugger, B., Mousis, O., Deleuil, M., & Lunine, J. I. 2016, The Astrophysical Journal, Letters, 831, L16

Burger, D., Stassun, K. G., Pepper, J. A., et al. 2013, in Astronomical Society of the Pacific Conference Series, Vol. 475, Astronomical Data Analysis Software and Systems XXII, ed. D. N. Friedel, 399

Chang, S. W., Byun, Y. I., & Hartman, J. D. 2015, The Astrophysical Journal, 814, 35

Chauvenet, W. 1960, A Manual of spherical and practical astronomy - Vol.1: Spherical astronomy; Vol.2: Theory and use of astronomical instruments. Method of least squares (New York: Dover Publication)

Chen, J., & Kipping, D. 2016, The Astrophysical Journal, 834, 17

Chen, J., & Kipping, D. 2017, The Astrophysical Journal, 834, 17

Christiansen, J. L., Clarke, B. D., Burke, C. J., et al. 2015, The Astrophysical Journal, 810, 95

143

Claret, A. 2017, Astronomy & Astrophysics, 600, A30

Claret, A., & Bloemen, S. 2011, Astronomy & Astrophysics, 529, A75

Cloutier, R., & Menou, K. 2020, The Astronomical Journal, 159, 211

Collins, K. A., Kielkopf, J. F., Stassun, K. G., & Hessman, F. V. 2017, The Astronomical Journal, 153, 77

Collins, K. A., Collins, K. I., Pepper, J., et al. 2018, ArXiv e-prints, arXiv:1803.01869

Collins, J. M., Jones, H. R. A., & Barnes, J. R. 2017, Astronomy & Astrophysics, 602, A48

Coughlin, J. L., Mullally, F., Thompson, S. E., et al. 2016, The Astrophysical Journals, 224, 12

Crossfield, I. J. M., Waalkes, W., Newton, E. R., et al. 2019, The Astrophysical Journal, 883, L16

Damasso, M., & Del Sordo, F. 2017, Astronomy & Astrophysics, 599, A126

Davenport, J. R. A., Kipping, D. M., Sasselov, D., Matthews, J. M., & Cameron, C. 2016, The Astrophysical Journal, Letters, 829, L31

Deming, D., Knutson, H., Kammer, J., et al. 2015, The Astrophysical Journal, 805, 132

Demory, B.-O., Ségransan, D., Forveille, T., et al. 2009, Astronomy & Astrophysics, 505, 205

Dressing, C. D., & Charbonneau, D. 2013, The Astrophysical Journal, 767, 95

—. 2015, The Astrophysical Journal, 807, 45

Eastman, J., Gaudi, B. S., & Agol, E. 2013, Publications of the Astronomical Society of the Pacific, 125, 83

Eastman, J., Siverd, R., & Gaudi, B. S. 2010, Publications of the Astronomical Society of the Pacific, 122, 935

Eastman, J. D., Rodriguez, J. E., Agol, E., et al. 2019, arXiv e-prints, arXiv:1907.09480

144

Espinoza, N., Kossakowski, D., & Brahm, R. 2019, Monthly Notices of the Royal Astronomical Society, 490, 2262

Fadavi, M., Verveer, A., Aymon, J., et al. 2006, Astronomische Nachrichten, 327, 811

Feinstein, A. D., Montet, B. T., Foreman-Mackey, D., et al. 2019, Publications of the Astronomical Society of the Pacific, 131, 094502

Feliz, D. L., Plavchan, P., Bianco, S. N., et al. 2021, The Astronomical Journal, 161, 247

Feliz, D. L., Blank, D. L., Collins, K. A., et al. 2019, The Astronomical Journal, 157, 226

Fischer, D. A., Anglada-Escude, G., Arriagada, P., et al. 2016, Publications of the Astronomical Society of the Pacific, 128, 066001

Foreman-Mackey, D., Luger, R., Czekala, I., et al. 2020, exoplanet-dev/exoplanet v0.3.2, doi:10.5281/zenodo.1998447

France, K., Froning, C. S., Linsky, J. L., et al. 2013, The Astrophysical Journal, 763, 149

Fulton, B. J., & Petigura, E. A. 2018, The Astronomical Journal, 156, 264

Fulton, B. J., Petigura, E. A., Howard, A. W., et al. 2017, The Astronomical Journal, 154, 109

Gaia Collaboration, Brown, A. G. A., Vallenari, A., et al. 2016, ArXiv e-prints, arXiv:1609.04172

Gaia Collaboration, Clementini, G., Eyer, L., et al. 2017, Astronomy & Astrophysics, 605, A79

Gaia Collaboration, Brown, A. G. A., Vallenari, A., et al. 2018, Astronomy & Astrophysics, 616, A1

Gaidos, E., Mann, A. W., Kraus, A. L., & Ireland, M. 2016, Monthly Notices of the Royal Astronomical Society, 457, 2877

Gilbert, E. A., Barclay, T., Quintana, E. V., et al. 2021, arXiv e-prints, arXiv:2109.03924

Ginsburg, A., Sipőcz, B. M., Brasseur, C. E., et al. 2019, The Astronomical Journal, 157, 98

Goulding, N. T., Barnes, J. R., Pinfield, D. J., et al. 2012, Monthly Notices of the Royal Astronomical Society, 427, 3358

Gray, D. F. 2009, The Astrophysical Journal, 697, 1032

Guerrero, N. M., Seager, S., Huang, C. X., et al. 2021, The Astrophysical Journal, Supplement, 254, 39

Günther, M. N., Pozuelos, F. J., Dittmann, J. A., et al. 2019, Nature Astronomy, 3, 1099

Hardegree-Ullman, K. K., Zink, J. K., Christiansen, J. L., et al. 2020, The Astrophysical Journals, 247, 28

Hartman, J. D., & Bakos, G. Á. 2016, Astronomy and Computing, 17, 1

Hawley, S. L., Davenport, J. R. A., Kowalski, A. F., et al. 2014, The Astrophysical Journal, 797, 121

Hedges, C., Saunders, N., Barentsen, G., et al. 2019, The Astrophysical Journal, 880, L5

Hippke, M., David, T. J., Mulders, G. D., & Heller, R. 2019, The Astronomical Journal, 158, 143

Hippke, M., & Heller, R. 2019, Astronomy & Astrophysics, 623, A39

Hoffman, M. D., & Gelman, A. 2014, Journal of Machine Learning Research, 15, 1593

Howard, W. S., Tilley, M. A., Corbett, H., et al. 2018, The Astrophysical Journal, 860, L30

Hsu, D. C., Ford, E. B., & Terrien, R. 2020, Monthly Notices of the Royal Astronomical Society, 498, 2249

Huang, C. X., Shporer, A., Dragomir, D., et al. 2018, arXiv e-prints, arXiv:1807.11129

Huang, C. X., Vanderburg, A., Pál, A., et al. 2020, Research Notes of the American Astronomical Society, 4, 204

Huber, P. 1981, Robust Statistics (Wiley)

Hunter, J. D. 2007, Computing in Science & Engineering, 9, 90

Ida, S., & Lin, D. N. C. 2004, The Astrophysical Journal, 616, 567

Jenkins, J. M., Twicken, J. D., McCauliff, S., et al. 2016, in Society of Photo-Optical Instrumen-
    tation Engineers (SPIE) Conference Series, Vol. 9913, Software and Cyberinfrastructure for
    Astronomy IV, ed. G. Chiozzi & J. C. Guzman, 99133E

Jensen, E. 2013, Tapir: A web interface for transit/eclipse observability, Astrophysics Source Code
    Library, ascl:1306.007

Joshi, M. M., Haberle, R. M., & Reynolds, R. T. 1997, Icarus, 129, 450

Kane, S. R., Gelino, D. M., & Turnbull, M. C. 2017, The Astronomical Journal, 153, 52

Kempton, E. M. R., Bean, J. L., Louie, D. R., et al. 2018, Publications of the Astronomical Society
    of the Pacific, 130, 114401

Kervella, P., Thévenin, F., & Lovis, C. 2017, Astronomy & Astrophysics, 598, L7

Kipping, D. M. 2013, Monthly Notices of the Royal Astronomical Society, 435, 2152

Kipping, D. M., Cameron, C., Hartman, J. D., et al. 2017, The Astronomical Journal, 153, 93

Konacki, M., Torres, G., Jha, S., & Sasselov, D. D. 2003, Nature, 421, 507

Kopparapu, R. K., Ramirez, R., Kasting, J. F., et al. 2013, The Astrophysical Journal, 765, 131

Kostov, V. B., Mullally, S. E., Quintana, E. V., et al. 2019, The Astronomical Journal, 157, 124

Kostov, V. B., Schlieder, J. E., Barclay, T., et al. 2019, The Astronomical Journal, 158, 32

Kovács, G., Zucker, S., & Mazeh, T. 2002, Astronomy & Astrophysics, 391, 369

—. 2016, BLS: Box-fitting Least Squares, ascl:1607.008

Kowalski, A. F., Mathioudakis, M., Hawley, S. L., et al. 2016, The Astrophysical Journal, 820, 95

Kreidberg, L. 2015, Publications of the Astronomical Society of the Pacific, 127, 1161

Kunimoto, M., Winn, J. N., Ricker, G. R., & Vanderspek, R. 2022, arXiv e-prints, arXiv:2202.03656

Laughlin, G., Bodenheimer, P., & Adams, F. C. 2004, The Astrophysical Journal, Letters, 612, L73

Li, Y., Stefansson, G., Robertson, P., et al. 2017, ArXiv e-prints, arXiv:1712.04483

Liu, H.-G., Jiang, P., Huang, X., et al. 2017, ArXiv e-prints, arXiv:1711.07018

Livingston, J. H., Endl, M., Dai, F., et al. 2018, The Astronomical Journal, 156, 78

Lopez, E., & Rice, K. 2018, Monthly Notices of the Royal Astronomical Society, 479, 5303

Lopez, E. D., & Fortney, J. J. 2014, The Astrophysical Journal, 792, 1

Lopez, E. D., Fortney, J. J., & Miller, N. 2012, The Astrophysical Journal, 761, 59

Loyd, R. O. P., France, K., Youngblood, A., et al. 2018, The Astrophysical Journal, 867, 71

Luger, R., Agol, E., Foreman-Mackey, D., et al. 2019, The Astronomical Journal, 157, 64

Luger, R., Agol, E., Kruse, E., et al. 2016, The Astronomical Journal, 152, 100

Luger, R., Barnes, R., Lopez, E., et al. 2015, Astrobiology, 15, 57

Luger, R., Kruse, E., Foreman-Mackey, D., Agol, E., & Saunders, N. 2018, The Astronomical Journal, 156, 99

Mandel, K., & Agol, E. 2002a, The Astrophysical Journal, Letters, 580, L171

—. 2002b, The Astrophysical Journall, 580, L171

Manduca, A., Bell, R. A., & Gustafsson, B. 1977, Astronomy & Astrophysics, 61, 809

Marcy, G. W., Butler, R. P., Vogt, S. S., Fischer, D., & Lissauer, J. J. 1998, The Astrophysical Journal, Letters, 505, L147

Martinez, C. F., Cunha, K., Ghezzi, L., & Smith, V. V. 2019, The Astrophysical Journal, 875, 29

Mathur, S., Huber, D., Batalha, N. M., et al. 2017, The Astrophysical Journal, Supplement, 229, 30

Mayo, A. W., Vanderburg, A., Latham, D. W., et al. 2018, The Astronomical Journal, 155, 136

Mayor, M., & Queloz, D. 1995, Nature, 378, 355

McQuillan, A., Aigrain, S., & Mazeh, T. 2013, Monthly Notices of the Royal Astronomical Society, 432, 1203

McQuillan, A., Mazeh, T., & Aigrain, S. 2014, The Astrophysical Journal, Supplement, 211, 24

Meadows, V. S., Arney, G. N., Schwieterman, E. W., et al. 2016, ArXiv e-prints, arXiv:1608.08620

Ment, K., Irwin, J., Charbonneau, D., et al. 2021, The Astronomical Journal, 161, 23

Meunier, N., Desort, M., & Lagrange, A. M. 2010, Astronomy & Astrophysics, 512, A39

Montalto, M., Borsato, L., Granata, V., et al. 2020, Monthly Notices of the Royal Astronomical Society, 498, 1726

Montgomery, R., & Laughlin, G. 2009, Icarus, 202, 1

Morton, T. D., & Johnson, J. A. 2011, The Astrophysical Journal, 738, 170

Morton, T. D., & Swift, J. 2014, The Astrophysical Journal, 791, 10

Muirhead, P. S., Dressing, C. D., Mann, A. W., et al. 2018, The Astronomical Journal, 155, 180

Nardiello, D., Borsato, L., Piotto, G., et al. 2019, Monthly Notices of the Royal Astronomical Society, 490, 3806

Newton, E. R., Irwin, J., Charbonneau, D., Berta-Thompson, Z. K., & Dittmann, J. A. 2016a, The Astrophysical Journal, Letters, 821, L19

Newton, E. R., Irwin, J., Charbonneau, D., et al. 2016b, The Astrophysical Journal, 821, 93

Nutzman, P., & Charbonneau, D. 2008, Publications of the Astronomical Society of the Pacific, 120, 317

Ofir, A. 2014, Astronomy & Astrophysics, 561, A138

Oliphant, T. E. 2006, A guide to NumPy, Vol. 1 (Trelgol Publishing USA)

Parviainen, H. 2015, Monthly Notices of the Royal Astronomical Society, 450, 3233

Pepper, J., Kuhn, R. B., Siverd, R., James, D., & Stassun, K. 2012, Publications of the Astronomical Society of the Pacific, 124, 230

Pepper, J., Pogge, R. W., DePoy, D. L., et al. 2007, Publications of the Astronomical Society of the Pacific, 119, 923

Plavchan, P. 2006, PhD thesis, University of California, Los Angeles

Plavchan, P., Barclay, T., Gagné, J., et al. 2020, Nature, 582, 497

Pope, B. J. S., Parviainen, H., & Aigrain, S. 2016, Monthly Notices of the Royal Astronomical Society, 461, 3399

Price-Whelan, A. M., Sipőcz, B. M., Günther, H. M., et al. 2018, The Astronomical Journal, 156, 123

Quintana, E. V., Barclay, T., Raymond, S. N., et al. 2014, Science, 344, 277

Ramirez, R. M., & Kaltenegger, L. 2014, The Astrophysical Journal, Letters, 797, L25

Rauer, H., Catala, C., Aerts, C., et al. 2014, Experimental Astronomy, 38, 249

Reichart, D., Nysewander, M., Moran, J., et al. 2005, Nuovo Cimento C Geophysics Space Physics C, 28, 767

Reiners, A. 2012, Living Reviews in Solar Physics, 9, 1

Ribas, I., Bolmont, E., Selsis, F., et al. 2016, Astronomy & Astrophysics, 596, A111

Ricker, G. R., Winn, J. N., Vanderspek, R., et al. 2014, Journal of Astronomical Telescopes, Instruments, and Systems, 1, 014003

Ricker, G. R., Winn, J. N., Vanderspek, R., et al. 2015, Journal of Astronomical Telescopes, Instruments, and Systems, 1, 014003

Rogers, L. A. 2015, The Astrophysical Journal, 801, 41

Saar, S. H., & Donahue, R. A. 1997, The Astrophysical Journal, 485, 319

Salvatier, J., Wiecki, T. V., & Fonnesbeck, C. 2016, PeerJ Computer Science, 2, e55

Schlaufman, K. C., & Laughlin, G. 2010, Astronomy & Astrophysics, 519, A105

Seager, S., & Mallén-Ornelas, G. 2003, The Astrophysical Journal, 585, 1038

Ségransan, D., Kervella, P., Forveille, T., & Queloz, D. 2003, Astronomy & Astrophysics, 397, L5

Shankland, P. D., Rivera, E. J., Laughlin, G., et al. 2006, The Astrophysical Journal, 653, 700

Shapley, H. 1951, Proceedings of the National Academy of Science, 37, 15

Shields, A. L., Ballard, S., & Johnson, J. A. 2016, Physics Reports, 663, 1

Siverd, R. J., Beatty, T. G., Pepper, J., et al. 2012, The Astrophysical Journal, 761, 123

Stassun, K. G., Oelkers, R. J., Pepper, J., et al. 2018, The Astronomical Journal, 156, 102

Stassun, K. G., Oelkers, R. J., Paegert, M., et al. 2019, The Astronomical Journal, 158, 138

Sullivan, P. W., Winn, J. N., Berta-Thompson, Z. K., et al. 2015, The Astrophysical Journal, 809, 77

Tarter, J. C., Backus, P. R., Mancinelli, R. L., et al. 2007, Astrobiology, 7, 30

The Theano Development Team, Al-Rfou, R., Alain, G., et al. 2016, arXiv e-prints, arXiv:1605.02688

Tofflemire, B. M., Wisniewski, J. P., Kowalski, A. F., et al. 2012, The Astronomical Journal, 143, 12

Turbet, M., Leconte, J., Selsis, F., et al. 2016, Astronomy & Astrophysics, 596, A112

Vakili, M., & Hogg, D. W. 2016, Do fast stellar centroiding methods saturate the Cramr-Rao lower bound?, arXiv:1610.05873

Van Eylen, V., Agentoft, C., Lundkvist, M. S., et al. 2018, Monthly Notices of the Royal Astronomical Society, 479, 4786

van Rossum, G. 1995, Python tutorial, Tech. Rep. CS-R9526, Centrum voor Wiskunde en Informatica (CWI), Amsterdam

Vanderburg, A., Plavchan, P., Johnson, J. A., et al. 2016, Monthly Notices of the Royal Astronomical Society, 459, 3565

Virtanen, P., Gommers, R., Oliphant, T. E., et al. 2020, Nature Methods, 17, 261

Waalkes, W. C., Berta-Thompson, Z. K., Collins, K. A., et al. 2021, The Astronomical Journal, 161, 13

Walker, A. R. 1981, Monthly Notices of the Royal Astronomical Society, 195, 1029

Wargelin, B. J., Saar, S. H., Pojmański, G., Drake, J. J., & Kashyap, V. L. 2017, Monthly Notices of the Royal Astronomical Society, 464, 3281

Weiss, L. M., & Marcy, G. W. 2014, The Astrophysical Journal, Letters, 783, L6

Wells, R., Poppenhaeger, K., & Watson, C. A. 2018, Monthly Notices of the Royal Astronomical
Society, 473, L131

Winn, J. 2011, Exoplanets, edited by S. Seager. Tucson, AZ: University of Arizona Press, 2011,
526 pp. ISBN 978-0-8165-2945-2, 55

Winters, J. G., Medina, A. A., Irwin, J. M., et al. 2019, The Astronomical Journal, 158, 152

Wolszczan, A., & Frail, D. A. 1992, Nature, 355, 145

Wu, Y. 2019, The Astrophysical Journal, 874, 91

Zechmeister, M., Reiners, A., Amado, P. J., et al. 2018, Astronomy & Astrophysics, 609, A12

Zink, J. K., Hardegree-Ullman, K. K., Christiansen, J. L., et al. 2020, The Astronomical Journal,
159, 154